The role of the sympathetic nervous system in multiple myeloma progression

The University of Iowa

Belin-Blank Center

Deborah E. Arul, Michael H. Tomasson MD, and Melissa L. Bates PhD
The Laboratory of Integrative Pathophysiology and Genetics, University of Iowa

Introduction

Multiple myeloma (MM), which is the second most common hematologic malignancy in the United States, is an incurable malignancy of bone marrow plasma cells. MM is always preceded by a common asymptomatic state known as monoclonal gammopathy of undetermined significance (MGUS). Despite the genetic similarity between MGUS and MM, progression only accrues at a rate of 1-2% per year (Kyle, 2002). This low progression rate suggests that non-genetic factors play a significant role in the development of MM. One such non-genetic factor could be chronic intermittent hypoxia (CIH), a key component of sleep apnea. Figure 1 shows that, when compared to normoxia-exposed C57BL/6J mice, which are usually resistant to MM, CIH-exposed C57BL/6J mice were more vulnerable to MM cells, with 67% of the mice developing terminal paralysis (Ali, 2019). This correlation may be explained by the increase in sympathetic tone caused by CIH, but no studies have been conducted on this matter. The first step to conducting such a study, however, would be to prove that the sympathetic nervous system can be inhibited.

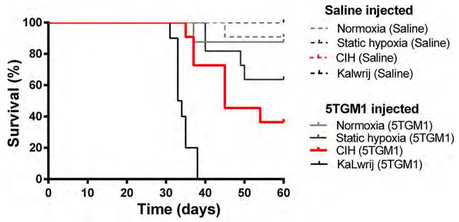

Figure 1: Kaplan-Meier curve indicating that the CIH-exposed group experienced the lowest survival among C57BL/6J mice.

Methodology

To establish a baseline with which to compare sympathetic responses, we measured 4 male and 2 female mice's response to dobutamine, an agent which mimics epinephrine. We then supplemented the mice's regular chow and water with Nutri-Cal and 0.25% saccharine water and measured the mice's average food and water intake. With that information, we dosed 9 animals with 100 mg/kg/day of propranolol by adding 5 mg/mL of propranolol to their saccharine water as well as a 0.001 mg/mL propranolol solution to their Nutri-Cal. We then placed 6 of the dosed mice in the CIH chamber and the other 3 in the normoxia chamber. We also placed 3 undosed animals in the CIH chamber and 3 in the normoxia chamber to serve as a control. After several days, we measured the mice's baseline heart rate and challenged the mice with dobutamine to test whether the dosed mice were beta blocked.

Figure 2: : Environmental exposure chambers used to simulate CIH

Results

Heart Rate

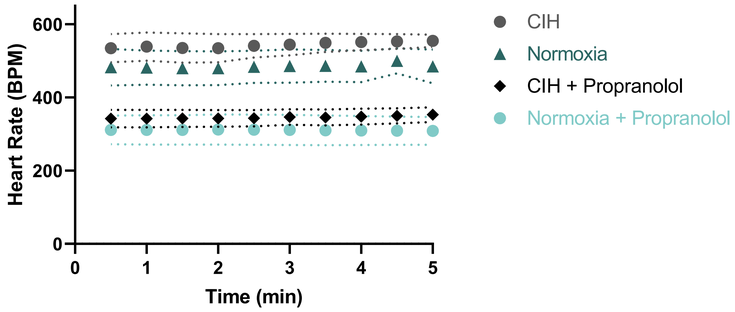

Figure 3: Baseline heart rate data without addition of dobutamine demonstrating mice dosed with propranolol have lower baseline heart rates as compared to those of the mice that were not given propranolol.

Dobutamine Challenge

CIH and Propranolol

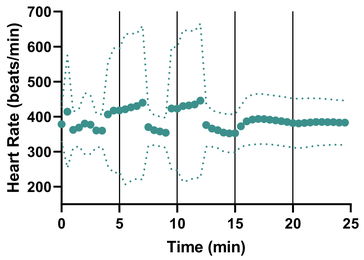

Figure 5: Response of mice exposed to CIH and dosed with propranolol

CIH

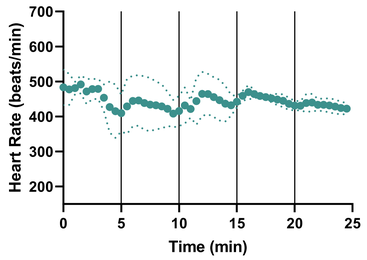

Figure 6: Response of mice exposed to CIH but not dosed with propranolol

Normoxia and Propranolol

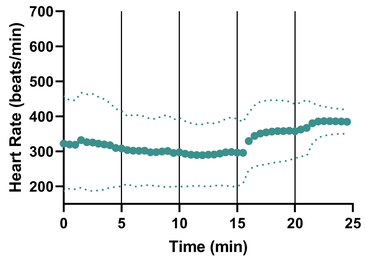

Figure 7: Response of mice in normal oxygen conditions and dosed with propranolol

Normoxia

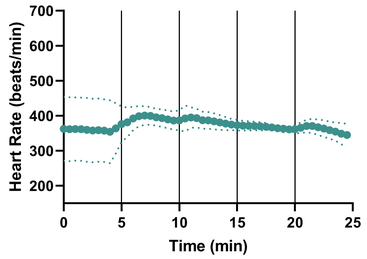

Figure 8: Response of mice in normal oxygen conditions but not dosed with propranolol

Implications

Modern cancer drugs pose staggering financial burdens. State-of-the-art treatment for newly diagnosed myeloma requires regimens that are unaffordable for even well-insured patients. At an average of $100,000 per year for a new cancer drug, many myeloma patients will not receive the medicine (Tomasson, 2018). An understanding of how MGUS progresses to MM would allow for the identification of those at highest risk of MM and the development of more cost-efficient and effective treatment and prevention plans. Our study has taken the first step to achieving this understanding by showing that CIH elevates sympathetic tone and that it is possible to inhibit this increase in sympathetic tone with beta-blockers. Essentially, our study has begun to investigate the role of the sympathetic nervous system in the progression of MGUS to MM. Future studies should focus on the relationship between increased sympathetic tone and malignant cell engraftment as well as the specific effect the sympathetic nervous system has on the bone marrow microenvironment.

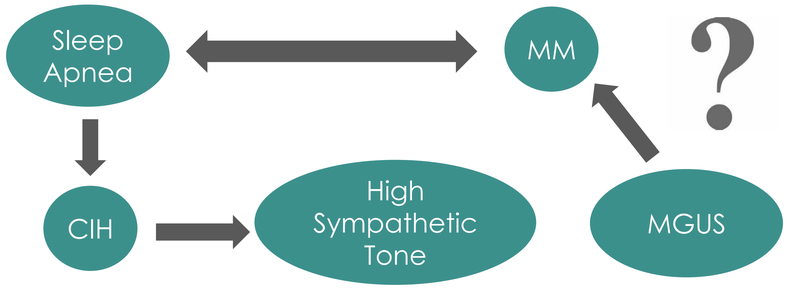

Acknowledgements

I would like to thank the Belin Blank Center and the SSTP program for giving me the opportunity to experience a research setting. I would also like to thank Dr. Bates and Dr. Tomasson for mentoring me and giving me as many opportunities to grow as possible.

References

Ali M., Kowkuntla S., Delloro D. J., Galambos C., Hathi D., Janz S., Shokeen M., Tripathi C., Xu H., Yuk J., Zhan F., Tomasson M. H., and Bates M. L. (2019). Chronic intermittent hypoxia enhances disease progression in myeloma-resistant mice. *American journal of physiology Regulatory, integrative and comparative physiology.*

Kyle, R. A., Therneau T. M., Rajkumar S. V., Offord J. R., Larson D. R., Plevak M. F., & Melton L. (2002). A long term study of prognosis in monoclonal gammopathy of undetermined significance. *New England Journal of Medicine* 346: 564-569.

Ravi, P., Kumar, S. K., Cerhan, J. R., Maurer, M. J., Dingli, D., Ansell, S. M., & Rajkumar, S. V. (2018). Defining cure in multiple myeloma: a comparative study of outcomes of young individuals with myeloma and curable hematologic malignancies. *Blood cancer journal*, 8(3), 26. doi:10.1038/s41408-018-0065-8.

Tomasson M. H., Ali M., De Oliveira V., Xiao Q., Jethava Y., Zhan F., Fitzsimmons A. M., & Bates M. L. (2018). *Prevention is the Best Treatment: The Case for Understanding the Transition from Monoclonal Gammopathy of Undetermined Significance to Myeloma. International Journal of Molecular Science* 19.

Enabling User-Defined Security Policies for Programmable IoT Systems

Samuel Berkun, Dr. Omar Chowdhury, Moosa Yahyazadeh

The University of Iowa

Belin-Blank Center, College of Education

Introduction

- People use Internet of Things (IoT) systems to control their smart devices, in their smart homes
- IoT platforms rely on downloading third-party apps, which may be malicious
- PATRIOT (Policy AssisTed Resiliency for IOT automated systems) ensures safety by filtering action requests in IoT systems

About PATRIOT Framework

- When applications want to control devices, they sent action requests to the IoT platform. For example, an app might send a request that says "Open the bedroom window".
- PATRIOT runs on the IoT platform, where it controls the flow of requests. For each request, PATRIOT either *allows* or *denies* the request. This decision is based on the security policies defined by the user.
- Users can define policies directly in the language, or use the Graphical User Interface (GUI) to automatically generate them.

Language and GUI Design

- Since PATRIOT is meant to be usable by everyone, language and GUI are designed to be as simple and intuitive as possible
- Language is high-level (close to English) and meant to translate from intuitive user expectations
- GUI consists primarily of selection menus, to make it impossible to create invalid syntax
- GUI developed as a web interface using HTML/CSS and Bootstrap framework
  - available for any device with a web browser

PATRIOT Blocking Malicious Applications:

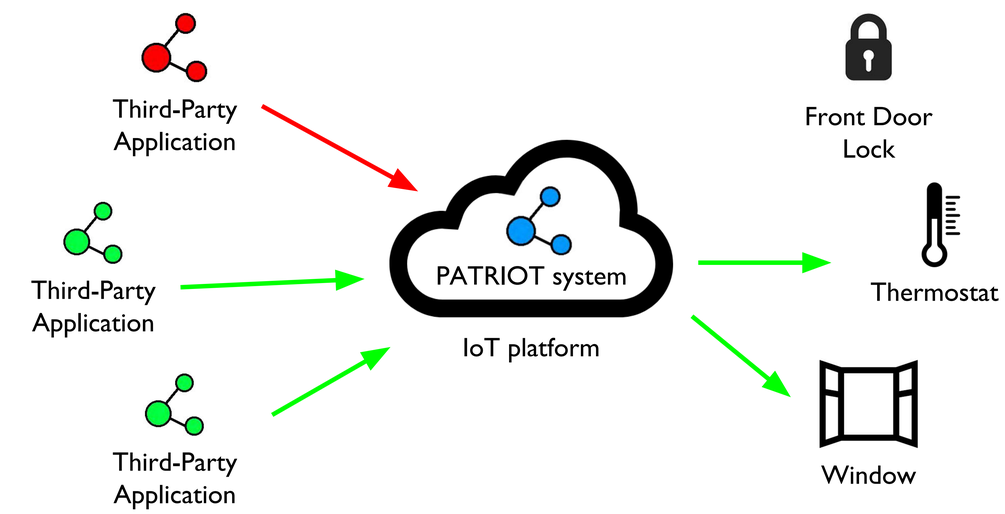

Figure 1: PATRIOT system in action. The malicious application is trying to unlock the front door, but is unable to do so because the user has defined a security policy that restricts access to the front door lock: Figure 2 gives an example of how this policy can be defined.

```
ALLOW
    action_device = front-door-lock
    and action_command = unlock
ONLY IF
    automation_unit = virtual-keys
    and state(my_location) = home
```

Figure 2: A policy, defined in the PATRIOT language.

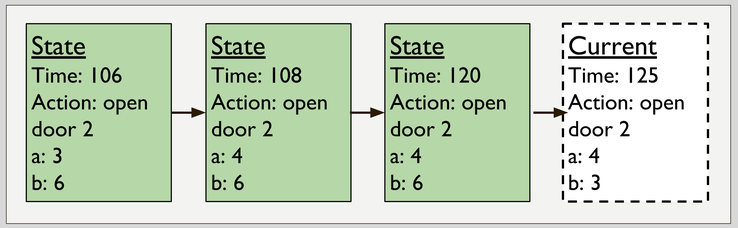

Figure 3: An example execution trace, being evaluated with respect to the current state.

Figure 4: A screenshot of the GUI developed for PATRIOT.

```
Sat:
    x > 5
    x < 7
Unsat:
    x > 2
    x < 4
    x ≠ 3
Unsat:
    ∀x∈X, x > 6
    ∃x∈X, x = 0
```

Figure 5: An example of satisfiable and unsatisfiable sets of formulas.

```
ALLOW
    action_device = water_main
    and action_command = off
EXCEPT
    once(
        state(smoke_detector) = off
    ) within [0, 30]
```

$$(\sigma_i.\text{actionDevice} = \text{“water\_main”} \land \sigma_i.\text{actionCommand} = \text{“off”}) \rightarrow (\exists\, j \in [0,i])(\sigma_j.\text{smokeDetector} = \text{off} \land (\sigma_i.\text{time} - \sigma_j.\text{time}) \in [0,30])$$

Figure 6: An example of a policy being converted into a sub-formula

Traces and Policy Analysis

- Conditions in the PATRIOT language can have temporal formulas - essentially, filtering depends on past events as well as present
- PATRIOT treats the past as a sequence of *states*, which is called a *trace*. A state is stored whenever an action occurs. See Figure 3 for an example.
- Occasionally, it may be possible for the system to reach a point where it gets stuck: The policies are defined such that with the current trace, no actions are allowed.
- The PATRIOT policy analysis warns the user if the user-defined policies may cause the system to get stuck in the future
- Analysis is done by converting policies into SMT formulas, which are processed by the Z3 SMT solver.

SMT Solving

- SMT solvers, such as Z3, check whether a set of first-order logic formulas are satisfiable. See Figure 5 for an example of this.
- Each policy is essentially a formula of the form "action implies condition"

Conclusions and Future Work

- Use of PATRIOT language structured policies allows avoiding many issues with previous implementations
- Analysis can be expanded and improved in efficiency: Alternate definitions of "stuck" trace
- Adoption of system into smart home platforms; improving usability

Acknowledgments

I am grateful to everyone in the Computational Logic Center at the University of Iowa for welcoming me to their lab. I would like to thank Dr. Omar Chowdhury and Moosa Yahyazadeh for bringing me onto the project, as well as taking the time to explain everything to me and making sure I was comfortable with my work. Finally, I would like to thank the Belin-Blank Center for providing me this opportunity.

References

Yahyazadeh, M., Podder, P., Hoque, E., & Chowdhury, O. (2019). Expat. *Proceedings of the 24th ACM Symposium on Access Control Models and Technologies - SACMAT 19*. doi:10.1145/3322431.3325107

Zhang, L., He, W., Martinez, J., Brackenbury, N., Lu, S., & Ur, B. (2019). AutoTap: Synthesizing and repairing trigger-action programs using LTL properties. *Proceedings of the 41st International Conference on Software Engineering*. doi:10.1109/ICSE.2019.00043

Alrawi, O., Lever, C., Antonakakis, M., & Monrose, F. (2019). SoK: Security Evaluation of Home-Based IoT Deployments. S&P 2019.

Fernandes, E., Jung, J., & Prakash, A. (2016). Security Analysis of Emerging Smart Home Applications. 2016 IEEE Symposium on Security and Privacy (SP). doi:10.1109/sp.2016.44

Fernandes, E., Rahmati, A., Jung, J., & Prakash, A. (2018). Decentralized Action Integrity for Trigger-Action IoT Platforms. Proceedings 2018 Network and Distributed System Security Symposium. doi:10.14722/ndss.2018.23119

Elucidating the role of angiopoietin-like protein 5 in plasma triglyceride metabolism

Kush Chaudhari[1], Shwetha Shetty[2,3], Brandon S. J. Davies[2,3]

Biotechnology High School[1], Fraternal Order of Eagles Diabetes Research Center[2], The University of Iowa[3]

University of Iowa Carver College of Medicine
University of Iowa Health Care

Introduction

Medical Implications

- Fatty acids not used for immediate calories are stored as triglycerides; some circulate in the bloodstream
- Elevated plasma triglyceride levels leads to the formation of **atherosclerotic** plaques (Pruthi et al., 2018)
- Results in cardiovascular diseases (heart disease and stroke)

Objective: To determine the role of ANGPTL5 in LPL inhibition and plasma triglyceride metabolism.

Lipoprotein Lipase (LPL)

- Triglycerides are carried by lipoproteins in the bloodstream (chylomicrons/very low-density lipoproteins)
- LPL **hydrolyzes triglycerides** within lipoproteins (Chi et al., 2015)

ANGPTL5

- Expressed in humans, not mice
- Association between low plasma triglyceride levels and rare loss-of-function mutations of ANGPTL5 (Romeo et al., 2009)

Angiopoietin-like proteins (ANGPTLs)

- Family of proteins involved in angiogenesis, metastasis, and **lipid metabolism** (Carbone et al., 2018)

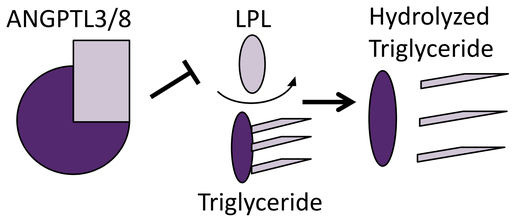

Figure 1: ANGPTL3-8 form a complex to inhibit LPL and increase plasma triglycerides

- ANGPTL4 → LPL inhibition
- ANGPTL3-8 → LPL inhibition

Experimental Design

Midipreparation → Sanger Sequencing to ensure correct nucleotide sequence

↓

Transient **transfection** of HEK293T Cells (V5/Strep-tagged) to produce protein

↓

Media/Cell Lysate **Collection** for secreted/non-secreted protein

↓

Western Blot to visualize/quantify protein

↓

LPL Activity Assay with EnzChek LPL Substrate to observe inhibitory effects

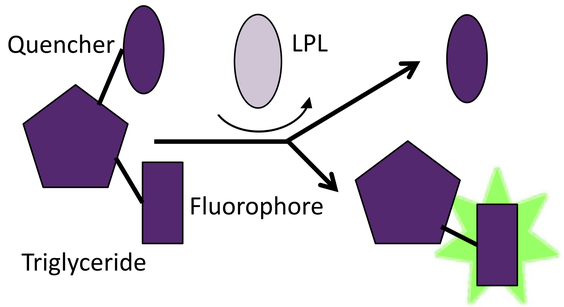

Figure 2: LPL cleaves the quencher off of EnzChek triglycerides to produce measurable fluorescence

Results: Fluorescent Immunodetection of ANGPTL5

Preliminary Western Blots of ANGPTL5

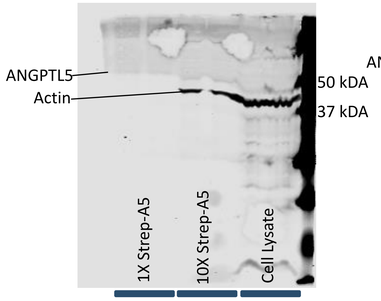

Figure 3: Western blot of Strep-tagged ANGPTL5 in conditioned media and cell lysate

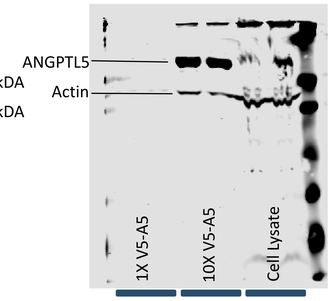

Figure 4: Western blot of V5-tagged ANGPTL5 in conditioned media and cell lysate

LPL Activity Assay

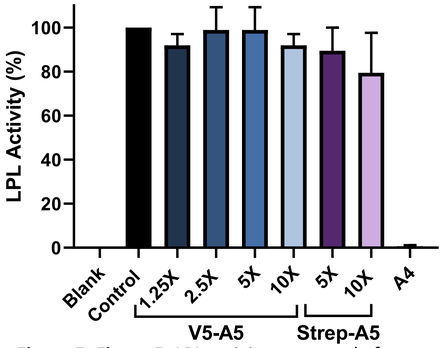

Figure 5: **Figure 5**: LPL activity measured after treatment with increasing amount of ANGPTL5. Activity was normalized to control media

Secondary Western Blots of ANGPTL5-8

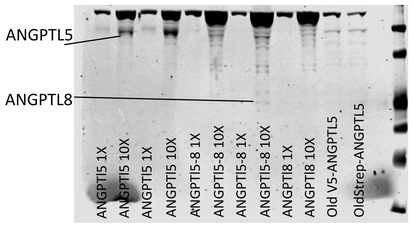

Figure 6: Western blot of secreted ANGPTL5 and co-transfected with ANGPTL8 in conditioned media with purified DNA

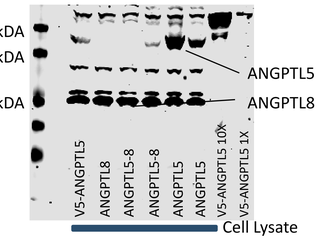

Figure 7: ANGPTL5 co-transfected with ANGPTL8 in cell lysate and with purified DNA

Co-transfected LPL Activity

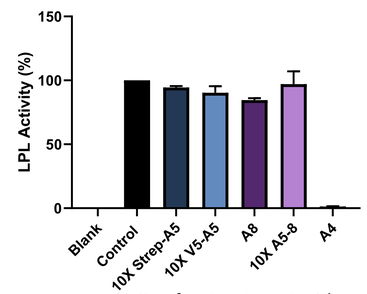

Figure 8: LPL activity after treatment with ANGPTL5 alone and/or co-transfected with ANGPTL8

Conclusions/Implications

1. ANGPTL5 has no significant effect on LPL activity
2. ANGPTL5, in complex with ANGPTL8, does not inhibit LPL; may enhance ANGPTL8 secretion
3. ANGPTL5 is not secreted effectively

Development of Atherosclerotic Therapeutics

- By determining how ANGPTL5 is involved in triglyceride metabolism, cardiovascular therapeutics become plausible.

Future Directions

Aim 1: Perform endothelial lipase inhibition assays with ANGPTL5
Aim 2: Co-transfect with ANGPTL4 (and other family members) to determine if ANGPTL5 counteracts inhibitory effects

Acknowledgements

Special thanks to Shwetha Shetty and Dr. Davies, the Belin Blank Center, and the Department of Biochemistry of Carver College for their guidance and resources during this project.

References

Carbone, C., Piro, G., Merz, V., Simionato, F., Santoro, R., Zecchetto, C., ... & Melisi, D. (2018). Angiopoietin-like proteins in angiogenesis, inflammation and cancer. *International Journal of Molecular Sciences*, *19*(2), 431.

Chi, X., Britt, E. C., Shows, H. W., Hjelmaas, A. J., Shetty, S. K., Cushing, E. M., ... & Davies, B. S. (2017). ANGPTL8 promotes the ability of ANGPTL3 to bind and inhibit lipoprotein lipase. *Molecular Metabolism*, *6*(10), 1137-1149.

Chi, X., Shetty, S. K., Shows, H. W., Hjelmaas, A. J., Malcolm, E. K., & Davies, B. S. (2015). Angiopoietin-like 4 modifies the interactions between lipoprotein lipase and its endothelial cell transporter. *Journal of Biological Chemistry*, *290*(19), 11865-11877.

Cushing, E. M., Chi, X., Sylvers, K. L., Shetty, S. K., Potthoff, M. J., & Davies, B. S. (2017). Angiopoietin-like 4 directs uptake of dietary fat away from adipose during fasting. *Molecular Metabolism*, *6*(8), 809-818.

Pruthi, S., Mankad, R., Jiminez, F., Castro, R., Wilkinson, J., & Litin, S. (2018, September 13). Can triglycerides affect my heart health?

Romeo, S., Yin, W., Kozlitina, J., Pennacchio, L. A., Boerwinkle, E., Hobbs, H. H., & Cohen, J. C. (2009). Rare loss-of-function mutations in ANGPTL family members contribute to plasma triglyceride levels in humans. *The Journal of Clinical Investigation*, *119*(1), 70-79.

Role of median raphe serotonergic neurons in seizure induced death

Amelia Chen[1], Molly Matkovich[2,3], Rui Li[3] & Gordon F. Buchanan[3,4]
[1]SSTP, [2]Department of Mathematics, University of Iowa [3]Department of Neurology,
[4]Iowa Neuroscience Institute, University of Iowa Carver College of Medicine

Introduction

- Sudden unexpected death in epilepsy (SUDEP) is defined as sudden, unexpected, non-traumatic, and non-drowning death in a patient with epilepsy[1].
- It is the leading cause of death among patients with refractory epilepsy[2] and is second only to stroke in terms of potential years of life lost among all neurological conditions[3].
- SUDEP usually happens after a generalized tonic-clonic seizure.
- Interestingly, there is a sleep state-dependence of seizures: they rarely occur during the rapid eye movement (REM) sleep[4], thus suggesting that REM is protective.
- REM sleep and its characteristic theta activity are both regulated by serotonin (5-HT)[5].
- Mice with a genetic deletion of serotonin have higher mortality rates[6].
- 5-HT is produced in several sites in the brain, including median raphe nucleus (MRN)[6].

Objective

Determine whether stimulating MRN 5-HT neurons **reduces** seizure-induced death.

Method

Experimental Procedures

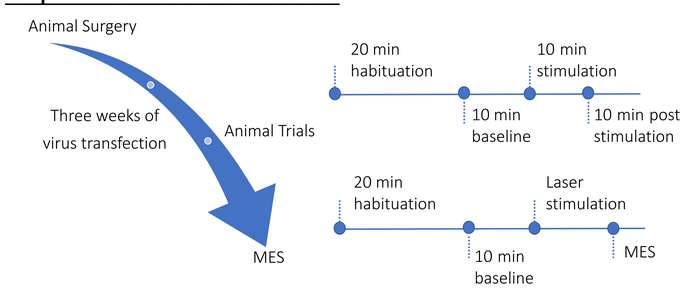

- Mice were injected with AAV-ChR2 (activation of 5-HT neurons) or AAV-Arch (inhibition of 5-HT neurons).
- 2-3 days habituation before MES.
- Photo-stimulation lasts at least ten minutes before seizure induction, which is given during wake period.
- MES parameter: 30 mA, 0.2 s, 60 Hz, sine wave.

Results

Effects of optogenetic manipulation of MRN 5-HT neurons

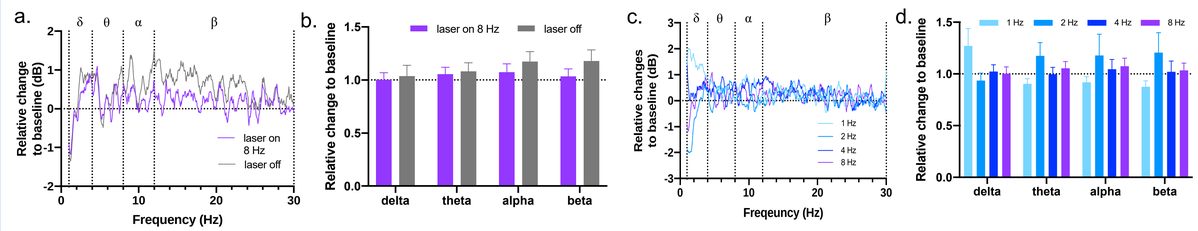

Fig 1. Effects of activation of MRN 5-HT neurons at different frequencies via ChR2. ***(a, b)*** EEG power spectral density ***(a)*** and EEG power at different frequency bands ***(b)*** during and after 8 Hz stimulation in MRN-ChR2 mice. ***(c, d)*** A summary of EEG power spectral density ***(c)*** and EEG power at different frequency bands ***(d)*** during 1 Hz, 2 Hz, and 8 Hz stimulation. All values shown have been subjected to baseline correction.

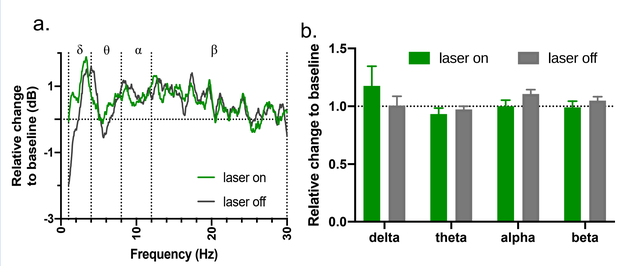

Fig 2. Effects of Arch-mediated inhibition of MRN 5-HT neurons on EEG. ***(a, b)*** EEG power spectral density ***(a)*** and EEG power at different frequency bands ***(b)*** during and after stimulation. All values shown have been subjected to baseline correction.

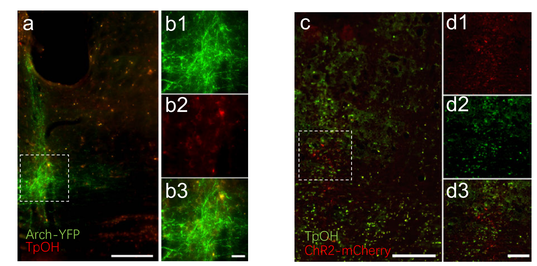

Fig 3. Verification of virus expression. ***(a, b)*** Expression of Arch-YFP (green) and TpOH (red) in median raphe from a Pet1-Cre MRN-Arch mouse. ***(c, d)*** Expression of ChR2-mCherry (red) and TpOH (green) in median raphe from a Pet1-Cre MRN-ChR2 mouse. Scale bars in (a, c), 200 μm; in (b, d), 50 μm.

Activation of 5-HT neurons decreases mortality rate in MES seizure mode

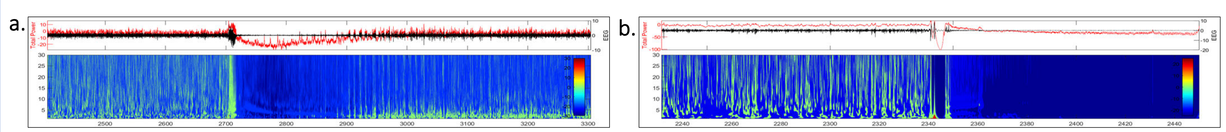

Fig 4. Time-frequency analyses from one mouse that survived an MES seizure ***(a)***, and from one that died ***(b)***.

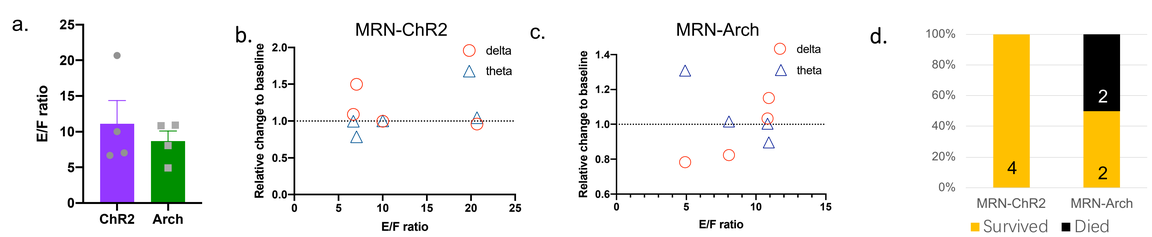

Fig 5. Effects of manipulation of MRN 5-HT neurons on MES outcome. ***(a)*** Seizure severity (extension-flexion (E/F) ratio) of MRN-ChR2 and MRN-Arch mice after at least 10 min stimulation. ***(b, c)*** Relationship between E/F ratio and EEG power changes at delta and theta bands relative to baseline for MRN-ChR2 mice ***(b)*** and MRN-Arch mice ***(c)***. ***(d)*** Mortality rate of MRN-Arch mice and MRN-ChR2 mice after MES. Numbers represent n's.

Summary

- Activation of MRN 5-HT neurons via ChR2 affected the brain EEG in a stimulation frequency dependent manner.
- Inhibition of MRN 5-HT neurons increased delta power, but reduced theta power.
- Manipulation of MRN 5-HT neurons affected the outcome of MES seizure.

Conclusion

More mice survived MES seizure when MRN 5-HT neurons were activated compared to when 5-HT neurons were inhibited.

Future Directions

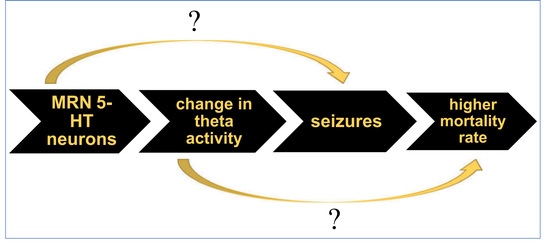

References

1. Nashef L., et al. (2012) Unifying the definitions of sudden unexpected death in epilepsy. *Epilepsia, 53*(2), 227-33, doi:10.1111/j.1528-1167.2011.03358.x
2. Devinsky., et al. (2016) Sudden unexpected death in epilepsy: epidemiology, mechanisms, and prevention. *The Lancet Neurology, 15*(10), 1075-88, doi:10.1016/S1474-4422(15)00379-8
3. Thurman D. J., et al. (2014) Sudden unexpected death in epilepsy: assessing the public health burden. *Epilepsia, 55*(10), 1479-85, doi:10.1111/epi.12666
4. Ng M., et al. (2013) Why are seizures rare in rapid eye movement sleep? Review of the frequency of seizures in different sleep stages. *Epilepsy Research and Treatment,* doi:10.1155/2013/932790
5. Monti J.M., et al. (2011) Serotonin control of sleep wake behavior. *Sleep Medicine Reviews, 15*(4), 269-81, doi:10.1016/j.smrv.2010.11.003
6. Buchanan G.F., et al. (2014) Serotonin neurons have anti-convulsant effects and reduce seizure-induced mortality. *The Journal of Physiology, 592*(19), 4395-410, doi:10.1113/jphysiol.2014.277574

Supported by the SSTP, NIH/NINDS R01 NS095842, and the Beth L. Tross Epilepsy Professorship

Exploring genetic interactions between an epilepsy mutant and Alzheimer's disease in flies

Richard Deng[1]; Pierre Yan[2]; Krishna Madhav Nukala[3]; Anthony Lilienthal[3]; Alexander Bassuk, M.D., Ph.D.[3]; J. Robert Manak, Ph.D.[3]
[1]Dougherty Valley High School, [2]Haddonfield Memorial High School, [3]The University of Iowa

Introduction

Alzheimer's Disease is a neurological disorder that affects 1 in 10 people over the age of 65. This condition has been linked to improper processing of the APP (amyloid precursor protein) and is known to be associated with widespread neurodegeneration and epilepsy. In *Drosophila*, another gene in the Planar Cell Polarity (*PCP*) complex called *prickle (pk)* (Figure 1a) has been associated with both of these phenotypes. When the *prickle-spiny-legs* isoform (pk^{sple}) is mutated, the fly exhibits seizures which mimic those found in human *PRICKLE* patients (Ehaideb et al., 2016). Conversely, when the *prickle-prickle* isoform (pk^{pk}) is mutated, preliminary data suggests that widespread neurodegeneration is observed in the *Drosophila* brain. Further connections between Alzheimer's and PCP were found in previous work by Soldano et al (2013), who demonstrated that the *Van gogh (Vang)* gene also interacts with *appl* (the *Drosophila* orthologue of APP) both genetically and physically during neurodevelopment (Figure 1B). All three genes, *Vang*, *appl,* and *pk*, have been associated with neuronal connectivity; thus, we sought to determine whether the pk^{sple} isoform interacts genetically with *appl.*

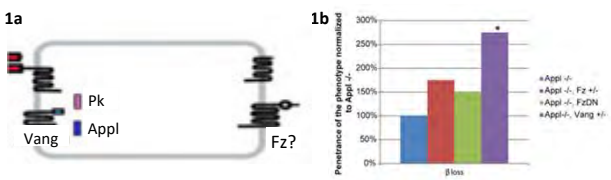

Soldano et al., 2013

Figure 1. (1a) A schematic showing the PCP proteins Vang and Prickle potentially interacting with the Alzheimer's protein Appl inside a neuron to promote proper neuronal development. (1b) This graph investigates the interaction between the $appl^d$ mutant and multiple mutants in the PCP complex during the development of the mushroom body of Drosophila. Soldano et al. demonstrated that the *appl* gene shows statistically greater disruption to proper neuron development when *vang* gene is also disrupted, hence, proving *appl* and *vang* genetically interact with each other. (figure adapted from Soldano et al., 2013)

Research Objective

To investigate the potential genetic interaction between an epilepsy mutant (pk^{sple}) and an Alzheimer's gene (*appl*) during embryonic neuronal development

Methods and Materials

1. Genotypes assayed: *WT* (+/+), pk^{sple1}/pk^{sple1} (sple/sple), $appl^d/appl^d$, and $appl^d/appl^d$;*sple/sple*
   - All outcrossed to a w^{1118} background
2. Perform two 2-hour pre-lays to stimulate lays and synchronize embryo aging
3. Prepare 14-16 hour embryos for staining by removing chorions with bleach
4. Fix embryos in a 4% paraformaldehyde
5. Remove vitelline membranes by vigorously shaking embryos in methanol
6. Use immunohistochemistry (IHC) to stain for 22C10, a marker for peripheral neurons, and Fasciculin II (FasII), a marker for motor neurons
7. Image embryos with confocal microscopy and quantify the number of neuronal defects in each line

Preliminary Results

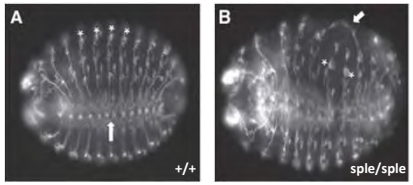

Tao, Manak, Sowers et al., 2011

Figure 2. Staining of PNS and VNC using 22C10 antibodies. Asterisks indicate normal neuron extension positions (B) depicts a sple mutant with neuron extension defects (Tao, Manak, Sowers et al., 2011).

Results

Genotype	22C10	FasII	Total
+/+	70	38	108
sple/sple	55	46	101
$appl^d/appl^d$	56	50	106
$appl^d/appl^d$; *sple/sple*	36	3	39
Total	217	137	**354**

Results (cont.)

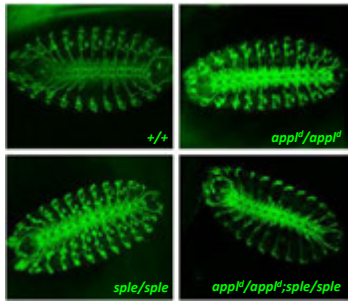

Figure 3. IHC of *Drosophila* embryos showing normal neuronal connectivity, all stained with the antibody 22C10. Brightness and contrast are modified for ease of viewing.

Conclusions

- No defects were observed in any of the genetic lines: +/+, sple/sple, $appl^d/appl^d$, and $appl^d/appl^d$;*sple/sple*
- Given that only 4.7% of embryos imaged by Tao, Manak, Sowers et al., had neuronal wiring defects, our study was likely underpowered and requires more samples to potentially reveal defects
- There is also a possibility of no genetic interaction between *appl* and the *sple* isoform of *prickle*
- Alternatively, the phenotype of these mutants may be revealed when looking at later developmental stages in *Drosophila*

Future Directions

- Increase the sample size of each line
- Improve techniques to maximize the number of imageable embryos
- Determine whether there is an interaction between *prickle* and *appl* in mice

References

1. Ehaideb, S. N., Iyengar, A., Ueda, A., Iacobucci, G. J., Cranston, C., Bassuk, A. G., … Manak, J. R. (2014). Prickle modulates microtubule polarity and axonal transport to ameliorate seizures in flies. *Proceedings of the National Academy of Sciences of the United States of America*, *111*(30), 11187–11192. doi:10.1073/pnas.1403357111
2. Noebels J. (2011). A perfect storm: Converging paths of epilepsy and Alzheimer's dementia intersect in the hippocampal formation. Epilepsia, 52 Suppl 1(Suppl 1), 39–46. doi:10.1111/j.1528-1167.2010.02909.x
3. Soldano A, Okray Z, Janovska P, et al. (2013). The Drosophila homologue of the amyloid precursor protein is a conserved modulator of Wnt PCP signaling. PLoS Biol. 2013;11(5):e1001562. doi:10.1371/journal.pbio.1001562
4. Tao, H., Manak, J. R., Sowers, L., Mei, X., Kiyonari, H., Abe, T., … Bassuk, A. G. (2011). Mutations in prickle orthologs cause seizures in flies, mice, and humans. *American journal of human genetics*, *88*(2), 138–149. doi:10.1016/j.ajhg.2010.12.012

Targeting Pancreatic Neuroendocrine Tumors With Drugs that Inhibit RABL6A Regulated Kinases

Aditi Deokar[1], Umesalma Shaikamjad, PhD[2], Dawn Quelle, PhD[2]
[1]Boston University Academy, Boston, MA, [2]Dept. of Pharmacology, University of Iowa, Iowa City, IA

The University of Iowa

Belin-Blank Center

Background

Pancreatic neuroendocrine tumors (PNETs)

- Rare and slow growing cancers
  - Often not diagnosed until advanced
  - Limited treatment options for metastasis
- Better understanding of genes and pathways behind PNET pathogenesis needed for improved biomarkers and therapies

RABL6A

- Novel cancer-promoting protein upregulated in PNETs (Hagen et al., 2014)
- Mechanisms of action only partly understood
- Kinome analyses (unpublished) suggest it activates CDK16 and EphA2 kinases

Objective: To test the hypotheses that…

1. RABL6A regulates CDK16 and EphA2
2. CDK16 and EphA2 can be inhibited by the drugs dabrafenib (Phadke et al., 2017) and ALW-41-27 (Amato et al, 2014), respectively, in PNET cells.

Results

Western blots of RABL6A regulation of CDK16

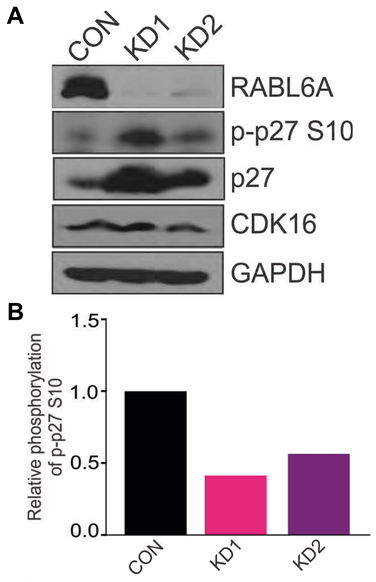

Figure 2: (A) Western blot analyses of indicated proteins in both control and RABL6A-knockdown (KD1, KD2) BON-1 cells. (B) Quantification of relative phosphorylation of p27 at S10 in control and RABL6A-knockdown BON-1 cells.

Schematic of putative RABL6A-regulated kinases / mechanisms

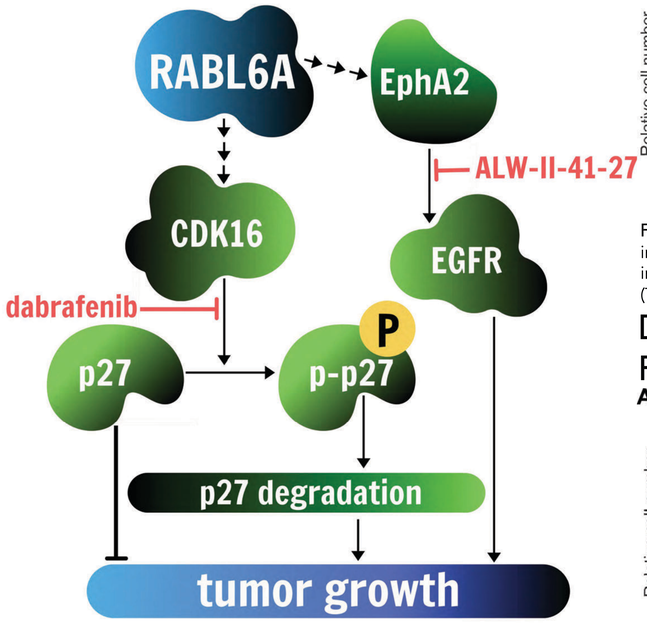

Figure 3: Hypothetical RABL6A pathways. RABL6A may promote tumor growth and proliferation by upregulating CDK16, which phosphorylates the tumor suppressor p27 at Ser10, inducing p27 degradation. CDK16 can be inhibited by the drug dabrafenib. The tumor-promoting kinase, EphA2, possibly also regulated by RABL6A, can be inhibited by the drug ALW-II-41-27.

Drug response assays in parental PNET cells

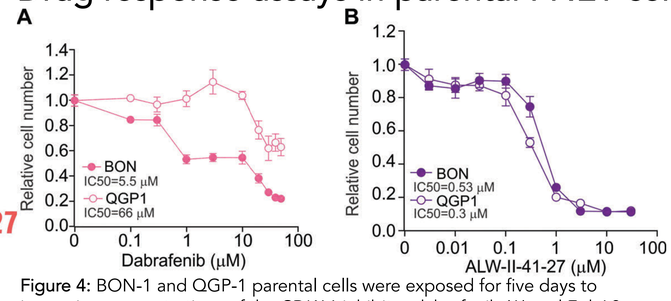

Figure 4: BON-1 and QGP-1 parental cells were exposed for five days to increasing concentrations of the CDK16 inhibitor dabrafenib (A) and EphA2 inhibitor ALW-II-41-27 (B) and relative cell proliferation assayed using alamarBlue[R] (Thermo Fisher Scientific).

Drug response assays in RABL6A knockdown PNET cells

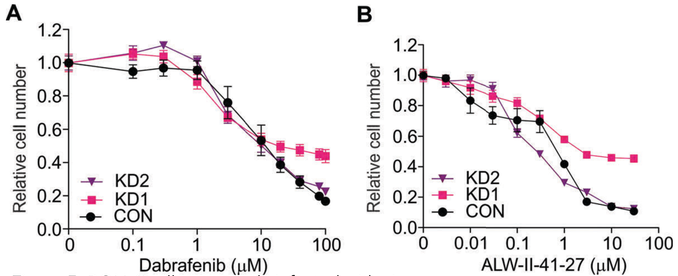

Figure 5: BON-1 cells transiently infected with viruses expressing empty vector (CON) or RABL6A shRNAs (KD1 and KD2) were exposed for five days to increasing concentrations of the CDK16 inhibitor dabrafenib (A) and EphA2 inhibitor ALW-II-41-27 (B) and relative cell proliferation assayed using alamarBlue[R] (Thermo Fisher Scientific).

Methods

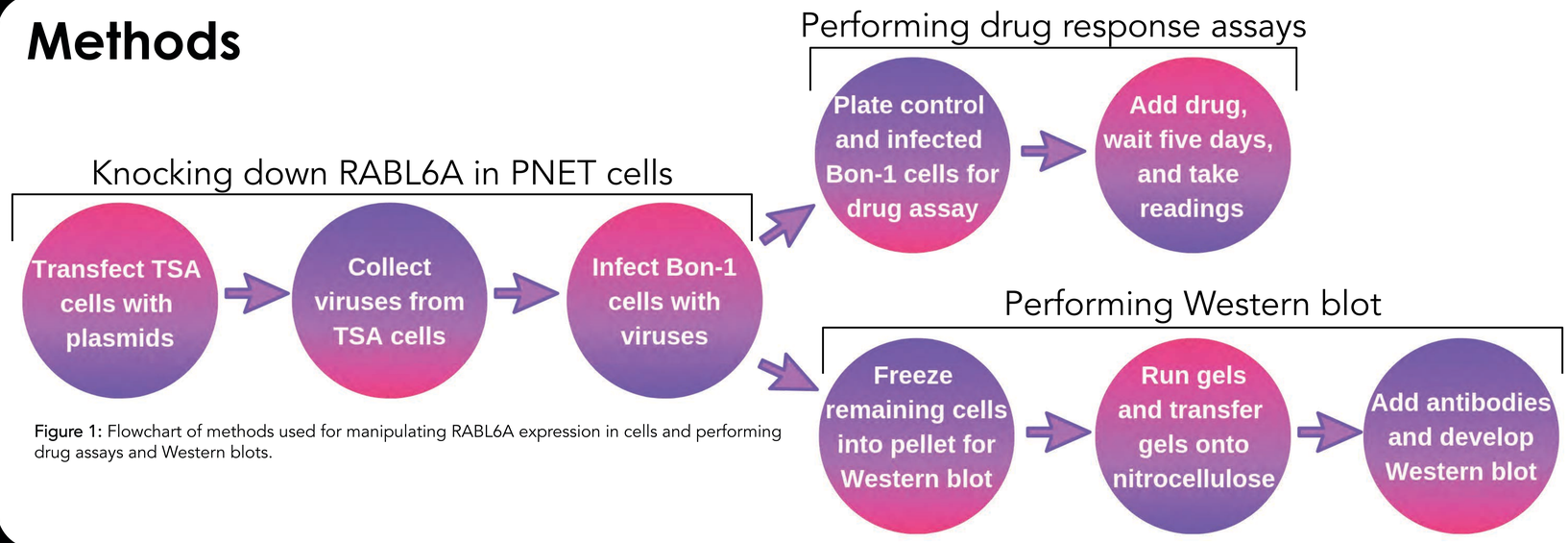

Figure 1: Flowchart of methods used for manipulating RABL6A expression in cells and performing drug assays and Western blots.

Conclusions

- RABL6A promotes p27-S10 phosphorylation, possibly through CDK16 activation
- ALW-II-41-27 effectively suppresses PNET cell growth while dabrafenib selectively reduces BON-1 viability

Future Directions:

- Is CDK16 required for p27 regulation by RABL6A?
  - Determine if CDK16 loss or overexpression alters the effect of RABL6A knockdown on p27 expression and S10 phosphorylation
  - Investigate the role of other p27 kinases, such as AKT, in the RABL6A-p27 relationship
- Validate drug actions by performing kinase assays

Acknowledgements

Special thanks to Dr. Umesalma Shaikamjad, Dr. Dawn Quelle, and the rest of the Quelle group for their guidance and support during this project. I would also like to thank SSTP and the Belin-Blank Center for giving me this amazing opportunity.

References

Amato, K. R., Wang, S., Hastings, A. K., Youngblood, V. M., Santapuram, P. R., Chen, H., … Chen, J. (2014). Genetic and pharmacologic inhibition of EPHA2 promotes apoptosis in NSCLC. *Journal of Clinical Investigation*, *124*(5), 2037–2049. https://doi.org/10.1172/JCI72522

Hagen, J., Muniz, V. P., Falls, K. C., Reed, S. M., Taghiyev, A. F., Quelle, F. W., … Quelle, D. E. (2014). RABL6A Promotes G 1 − S Phase Progression and Pancreatic Neuroendocrine Tumor Cell Proliferation in an Rb1-Dependent Manner. *Cancer Research*, *74*(22), 1–10. https://doi.org/10.1158/0008-5472.CAN-13-3742

Phadke, M., Remsing Rix, L. L., Smalley, I., Bryant, A. T., Luo, Y., Lawrence, H. R., … Smalley, K. S. M. (2017). Dabrafenib inhibits the growth of BRAF-WT cancers through CDK16 and NEK9 inhibition. *Molecular Oncology*, *12*(2018), 74–88. https://doi.org/10.1002/1878-0261.12152

Validation of next-generation sequencing and applications in sex-specific genetic analysis in autism

Katherine Dong[1], Taylor Thomas[2], & Jacob J. Michaelson, Ph.D.[2]

[1]Novi High School, Michigan; [2]Department of Psychiatry, University of Iowa

Belin-Blank Center, College of Education, The University of Iowa

The University of Iowa

Background

Autism Spectrum Disorder

- Autism spectrum disorder (ASD) is a neurodevelopmental disorder
  - repetitive behaviors and difficulties with social communication (Ferri, Abel, & Brodkin, 2018).
- Exact etiology unknown
  - Complex condition → polygenic, influenced by rare and common variations (Gaugler et al., 2014)

Sex bias in ASD

- Sex bias with 4:1 male to female ratio (Werling, 2016)
- Cause is unclear, multiple theories
  - Female protective effect (FPE): females are more protected from ASD than males
  - Sex hormones may have influence

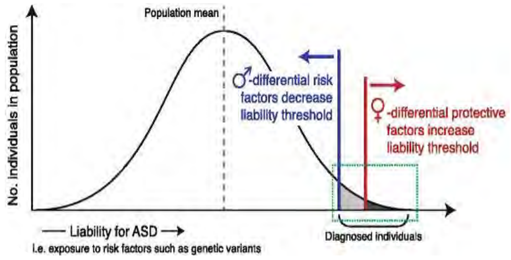

https://bsd.biomedcentral.com/articles/10.1186/s13293-016-0112-8

Figure 1: Model of FPE: Due to a protective effect, females have a higher liability threshold (i.e. require more deleterious factors) for ASD symptoms (Werling, 2016).

Research Objectives

1. **To use NGS data to identify genes differentiated between ASD males and females that may contribute to a female protective effect, and therefore the sex bias in Autism Spectrum Disorder**
2. **To validate rare genetic variants found in a cohort**

SPARK & Illumina Sequencing

Simons Foundation Powering Autism Research for Knowledge (SPARK)

- Project using a large cohort of medical and genetic data for ASD research

Next-Generation Sequencing (NGS)

- High throughput methods used to sequence DNA
- Illumina sequencing: type of NGS
  - Efficient for large cohorts
  - High error rate – needs validation (Goodwin, McPherson, & McCombie, 2016)
  - SPARK uses Illumina sequencing

Validation of Next-Generation Sequencing

Methods:

Sanger sequencing → Used to accurately sequence fragment with variant

Primer Design

gene	chrom	start	ref	alt
ZFYVE28	chr4	2307236	T	TCCTC

Table 1: Location of variant from NGS sequence

PCR Amplification & Gel Electrophoresis

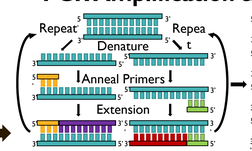

Figure 2: Diagram of PCR process: DNA is amplified over many cycles using template strands.

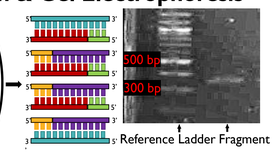

Figure 3: Gel image of fragment

- Primers designed using sequence around variant (indel in this case)
- Alternate sequence: indel being validated and compared to reference sequence

- PCR using primers
  - amplify sequence with indel
- Gel electrophoresis confirmed correct fragment size

Sanger Sequencing

PCR in the presence of fluorescent, chain-terminating nucleotides

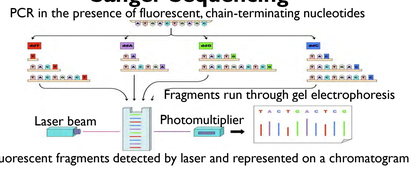

Fluorescent fragments detected by laser and represented on a chromatogram

http://www.vce.bioninja.com.au/aos-3-heredity/molecular-biology-technique/sequencing.html

Figure 4: DNA Sequencing via the Sanger Method: DNA is sequenced using fragments formed by chain-terminating dideoxynucleotides.

- Sanger sequencing used to sequence the fragment
  - Validate indel found by NGS

Sequence alignment

Figure 5: BLAST sequence alignment

- Basic Local Alignment Tool (BLAST): tool used to compare sequences
- Compared Sanger sequencing result to reference sequence
  - Identify variations and validate indel identified by NGS

Results:

- Observed indel from the NGS sequence was not a variant in the sample, but an error in the NGS process

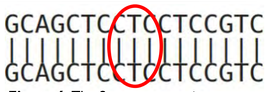

Figure 6: The Sanger sequencing sequence matches the reference sequence, so there is no variant.

Sex-Specific Genetic Analysis in Autism

Methods:

CADD Scores – Combined Annotation-Dependent Depletion

- Deleteriousness of a variant (Rentzsch, Witten, Cooper, Shendure, & Kircher, 2018)
- Maximum CADD score per gene used for analysis

- Selected genes involved in sex hormone pathways and autism categories 1-6 from *SFARI Gene* database

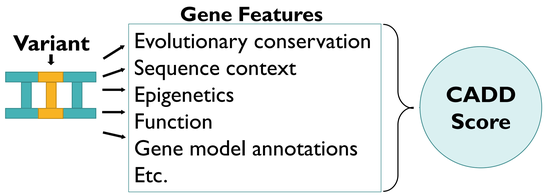

Figure 7: A CADD score combines multiple gene features to score the deleteriousness of a variant (Rentzsch, Witten, Cooper, Shendure, & Kircher, 2018).

Significance Tests

- Wilcoxon rank sum tests and t-tests on maximum CADD scores for each gene
- Identify significantly different scores between severe ASD male and female probands
- Significant genes on sex chromosomes filtered out

Sex-Specific Genetic Analysis in Autism (cont.)

Results:

Genes with significantly different max CADD scores between ASD males and females in Wilcoxon rank sum test and/or t-test

Gene	Gene group	adj. p-value Wilcoxon test	adj. p-value t-test	Mean severe ASD males (n=906)	Mean severe ASD females (n=214)
KMT2A ***	autism category 1	0.01857	0.005439	8.8266	7.0639
ALAD ***	cortisol	0.03803	0.021661	9.0857	10.797
HSD11B2 **	cortisol	0.03051	0.2470	3.6249	2.6196
TRPM1**	autism category 3	0.04489	0.3074	20.974	22.344
AACS *	testosterone	0.05282	0.02011	8.2288	6.9502
SHBG *	testosterone, estradiol	0.05356	0.02176	6.3184	8.1448
KRT26 *	autism category 4	0.1584	0.02216	7.5587	5.0199
GBA *	testosterone, cortisol, estradiol	0.1025	0.03320	5.3513	4.4664
CNTN4 *	autism category 2	0.1078	0.04129	16.838	17.350
SLC22A3 *	autism category 5	0.06612	0.04475	12.826	13.572

Note: Significant at p ≤ 0.05 level
**= Significant adjusted p-value on t-test*
*** = Significant adj. p-value on Wilcoxon rank sum test*
**** = Significant adj. p-value on both tests*

Table 2: Autosomal genes with significant adjusted p-values in Wilcoxon rank sum test or t-test when comparing max CADD scores between males and females.

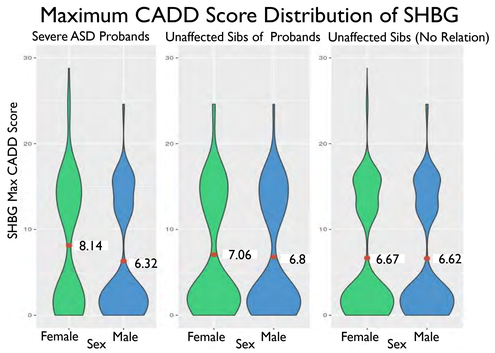

Figure 8: Distribution of SHBG max CADD scores: There is visible difference in the distribution between severe ASD males and females that is not present in either group of unaffected siblings.

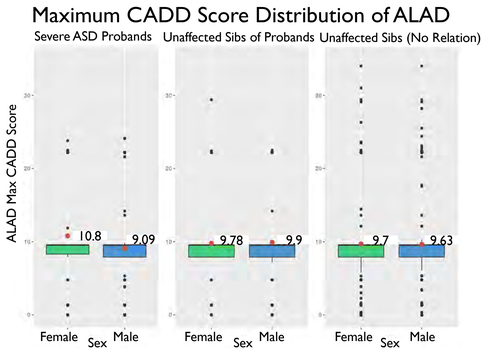

Figure 9: Distribution of ALAD max CADD scores: There is visible difference in the distribution between severe ASD males and females that is not present in either group of unaffected siblings.

- 10 significant genes among both tests
  - 2 significant in both tests
  - 5 associated with hormonal pathways
- Differences not observed among unaffected siblings

Conclusions

- Deleteriousness of some sex hormone genes differ between ASD males and females
  - May contribute to FPE and sex bias
  - Future studies investigating these genes
- Observed indel invalidated
  - Important to validate variants → Validate variants found in computational analyses

Acknowledgements

I would like to thank Taylor Thomas for her mentorship and guidance, Dr. Jacob Michaelson for the opportunity to conduct research in his lab, as well as the entire Michaelson Lab and the University of Iowa Carver College of Medicine, Department of Psychiatry. Also special thanks to all involved in the SSTP program for providing this amazing opportunity.

References

Ferri, S. L., Abel, T., & Brodkin, E. S. (2018). Sex differences in autism spectrum disorder: a review. *Current Psychiatry Reports*, *20*(2). doi:10.1007/s11920-018-0874-2

Gaugler, T., Klei, L., Sanders, S. J., Bodea, C. A., Goldberg, A. P., Lee, A. B., . . . Buxbaum, J. D. (2014). Most genetic risk for autism resides with common variation. *Nature Genetics*, *46*(8), 881-885. doi:10.1038/ng.3039

Goodwin, S., Mcpherson, J. D., & Mccombie, W. R. (2016). Coming of age: Ten years of next-generation sequencing technologies. *Nature Reviews Genetics*, *17*(6), 333-351. doi:10.1038/nrg.2016.49

Rentzsch, P., Witten, D., Cooper, G. M., Shendure, J., & Kircher, M. (2018). CADD: Predicting the deleteriousness of variants throughout the human genome. *Nucleic Acids Research*, *47*(D1). doi:10.1093/nar/gky1016

Werling, D. M. (2016). The role of sex-differential biology in risk for autism spectrum disorder. *Biology of Sex Differences*, *7*(1). doi:10.1186/s13293-016-0112-8

A Serious Game for Flood Mitigation: Game Engine Development

Joshua Feuerstein

INTRO:

- Video games are a medium that enhance **user engagement** and **encourage learning**
- Globally, and in Iowa especially, flood alerts are very common: it is of the utmost importance for residents to make **educated decisions** based on **real-time water body data**, such as finding shelter, evacuating, and planning ahead
- The use of this game gives users an opportunity to **teach themselves flood protection and mitigation techniques**, such that they and their belongings are **protected in the event of a flood**.

METHODS:

- **Design**
  - Designed in plain, engine-less JavaScript
  - Created to seamlessly integrate real time flood data with game logic to create an educational yet enjoyable user experience
  - Use of simple, colorful graphics and easy to interpret menu system make the game appealing to anyone with any video gaming background
- **Google Maps API integration**
  - The entire game is based on the Google Maps API's map overlay system
  - Tiles are overlaid on top of a real time Google Map
  - This not only allows for IFIS data integration but allows for the second main feature of the game, its global scale
- **Global adaptability**
  - A main feature of the game is its changing user-by-user experience
  - Each new player can select to play their game anywhere in the world, using the game's automatic level generation along with the Google Maps API and global flood data.

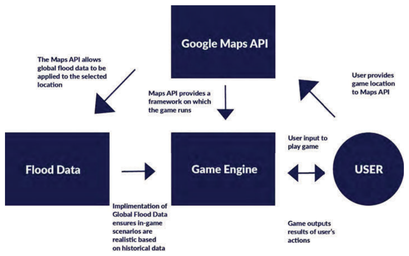

Flowchart of the project's workflow

Video Games can be used to **educate** people about **flood prevention** and **mitigation.**

RESULTS:

- Game engine structure beginning to be developed
- Accounts for future inclusion of planned features, such as global flood data and global scalability
- Concrete game design centered around optimally entertaining and educational experience for the user

A screen capture of the project in its current state

FUTURE IMPLICATIONS:

- Once fully developed, this game will provide an educational experience for the user, allowing them to experiment with different flood remediation techniques
- The game will hopefully be able to eventually reach all its initial goals, including global scalability and global flood data incorporation

REFERENCES/ACKNOWLEDGEMENTS

Bosschaart, A., van der Schee, J., & Kuiper, W. (2016). Designing a flood-risk education program in the Netherlands. Journal of Environmental Education, 47(4), 271–286. https://doi.org/10.1080/00958964.2015.1130013

Din, Z. U., & Gibson, G. E. (2019). Serious games for learning prevention through design concepts: An experimental study. Safety Science, 115, 176–187. https://doi.org/10.1016/j.ssci.2019.02.005

Garneli, V., Giannakos, M., & Chorianopoulos, K. (2017). Serious games as a malleable learning medium: The effects of narrative, gameplay, and making on students' performance and attitudes. British Journal of Educational Technology, 48(3),842–859. https://doi.org/10.1111/bjet.12455

Stop disasters game. (2018). Retrieved July 23, 2019, from UNDRR website: https://www.stopdisastersgame.org/

Special and gracious thanks to Dr. Ibrahim Demir, Yusuf Sermet, and the Hydroinformatics lab for their help and resources towards my project.
I would also like to thank SSTP and the Belin-Blank center for this research opportunity.

Joshua Feuerstein[1], Yusuf Sermet[2], Ibrahim Demir[2]

[1]Amity Regional High School,
[2]Hydraulics Lab, IIHR Hydroscience and Engineering, University of Iowa

IIHR Hydroscience & Engineering

UIHI Lab

The University of Iowa | Belin-Blank Center

3D Printing of Tunable Piezoelectric Components via Ceramic Stereolithography

Yash Fichadia[1,2], Li He[1], Xuan Song[1]

1. Department of Mechanical and Industrial Engineering 2. Millard North High School

Background

- A big part of my project is additive manufacturing, commonly known as 3D printing
- Most people know about one 3D printing method, fusion deposition modeling or FDM
  - Plastic filament is melted into layers that stack together
- Stereolithography is another 3D printing method that uses an ultraviolet light and photosensitive materials like liquid resin
  - The UV light hardens certain areas of each resin layer, creating a solid shape (Chen et al, 2019)
- Stereolithography allows printing with materials like ceramics
  - Ceramics both can have piezoelectric properties and be biocompatible, but they can also be very brittle
- Piezoelectric properties mean that a change in pressure generates an electric charge, and vice versa
  - This allows ceramics to have medical applications, often as some kind of sensor (Chen-Glasser et al, 2018)
- Ceramics are hard to shape using traditional manufacturing
  - FDM doesn't work, as the melting point of ceramics is too high to be practical
- This makes stereolithography the best option

Method Planning

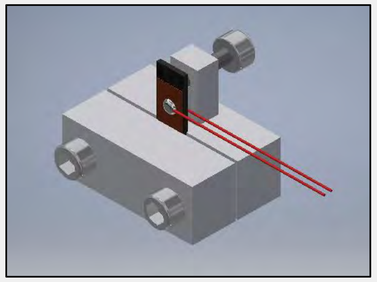

Using Autodesk Inventor, I 3D modeled a plan for the testing setup. The top screw puts a constant pressure on the sample, which is measured by an oscilloscope connected to the wires. Oscilloscopes measure the change in electrical signals. The bottom screws act as a clamp, so the setup can be used for any thickness sample.

Research Question

- What is the effect of adding a zinc oxide dopant to a barium titanate sample?
  - Is there a significant difference in their electromagnetic/ dielectric properties?
  - Is there an effect on the piezoelectric properties?

Method Application

UV Light Curing

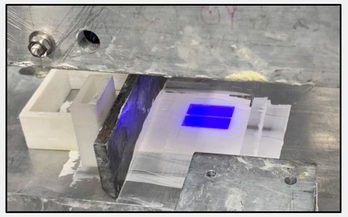

Pure BTO Sample

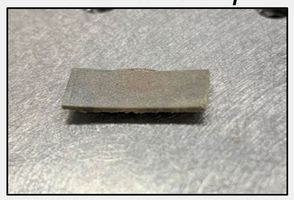

Copper Tape

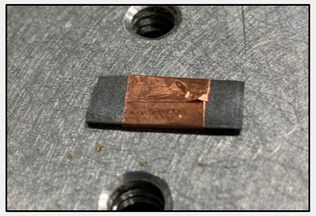

Connection to Oscilloscope

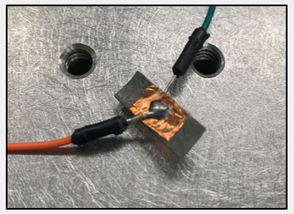

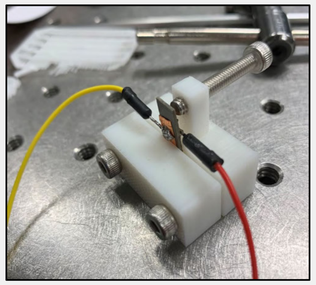

Prototype Pressure Application Setup

Results (pt. 1)

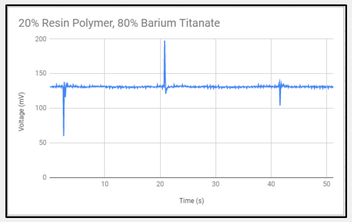

BTO Without ZnO

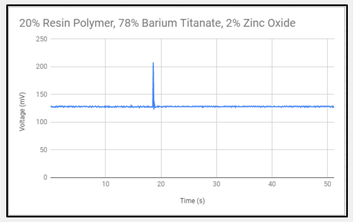

BTO With ZnO

Acknowledgements

I greatly appreciate the guidance and support of Dr. Song and his research group, including Li He. I thank the Belin- Blank Center, the National Science Foundation, and the SSTP program. Also, thank you to our Residential Assistants and our seminar leaders.

Results (pt. 2)

Sample	L: Inductance [H]	C: Capacitance [pF]	D: Dissipation factor	|Z| : Value of impedance [MW]
#1 (78+2) Mid	-747	33.90	0.0647	4.67
#2 (80) Mid	-941	26.90	0.0511	5.88
#1 (78+2) Edge	-743	34.00	0.0669	4.66
#2 (80) Edge	-932	27.10	0.0512	5.85

Sample	d33 [pC/N]	e33** [e-12 F/m]	g33*** [Vm-1Pa-1]
#1 (78+2) Mid	55	290.13	0.19
#2 (80) Mid	50	280.76	0.18
#1 (78+2) Edge	55	290.99	0.29
#2 (80) Edge	50	282.85	0.28

Conclusion

- The dielectric properties stayed consistent all the way through our samples
- Overall, the different samples gave very similar results
- Adding a ZnO dopant should allow more customization of the sensor material
  - For example, by adding ZnO, we should be able to add density to the sample with minimal sensitivity loss
- In this case, the density stayed the same, while the sensitivity did have a drop
  - Adding 2% of the dopant did not have a significant enough effect
- Another possible reason for the minimal change could be the method of dispersal
  - In our trials, the ZnO was completely mixed into the BTO
  - In other trials, it is mixed in as a gradient through the piece
- In future trials, we should try different dispersal methods to see if we can achieve a greater difference

References

Chen-Glasser, M., Li, P., Ryu, J., & Hong, S. (2018). Piezoelectric materials for medical applications [Chapter 7]. In *Piezoelectricity - organic and inorganic materials and applications* (pp. 125-137). https://doi.org/10.5772/intechopen.76963

Chen, Z., Qian, X., Song, X., Jiang, Q., Huang, R., Yang, Y., . . . Zhou, Q. (2019, February 28). Three-dimensional printed piezoelectric array for improving acoustic field and spatial resolution in medical ultrasonic imaging. Retrieved July 2, 2019, from https://www.ncbi.nlm.nih.gov/pmc/articles/PMC6471007/

Opto-Acoustic Device for Real-Time On-Site Flood Warning Using Smartphones

Anika Fuloria & Dr. Marian Muste

Introduction

Flooding is a prevalent problem throughout the world, causing destruction of infrastructure and loss of life. In fact, flooding results in more deaths than other natural disasters including tornadoes, hurricanes, and lightning [4]. A main cause of death in relation to flooding is vehicle accidents that occur because roads can be covered with deep, fast-moving water [5]. Another cause of death is being inside homes and other buildings when a flood occurs [2].

Leading Flood-Related Hazards for People: Water Depth & Water Velocity

Objective

Our project aims to reduce the number of deaths from flooding by providing individuals with alerts when a flood is occurring. The project will focus on helping people inside vehicles and buildings.

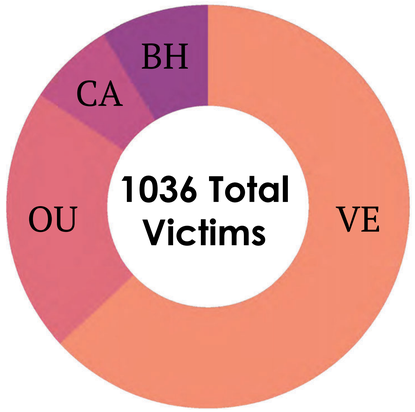

Percentage of Flash Flood Victims Based on Activity [2]

Vehicle (VE) – 654, Outside/Close to Streams (OU) – 220, Campsite/Recreational Area (CA) – 72, Permanent Building & Mobile Home (BH) – 90

Depth Sensing *(via Ultrasonic Sensor)*:

To find the water depth, we used an Arduino and an ultrasonic sensor (HC-SR04). The circuitry is shown below.

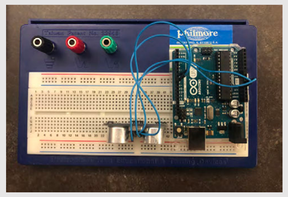

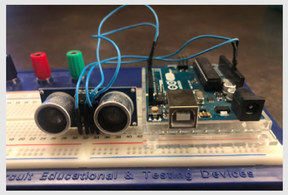

The ultrasonic sensor returns two distances in centimeters: the water depth and the height difference between the sensor and the water. These two measurements taken are shown below.

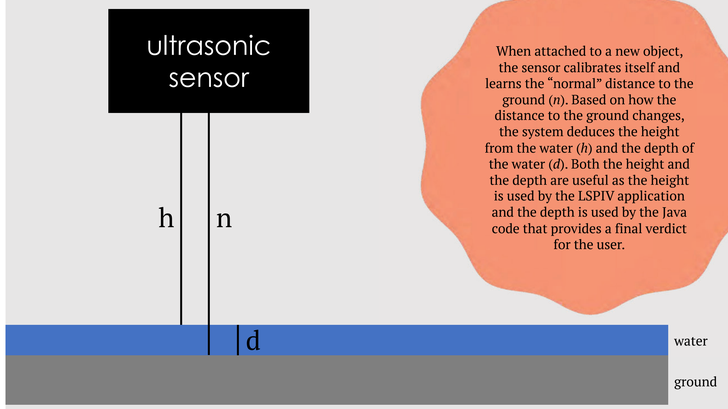

When attached to a new object, the sensor calibrates itself and learns the "normal" distance to the ground (*n*). Based on how the distance to the ground changes, the system deduces the height from the water (*h*) and the depth of the water (*d*). Both the height and the depth are useful as the height is used by the LSPIV application and the depth is used by the Java code that provides a final verdict for the user.

Velocity Sensing *(via LSPIV)*:

To find the water surface velocity, we used a smartphone application based on Large-Scale Particle Image Velocimetry (LSPIV). LSPIV tracks particles on the surface of the water and finds their velocity. Using the height above the water, the app is able to scale the velocity from LSPIV into meters per second [3].

LSPIV works by tracing particles on the surface of water [1]. In the picture on the right, the gray dots are the particles on the first frame and the black dots are particles on the second frame. The arrows between them represent the direction of the individual velocity vectors. A final velocity can be calculated by averaging all of the individual velocities.

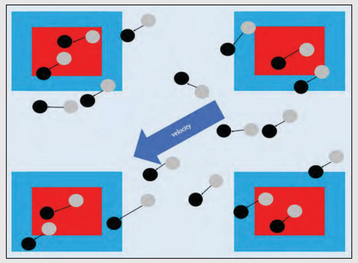

Screenshot of LSPIV Application

Warning Device Protocol

- Ultrasonic device provides accurate water height and depth
- LSPIV finds the surface velocity of the water
- Data (depth and velocity) are synthesized and a final warning is presented based on the actual situation

Protocol Testing

The picture on the right shows the setup that was used to collect the data. The red dot is where the smartphone (iPhone) was.

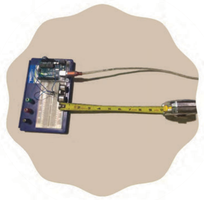

The ultrasonic device was tested for accuracy. The device performed with an error of ± 1.6%.

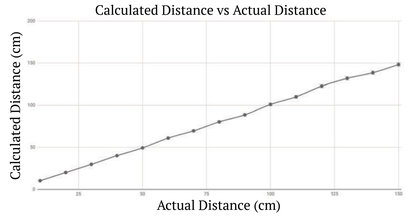

The LSPIV app was tested with a variety of camera heights and water velocities. The uncertainty for the tested conditions ranged from ± 6.5% to ± 8.7%.

Future Research

- Integration of the ultrasonic sensor with the smartphone
- Improvement of the LSPIV application:
  - Reliable scaling of velocity vectors based on height
  - Faster speed of imaging
  - Moving interrogation windows
- Communication between the application and the ultrasonic sensor

Acknowledgements:

I would like to thank Dr. Marian Muste for his guidance on this project. Additionally, I would like to thank IIHR, Ryota Tsubaki, and the team at the Model Annex.

References:

[1] Bodart, G. (n.d.). *Facing adverse conditions of image-based hydrometry (LSPIV)*, 1-43.
[2] Terti, G., Ruin, I., Anquetin, S., & Gourley, J. J. (2017). A Situation-Based Analysis of Flash Flood Fatalities in the United States. *Bulletin of the American Meteorological Society*, *98*(2), 333-345. https://doi.org/10.1175/BAMS-D-15-00276.1
[3] Tsubaki, R., Fujita, I., Yu, K., & Muste, M. (2015). Large-Scale Particle Image Velocimetry (LSPIV) Implementation on Smartphone. In *E-proceedings of the 36th IAHR World Congress* (pp. 1-6).
[4] U.S. Department of Homeland Security. (2018, September). *Flood Apex Research Program – Findings and Progress, Science & Technology* (D. Alexander & D. Cotter, Authors). Retrieved from https://www.asfpmfoundation.org/ace-images/LALspeaker_series
[5] Xia, I., Falconer, R. A., Lin, B., & Tan, G. (2011). Numerical assessment of flood hazard risk to people and vehicles in flash floods. *Environmental Modelling & Software*, *26*(8), 987-998. https://doi.org/10.1016/j.envsoft.2011.02.017

For more resources, scan the QR code below.

Scan me

Improving the selectivity of polydicyclopentadiene membranes by adding different activators

Benjamin Hong[1], Katherine Sulaitis[2], B.S., Ned Bowden[2], Ph.D.
[1] East Brunswick High School, [2] Department of Chemistry, University of Iowa

Introduction

EPA-EE (Eicosapentaenoic acid ethyl ester) and DHA-EE (docosahexaenoic acid ethyl ester), two derivatives of fish oil, require expensive separation methods, such as distillation or chromatography. Membranes offer an alternative solution that is significantly more cost effective. The purpose of this project is to create a membrane composed of polydicyclopentadiene (PDCPD) capable of separating fatty acids with high flux ratios between desirable and non-desirable molecules.

Methods

Dicyclopentadiene (DCPD) has a highly reactive alkene group, that allows it to engage in ring-opening metathesis polymerization.

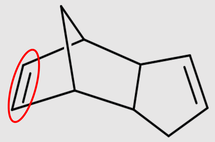

dicyclopentadiene

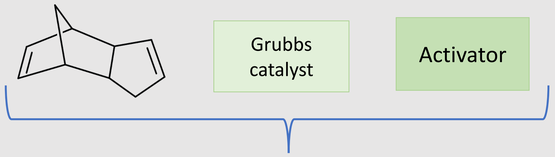

2 Hours @ 50°C

PDCPD membranes

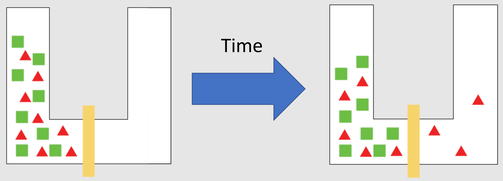

Results

The membrane acts similarly to a coffee filter, where larger particles are unable to pass through but smaller particles can.

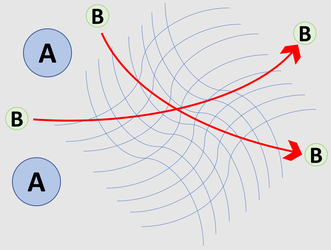

The selectivity of the membranes was tested by adding *p*-nitrobenzaldehyde and triphenylmethane and finding their flux ratios. Since triphenylmethane is a larger molecule, less of it should permeate through.

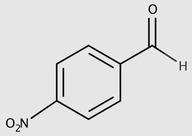

p-nitrobenzaldehyde

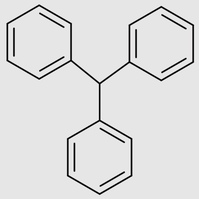

triphenylmethane

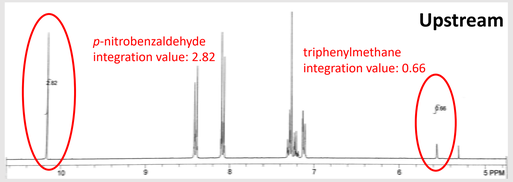

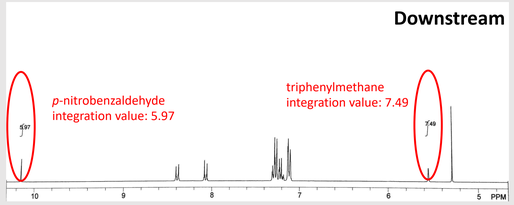

Integrations for the membrane made with Grubbs 1 and tetrachlorocyclopropene in a 1:1 ratio

We found that using tetrachlorocyclopropene gave us the best *p*-nitrobenzaldehyde to triphenylmethane flux ratio of about 5.4:1 when used in a 1:1 ratio with the Grubbs first generation catalyst. This is an improvement from the other membranes, which typically had flux ratios of only about 3:1.

tetrachlorocyclopropene

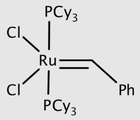

Grubbs 1st generation catalyst

Overall, the Grubbs first generation catalyst performed much better than the second generation catalyst. The second generation catalyst membranes were significantly thinner and possessed many traits that were not ideal for separations.

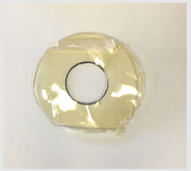

Grubbs 1 membrane

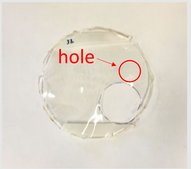

Grubbs 2 membrane

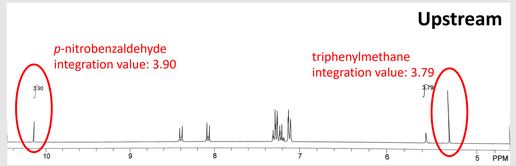

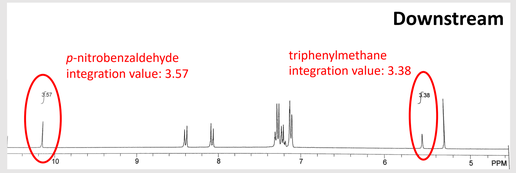

Integrations for the membrane made with Grubbs 2 and tetrachlorocyclopropene in a 1:1 ratio. The flux ratio here is 1.0:1, which is significantly poorer than its Grubbs 1 counterpart.

Implications

The membranes studied in this study are unique in their ability to separate molecules by cross-sectional area rather than molecular weight. This provides an alternative way of separating fatty acids, which has depended on the same methods for decades. In order to ensure that the membranes work optimally for EPA-EE and DHA-EE, it is important that in the future the membranes are tested for their selectivity with these molecules. Also, the permeation rate could be improved by applying pressure or changing temperature, this could provide a new industrial method of separating fatty acids that is less expensive and equally, if not more, effective than current methods of separation. Hopefully, this will create a successful method of separating fatty acids that is both efficient and inexpensive.

References

- Gilmer, C. M., & Bowden, N. B. (2016). Highly cross-linked epoxy nanofiltration membranes for the separation of organic chemicals and fish oil ethyl esters. *Acs Applied Materials and Interfaces*, 24104-24111. doi:10.1021/acsami.6b07749
- Gupta A, Bowden NB. Separation of cis-fatty acids from saturated and trans-fatty acids by nanoporous polydicyclopentadiene membranes. *Acs Applied Materials & Interfaces*. 5: 924-33. PMID 23281782 DOI: 10.1021/am3025867
- Long, T. R., Elder, R. M., Bain, E. D., Masser, K. A., Sirk, T. W., Jian, H. Y., ... & Lenhart, J. L. (2018). Influence of molecular weight between crosslinks on the mechanical properties of polymers formed via ring-opening metathesis. *Soft matter*, 14(17), 3344- 3360.
- Long TR, Gupta A, Miller AL, Rethwisch DG, Bowden NB. Selective flux of organic liquids and solids using nanoporous membranes of polydicyclopentadiene. *Journal of Materials Chemistry*. 21: 14265-14276. DOI: 10.1039/c1jm10970g
- Swanson, D., Block, R., & Mousa, S. A. (2012). Omega-3 fatty acids EPA and DHA: Health benefits throughout life. *Advances in Nutrition,3*(1), 1-7. doi:10.3945/an.111.000893

Acknowledgments

I would like to thank Professor Ned Bowden and Katherine Sulaitis, the graduate student I worked with, for spending the time to guide me for this research project. I wish them and the rest of the Bowden research group the best of luck in their future endeavors. I would also like to thank the Belin-Blank center for providing me with the resources and opportunity for this project.

Sequence Variations in the GDF11 Gene in the African Population with Orofacial Clefts

Siyong Huang[1], Valeria Bravo[1], Tamara Busch[1], Joy Olotu[1], Mary Li[1], John Pape[1], Mohaned Hassan[1], Chinyere Adeleke[1], Waheed Awotoye[1], Azeez Butali[1]
[1]Department of Oral Pathology, Radiology, and Medicine, University of Iowa

Intro

Figure 1: These are the common forms of orofacial clefts: Cleft Palate (left) and both Cleft Lip and Palate (right)
Photo Credit: Apollo Hospital

- Orofacial Clefts affect ≈ 1 in 700 births
  - Increase infant mortality
  - Significant morbidity in adulthood
- There are three main types
  - CLP – Cleft Lip and Palate
  - CL – Cleft Lip
  - CPO – Cleft Palate Only
- OFCs are complex diseases
  - Caused by combination of many genes as well as
  - Environmental factors such as alcohol and smoking
- Growth Differentiation Factor 11 (GDF11)
  - Important protein-coding gene
  - Affects development of organ systems
  - Regulates aging
- GDF11 gene was recently found to be related to orofacial clefts[1]
- This study analyzed variations of GDF11 in the African population with OFCs
  - Samples from Ethiopia, Ghana, and Nigeria
  - Samples are organized by CLP, CL, and CPO
  - Total of 768 samples in plates of 96

Methods

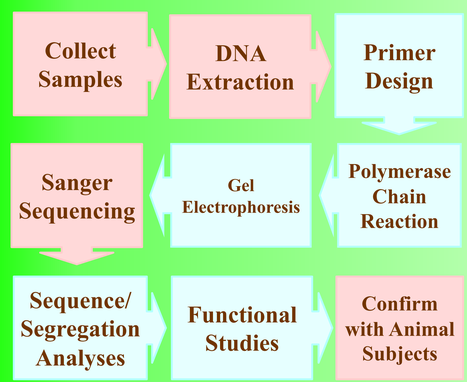

Objective: Find Genetic Cause of Orofacial Clefts

Results

Wild Type / Mutant

Figure 2: Electropherogram of wild type (left) and mutant (right) variations. Wild type is the common genotype found in the majority of people, while the mutant variation is rare and probably more dangerous. These variants are located on the third exon of the GDF11 gene.

Novel variation found at position 55749667 on chromosome 12. Although SIFT predicted it to be tolerated and PolyPhen anticipates benign, its CADD score was 23.7, which ranks it among the top 1% of deleterious variants.

Lysine → Glutamic acid

Figure 3: Image of the mutation: The Lysine is mutated into Glutamic acid

HOPE Summary

- Charge of AA swaps from positive to negative
  - Heavily disturbs protein interaction and formation
- This particular AA is likely in contact with other proteins
  - Vastly changes protein interaction
- Glutamic acid is slightly smaller than Lysine

Wild Type / Variant

Figure 4: Electropherogram of wild type (left) and mutant (right) variations. Wild type is the common genotype found in the majority of people, while the mutant variation is rare and probably more dangerous. These variants are located on the second exon of the GDF11 gene.

Rare, known variation (rs780604190) [MAF=3.985e-6] found at position 55748780 on chromosome 12. This variant was also classified as tolerated and benign for SIFT and PolyPhen, but its CADD score was 22.4, which means it is predicted to be among the top 1% of deleterious variants.

Glycine → Arginine

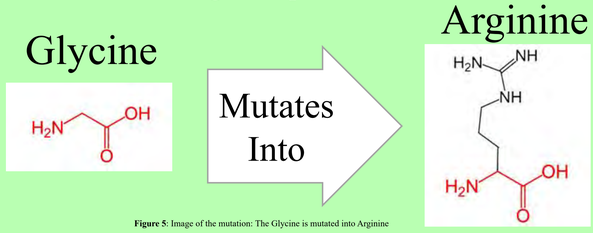

Figure 5: Image of the mutation: The Glycine is mutated into Arginine

HOPE Summary

- Glycine neutral, Arginine is positive
  - Heavily disturbs protein interaction and formation
- AA becomes more hydrophobic
  - Further impacts protein interaction and formation
- Arginine is much larger and inflexible than Glycine
  - Impact protein structure

Location	Codon Change	Amino Acid Change	PolyPhen	SIFT	Provean	CADD
chr12: 55749667	K(AAG)> E(GAG)	Lys 337 Glu	Benign	Tolerated	Neutral	**23.7** (top 1%)
chr12: 55748780	G(GGA)> R(AGA)	Gly 214 Arg	Benign	Tolerated	Neutral	22.4 (top 1%)

Conclusion

This study found two variants that could affect the protein's function, and both are predicted to be among the top 1% of deleterious mutations. Both variants demonstrated a change in charge, which would impact protein interaction. There is a good chance that these mutations contributed to the formation of OFCs in the patients.

Future Work

- Troubleshoot and redesign primer for exon 1 of this gene
- Test predictions on Zebrafish embryo to determine whether this variation actually has a severe effect

Figure 6: Image of zebrafish embryo

- Determine if the variants are functional using migration assays in keratinocytes and mesenchymal cells

Acknowledgements: I would like to thank the Butali Lab for allowing me to conduct research. I appreciate Dr. Azeez Butali for his support and for allowing me to work in his lab. Tamara Busch and my lab group were also crucial to help me learn how to properly conduct research. I would also like to thank the Belin-Blank Center for hosting the SSTP program. Finally, for the samples used in this study, I thank the families in Ghana, Ethiopia, and Nigeria. This work was supported by **NIDCR K99/R00 Grant DE022378 and Robert Wood Johnson Foundation Grant number 72429 (AB)**.

Citations:
[1] Cox, T., Lidral, A., McCoy, J., Cox, L., Zhu, Y., Anderson, R., … Roscioli, T. (2019). Mutations in GDF11 and the extracellular antagonist, Follistatin, as a likely cause of Mendelian forms of orofacial clefting in humans. *Human Mutation, 0*(0); 1– 13. doi: 10.1002/humu.23793

Testing the role of the mitochondrial calcium uniporter in pain, learning and anxiety behavior in mice

Yuting Huang, Leonid Shutov, Jake Rysted, Maria Pattschull, Yuriy Usachev

Introduction/Background:

Synaptic plasticity is the ability for synaptic connections to become stronger or weaker based on one's experience. Long-term exposure to a certain stimulus makes neurons easily excitable to generate a response. Synaptic plasticity is involved in almost all neuronal activities such as anxiety behaviors, memory formation, pain processing and neurological diseases like epelipsy.

The mitochondrial calcium uniporter (MCU) is a calcium channel on the inner membrane of mitochondria. Calcium controls the release of neurotransmitters. By elongating the time of high cytoplasmic calcium level, MCU enhances synaptic connections. Therefore, MCU can be a potential therapeutic target to treat neurological diseases by modulating synaptic plasticity. The effects of MCU on synaptic plasticity of neurons that process different types of information need to be determined before the application of medicine that targets MCU.

Methods:

By comparing the differences between MCU knockout and wild type mice in different behavioral tests, the effects of MCU on different brain functions can be discovered.

1. Elevated plus maze was used to test the effect of MCU on anxiety behaviors. Mice were given two choices: open arms where they should feel unsafe from light, height and potential predators; closed arms where they should feel protected in the dark and enclosed environment. The more a mouse explores the open arms, the less stressful it is.

2. In the novel object recognition test, mice were habituated to the arena, familiarized with two objects and allowed to explore one of the familiar objects and a novel object. The more a mouse explore the novel object, the stronger its recognitive memory is. In cued fear conditioning test, mice were first trained to associate foot shocks (a fearful stimulus) with a tone in a certain context. Their time being motionless were used to determine if they memorized fearful experience by the context or the sound cue.

3. CFA was injected into the hind paws of mice to induce inflammation. The pain responses (paw withdrawal, licking or shaking) to mechanical and thermal stimuli were measured through von Frey and Hargreaves tests respectively. The more sensitive they are, the more severe pain response they develop.

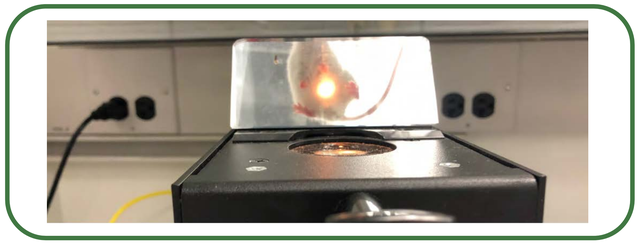

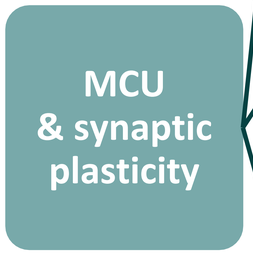

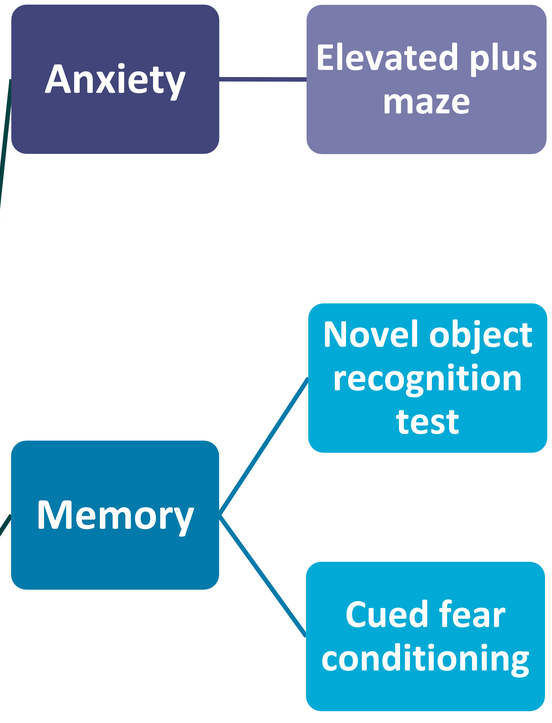

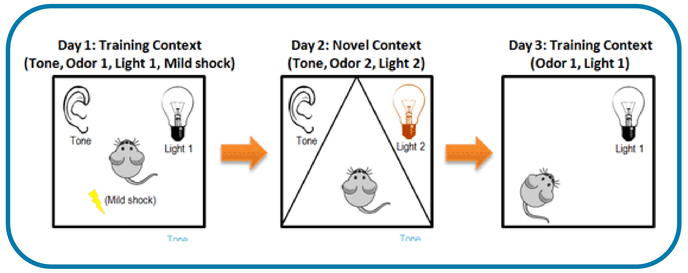

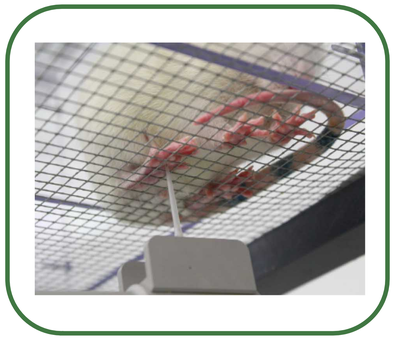

Elevated plus maze results:

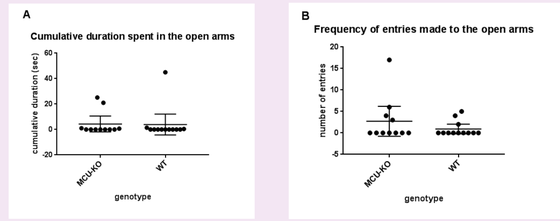

Figure 1: A. Cumulative durations mice spent in the open arms. B. Frequencies of entries mice made to the open arms. These two graphs show that MCU-KO mice had similar anxiety -related behavior to WT mice.

Novel object recognition test results:

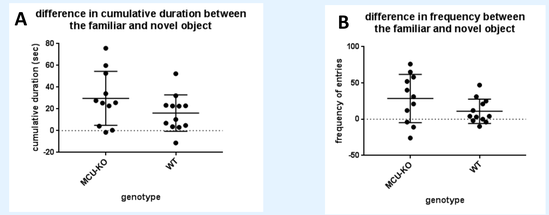

Figure 2: A. Differences in cumulative duration mice spent around the familiar and novel objects. B. Differences in frequency of mice's exploration around the familiar and novel objects. The graphs show that MCU-KO mice were not significantly better in recognitive memory than WT mice.

CFA-induced inflammatory pain test results:

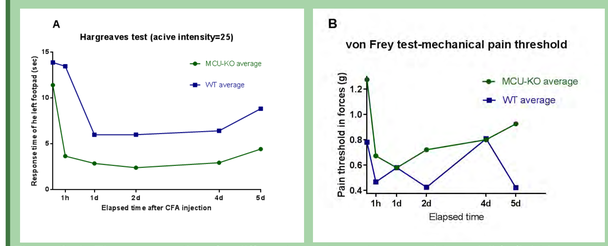

Figure 3: A. The average time for different genotypes to respond to a visible light beam (active intensity=25) after injections. B. The average nociceptive thresholds to a mechanical stimulus. MCU-KO resembled WT in developing inflammatory pain.

Conclusions:

MCU deletion did not cause a statistically significant effect on the anxiety-related behavior, memory or inflammatory pain reception of mice (p-values>0.05). However, MCU-KO tended to do better in recognizing novel objects, but become more hypersensitive to thermal stimuli in the presence of inflammation. These findings were underpowered and need further validation. Hypersensivity to heat should be addresses when applying medicine that targets MCU.

References:

Fehrenbacher, J. C., Vasko, M. R., & Duarte, D. B. (2012). Models of inflammation: Carrageenan- or Complete Freund's Adjuvant-induced edema and hypersensitivity in the rat. *Current Protocol Pharmacology*. https://doi.org/10.1002/0471141755.ph0504s56

Kim, H. Y., Lee, K. Y., Lu, Y., Wang, J., Cui, L., Kim, S. J., . . . Chung, K. (2011). Mitochondrial Ca2+ uptake is essential for synaptic plasticity in pain. *Journal of Neuroscience*, *31*(36), 12982-12991. https://doi.org/10.1523/JNEUROSCI.3093-11.2011

Leger, M., Quiedeville, A., Bouet, V., Haelewyn, B., Boulouard, M., Schumann-Bard, P., & Freret, T. (2013). Object recognition test in mice. *Nature Protocols*, *8*, 2531-2537. https://doi.org/10.1038/nprot.2013.155

Walf, A. A., & Frye, C. A. (2007). The use of the elevated plus maze as an assay of anxiety-related behavior in rodents. *Nature Protocols*, *2*(2), 322-328. https://doi.org/10.1038/nprot.2007.44

UTILIZATION OF METABOLIC SCREENING CARDS FOR GENE EXPRESSION ANALYSIS IN AUTISM SPECTRUM DISORDER

Haley Humes[1], Taylor Thomas[2], Jacob Michaelson[2]
Pleasant Valley High School[1], University of Iowa[2]

INTRODUCTION

Autism Spectrum Disorder (ASD)

- neurodevelopmental disorder
- challenges with social skills, behavior, and communication
- affects 1 in 59 children in the US (Fombonne, 2018)

Figure 1: Genetic Causes of ASD

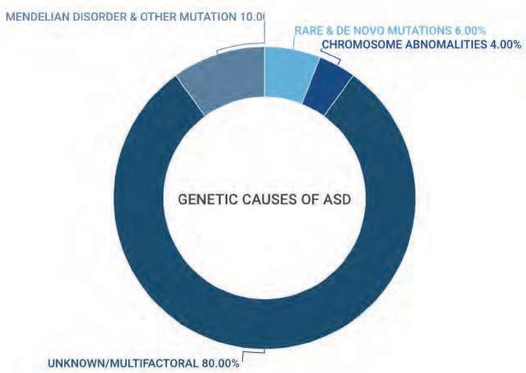

The underlying biological mechanisms and etiology are still unknown.

There is a need for a more accessible test to analyze gene expression in ASD. Gene expression data is usually lacking in sample size, limiting the power of the study (Abrahams & Geschwind, 2008). Metabolic screening cards could make gene expression analysis more accessible. Data can be collected from more individuals and provide a better sample of genetic issues in ASD.

Metabolic Screening Cards

- typically used during newborn screening to detect metabolic disorders
- simple finger prick
- benefits
  - more convenient way to collect a sample (no need for a phlebotomist)
  - provides a broad range of data (Karlsson, Guthenberg, von Döbeln, Kristenssson, 2003).

Figure 2: Newborn Screening Testin Using Metabolic Screening Cards

Retrieved From: www2.health.vic.gov.au

RESEARCH OBJECTIVE

Goal: to determine if the metabolic screening cards can be used for storing RNA and measuring gene expression

METHODS

Figure 3: Extraction & RT-qPCR Process

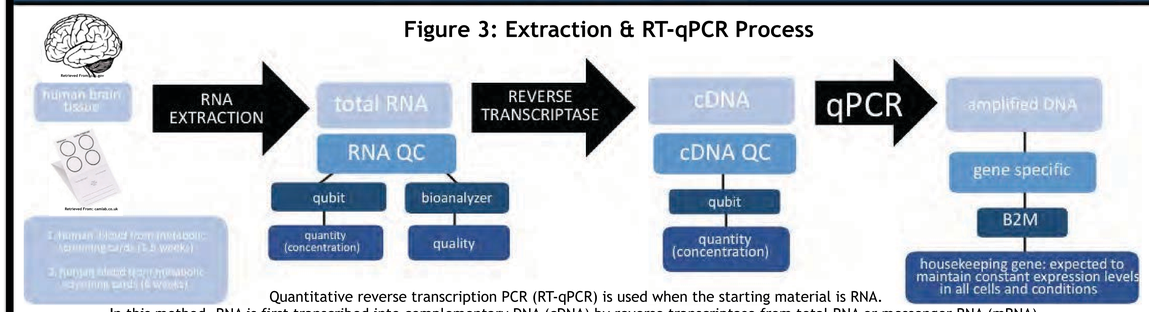

Quantitative reverse transcription PCR (RT-qPCR) is used when the starting material is RNA.
In this method, RNA is first transcribed into complementary DNA (cDNA) by reverse transcriptase from total RNA or messenger RNA (mRNA).
The cDNA is then used as the template for the qPCR reaction to detect, characterize and quantify nucleic acids for numerous applications.

RESULTS

Figure 4: RNA Bioanalyzer Results (Human Brain Tissue)

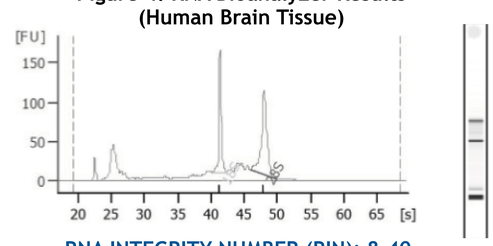

RNA INTEGRITY NUMBER (RIN): 8.40

Table 1: RNA Qubit Results

Sample Type	*Concentration (ng/ul)*
Human Brain Tissue	*24*
Human Blood From Metabolic Screening Cards (#1)	3.27
Human Blood From Metabolic Screening Cards (#2)	7.89

Figure 5: RNA Bioanalyzer Results (Human Blood From Metabolic Screening Card #1)

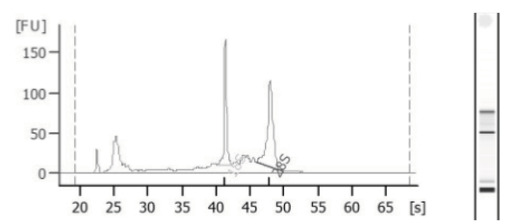

RNA INTEGRITY NUMBER (RIN): 3.00

Figure 6: RNA Bioanalyzer Results (Human Blood From Metabolic Screening Cards #2)

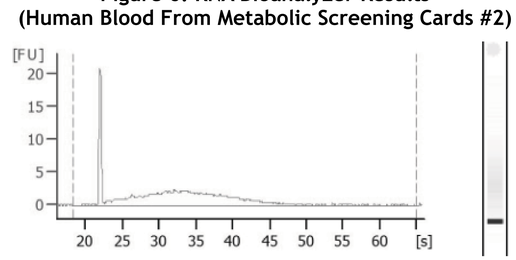

RNA INTEGRITY NUMBER (RIN): 2.10

Figure 7: Reverse-Transcribed cDNA by Traditional PCR

```
CCTTTCAGTTTAAAGGACTTAACGATACACAGACCCAAAGTAGGTAGGCTGTAACTTCAACTGAATGAC
                    >>>forward>>> 264 to 286
GACTTGTCTTTCAGCAAGGACTGGTCTTTCTATCTCTTGTACTACACTGAATTCACCCCCACTGAAAAA
    250       260       270       280       290       300       310
CTGAACAGAAAGTCGTTCCTGACCAGAAAGATAGAGAACATGATGTGACTTAAGTGGGGGTGACTTTTT
                                <<<reverse<<< 387 to 406
TCACAGCCCAAGATAGTTAAGTGGGATCGAGACATGTAAGCAGCATCATGGAGGTTTGAAGATGCCGCA
```

(Complementary DNA (cDNA) is made by reverse transcribing the RNA templates with the enzyme reverse transcriptase.)

Figure 8: Gel Electrophoresis of B2M Gene by Traditional PCR

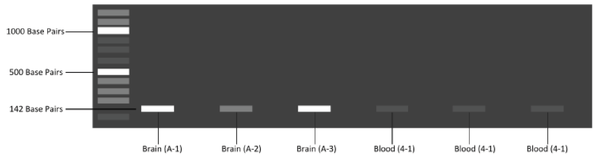

(The presence of B2M was detected in all samples.)

CONCLUSION

- Total RNA was successfully extracted from the metabolic cards, however it is low quality.
- cDNA can be successfully reverse transcribed from RNA from metabolic cards
- The presence of B2M was detected from the reverse-transcribed cDNA by traditional PCR.

FUTURE DIRECTIONS

- Develop an RT-qPCR protocol to qualitatively detect the amount of the gene of interest (as opposed to the traditional PCR, which just detects presence/absence)
- Use this method for genes implicated in autism to analyze gene expression

REFERENCES

Abrahams, B., & Geschwind, D. (2008). Advances in autism genetics: on the threshold of a new neurobiology. *Nature reviews genetics*, *9*(5), 341.

Fombonne, E. (2018). Editorial: The rising prevalence of autism. *Journal of Child Psychology and Psychiatry*, *59*(7), 717-720.

Karlsson, H., Guthenberg, C., von Döbeln, U., & Kristenssson, K. (2003). Extraction of RNA from dried blood on filter papers after long-term storage. *Clinical chemistry*, *49*(6), 979-981.

ACKNOWLEDGEMENTS

Thank you to Dr, Jacob Michaelson, Taylor Thomas, the Michaelson Lab, the Belin-Blank Center, and SSTP for their help and this opportunity.!

Characterizing a mutation of the mitochondrial membrane protein AKAP1 in intellectual disability

He Jiang[1], Yujia Liu[2], Ronald A. Merrill[2], Stefan Strack[2]

[1]*Princeton Intl. School of Math and Science, Princeton, NJ*

[2]*Department of Pharmacology, University of Iowa Carver College of Medicine, Iowa City, IA*

University of Iowa Carver College of Medicine

Belin-Blank Center
College of Education
The University of Iowa

Abstract

Mitochondrial dynamics is driven by a protein named Drp1. An anchoring protein on mitochondrial outer membrane called AKAP1 regulates this process by interacting with Drp1's two enzymes, PKA and CaN. Their interactions are shown to influence neural development in mice.

In this study, we try to characterize how AKAP1 mutations might affect human neural development. We focused on how one AKAP1 mutation identified in a 3-year-old patient contributes to intellectual disability. Specifically, we approach this goal by refining a two-step purification process to obtain the desired AKAP1 proteins. We construct plasmids to produce AKAP1 with GST-tag and his-tag fused at each end. Rosetta cells are transformed with plasmids to produce protein and then lysed. Cell lysis is first purified using nickel column, which binds to AKAP1 with his-tag. Protein concentration is normalized before proceeding with the second purification using GST-glutathione beads. These beads recognize AKAP1 with GST-tag. Thus, we can select the proteins with both tags, which are therefore intact. We later perform brain lysate pull down on those proteins, which shows weak signals and sign of AKAP1 degradation. This can be improved using new constructs of plasmids or stronger inhibition.

Our project provides foundation to investigate the effect of AKAP1 mutations in intellectual disability.

Backgrounds

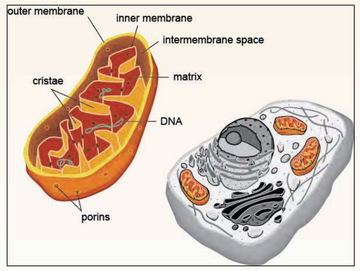

Fig 1. "The Powerhouses"—Mitochondria in mammalian cell. **Mitochondria** are known as the "powerhouses" of cells because of it ATP production. However, it is also responsible for other functions such as maintaining calcium homeostasis and promoting cell cycle progression. Image is not drawn to scale.
(Image credit: Pearson Education, 2009)
Image is not drawn to scale.

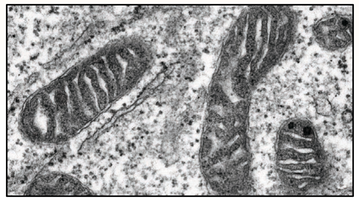

Fig 2. Electron microscopy image of mitochondria.
Mitochondria dynamics refer to the constant equilibrium of fission and fusion. Dephosphorylation of Dynamin related protein (Drp1) drives this process.
(Image credit: www.cera.org.au)

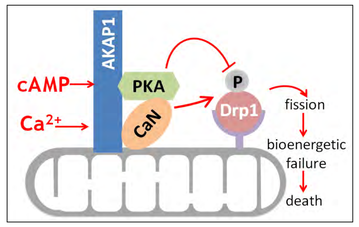

Fig 3. AKAP1::PKA::CaN regulates the function of Drp1.
AKAP1 (A-Kinase Anchoring Protein 1) is an anchoring protein located on the mitochondrial outer membrane. It binds to two enzymes, CaN that activates and PKA that inactivates Drp1, which is a protein that causes mitochondrial fission.

Objective

A 3 years-old female patient in Spain was found to carry compound **heterozygous AKAP1 mutations.**

Patient clinical features:

- **Intellectual disability**
- **Autism**

Experimental Approaches:

AKAP1 subcellular localization (V33G) √

Mitochondrial morphology √

AKAP1 protein turnover √

AKAP1::CaN interaction

Posición cromosómica/ Genotipo	Gen*(MIM#)/ Transcrito	Cambio Nucleotídico/ Proteico	Exón/ Efecto	Cigosidad (VAF)/ Profundidad			ID dbSNP/ Frec. ExAC
				Prob.	P	M	
chr17:55182923 T/G	*AKAP1 (MIM#602449)* NM_001242902.1	c.98T>G p.(Val33Gly)	Exón 3 *missense*	Het (51%) 198X	- 82X	Het (41%) 163X	rs147774257 0.061%
chr17:55183196 G/A	*AKAP1 (MIM#602449)* NM_001242902.1	c.371G>A p.(Arg124His)	Exón 3 *missense*	Het (49%) 231X	Het (48%) 217X	- 165X	rs150162032 0.002%

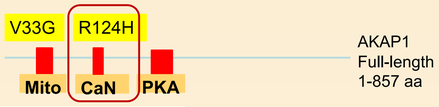

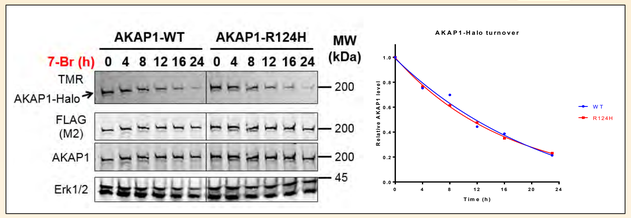

Fig 5. The R124H mutation has no affect on AKAP1 protein turnover.
AKAP1 WT and R124H mutant with HaloTag were transfected into COS1 cells. The amount of protein was labeled by TMR over the course of 24 hours. The amount of protein at given time points were quantified as shown.

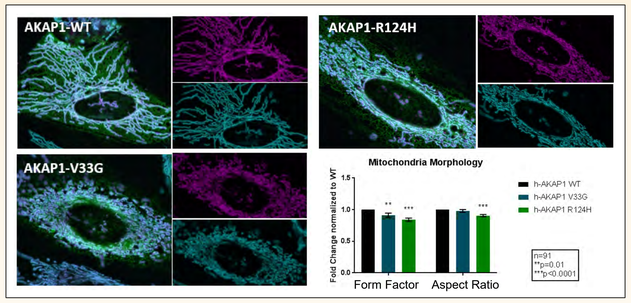

Fig 6. Both V33G and R124H mutations promote mitochondrial fission.
HeLa cells were transfected with AKAP1-WT control, AKAP1-V33G and –R124H variants in glass bottom chamber slides before proceeded to immunofluorescent staining for mitochondria (cyan), AKAP1 (purple) and ER (green). Images were analyzed by ImageJ. Data presented by form factor and aspect ratio. ($p<0.05$)

Methods

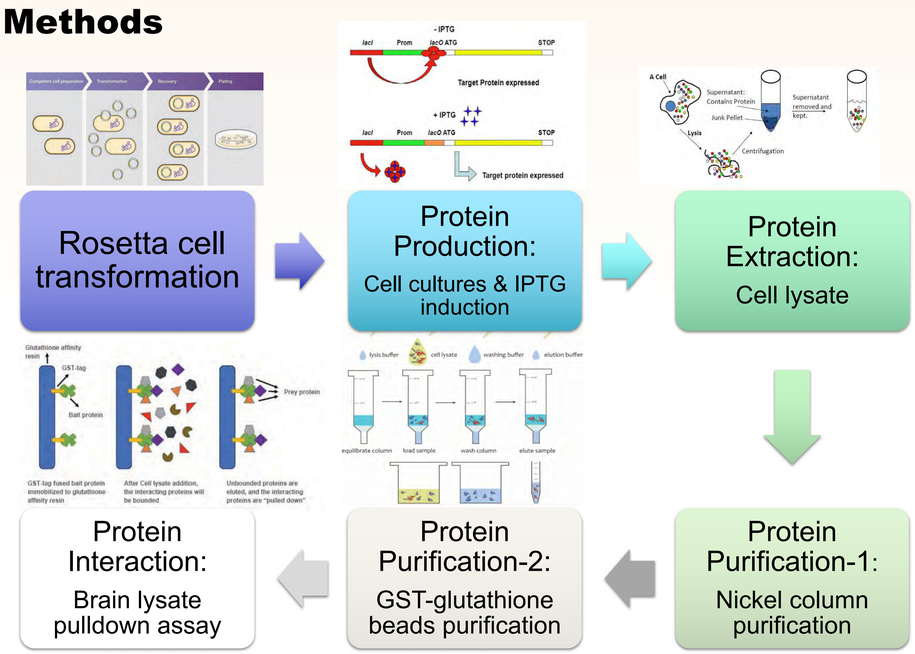

Results

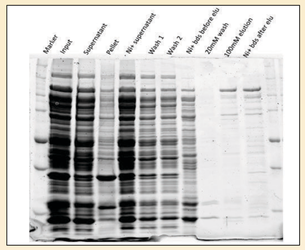

Fig 7. A typical Coomassie stain image of nickel column purification results (R124H)
Before the purification, our proteins should exist in the supernatant after lysis because of its solubility. We can see during the purification, most uninvolved proteins are washed off. In the 100mM final elution, we can perceive the existence of our desired protein (AKAP1), though some still remains on the nickel beads(last two lanes). This suggest a higher concentration of imidazole can be use to elute in the future.

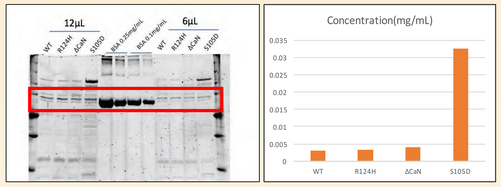

Fig 8. Protein elutions compared with BSA standards.
The signal intensity of the standards and elutions from Coomassie stains (left) are compared using ImageJ. Then the protein concentrations are calculated (right). Elutions are diluted to same concentration before proceeding with the next purification.

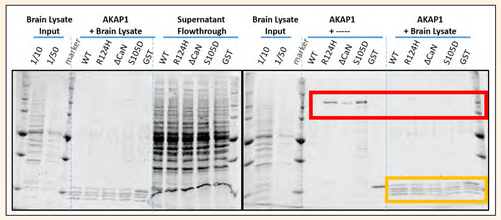

Fig 9. Fast-green staining of GST-glutathione purification and brain lysate pull down results
We can see the existence of AKAP1 on beads, proving a successful purification despite the unevenness in their amount. From the pull down, most protein in brain lysate end up in the flowthrough, while the binding is weak.

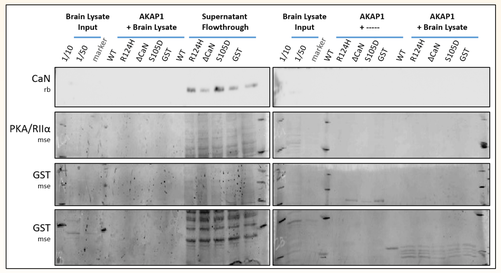

Fig 10. Western blotting of brain lysate pull down results, probing for GST and ΔCaN.
We can see the existence of various protein in the flowthrough, but not much in the actual pull down. We detect ΔCaN in the flowthrough, but not in brain lysates or pull down. Since bands appear, the antibodies should be functional, while degradation or low protein concentration might account for no bands.

Conclusion & Future Direction

- For this specific project, we have finalized the two-step purification process to obtain desired AKAP1 protein. To boost the signal strength, we can use higher cell density for purification in the future and add more inhibitors to prevent protease from degrading the proteins. Changing the vector used for transformation might enhance the protein production.
- This project provides foundation to investigate the differences in CaN binding between WT and R124H AKAP1.

Acknowledgement

Secondary Student Training Program
Stefan Strack Laboratory
Dr. Alberto Fernández Jaén M.D.

Hospital Universitario quirónsalud Madrid

American Heart Association.

NIH National Institutes of Health

References

Cribbs, J. T., & Strack, S. (2007). Reversible phosphorylation of Drp1 by cyclic AMP-dependent protein kinase and calcineurin regulates mitochondrial fission and cell death. *EMBO Reports*, *8*(10), 939–44. https://doi.org/10.1038/sj.embor.7401062

Dickey, A. S., & Strack, S. (2011). PKA/AKAP1 and PP2A/Bβ2 regulate neuronal morphogenesis via Drp1 phosphorylation and mitochondrial bioenergetics. The Journal of Neuroscience : The Official Journal of the Society for Neuroscience, 31(44), 15716–26. https://doi.org/10.1523/JNEUROSCI.3159-11.2011

The design and implementation of a low-cost solution for cluster computing with MATLAB on Docker Swarm

Kaibo Tang[1, 2], & Chris W. Schwarz[2]

[1]The Stony Brook School, Stony Brook, NY, [2]National Advanced Driving Simulator, University of Iowa, Iowa City, IA

kaibo-tang@uiowa.edu

Introduction

Table 1.
The advantages of cluster computing which can be utilized to boost the data reduction process at NADS.

Data Reduction at NADS	Cluster Computing
Multiple reduction tasks	Multi-core, multiple computers
Different sets of data are independent	Parallelization
Time-consuming	Significant reduction in time due to the distribution of tasks

Objectives

- The objective of this study is to design a low-cost solution for cluster computing with MATLAB.
- Hypothesis 1: Performance of the cluster will be positively correlated with:
  - Number of paralleled tasks on a single machine;
  - Total number of machines involved in the cluster.
- Hypothesis 2: Cluster > Parallel

Conclusion

This study manifests the feasibility and promising performance of simultaneously running multiple containerized MATLAB scripts in an on-premise computer cluster. The advantages of Docker compared to other solutions are listed in figure 2.

Table 2.
The advantages of Docker compared to three other solutions.

	Docker	Microsoft HPC Pack	MATLAB Parallel Server	pMATLAB
Cost	$0	$972/core[2]	License-required	$0
OS Requirement	/	Windows Server[3]	/	/
Coding Intensive?	No	N/A	N/A	Yes[4]
Performance[1]	High	N/A	N/A	Poor[4]

[1] Performance is compared to running on one machine.
[2] Windows Server 2019 Standard. Retrieved from https://www.microsoft.com/en-us/cloud-platform/windows-server-pricing
[3] Windows Server is only required for head nodes and worker nodes. OS requirement for workstation nodes is Windows 10 Pro, Education or Enterprise.
[4] According to Swatski (2014).

The study also paved the way for deploying ndaqTools onto all the idle machines at NADS which, embedded with a data access interface to the filer, will significantly increase the data reduction efficiency.

Acknowledgment

I would like to express my special thanks to Dr. Schwarz and Dr. Brown for having me at NADS and for the opportunity to put my crazy idea of creating an HPC cluster into practice. Secondly, I would like to thank my parents who never fail to take my phone calls when I am in need. Last, I would also like to thank my friend Rong Lu for her suggestion on the art design of this poster.

References

Docker Inc. (n.d.). Enterprise Container Platform. Retrieved July 23, 2019, from https://www.docker.com/
Microsoft. (n.d.). .NET Framework. Retrieved July 17, 2019, from https://hub.docker.com/_/microsoft-dotnet-framework
Swatski, S. (2014). Investigating the Use of pMatlab to Solve the Poisson Equation on the Cluster maya(Tech.). Baltimore, MD: The University of Maryland, Baltimore County. doi:10.13016/M2CC0TX59
Tang, K. (2019, July 17). Matlab-mcr-win. Retrieved from https://hub.docker.com/r/kevintang233/matlab-mcr-win

Structure Design

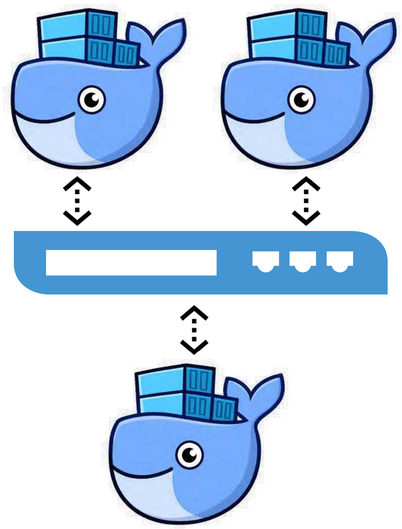

Figure 1. Structure of the Docker Swarm Cluster

Figure 2. Structure within a Docker container

Implementation

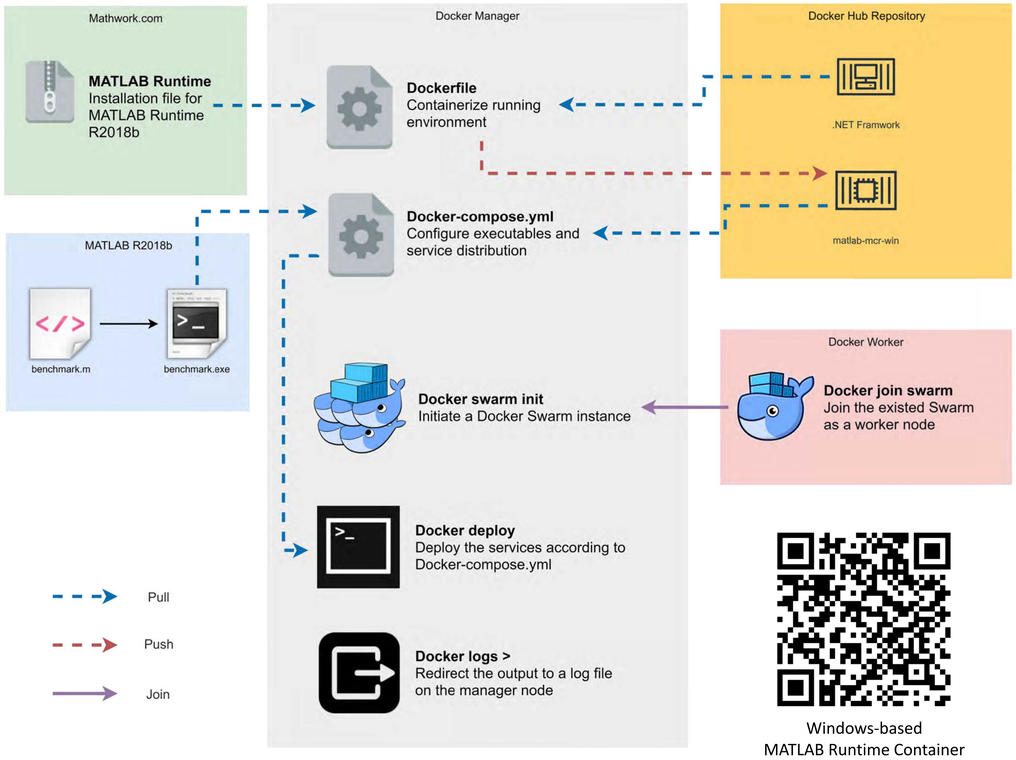

Figure 3. Construction of the Cluster and Service Deployment

Result

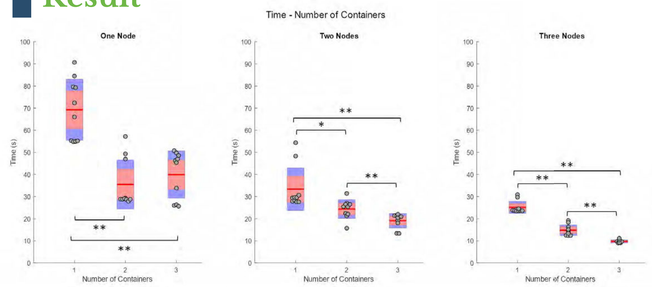

*: $p < .05$; **: $p < .001$
Figure 3. T-test between the performance of different node-container configuration with number of nodes as control variable.

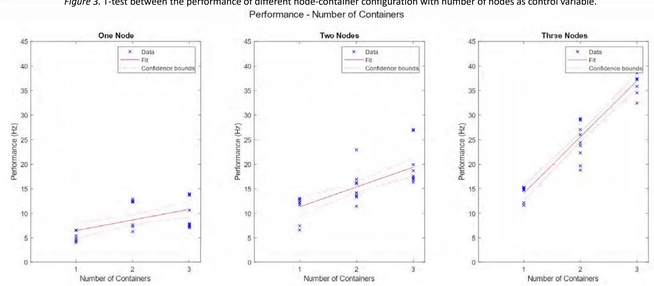

Figure 4. Linear regression predicting performance based on number of containers with number of nodes as control variable.

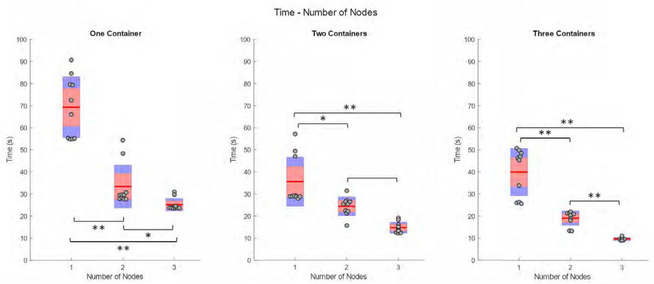

*: $p < .05$; **: $p < .001$
Figure 5. T-test between the performance of different node-container configuration with the number of containers as control variable.

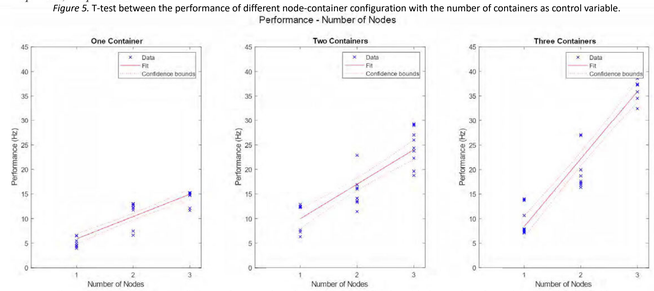

Figure 6. Linear regression predicting performance based on the number of nodes with the number of containers as control variable.

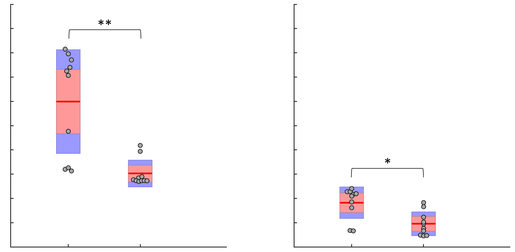

*: $p < .05$; **: $p < .001$
Figure 7. T-test between the performance of different node-container configuration with the total number of containers as control variable.

Effect of diet on gut microbiome and metabolic pathways

Siddhartha Kalala[1], Yuanchao Ye[2,3], Mohamad Mokadem[2,3]

1. Cedar Falls High School, Cedar Falls, IA

2. Department of Internal Medicine, Gastroenterology and Hepatology, University of Iowa, Iowa City, IA

3. Fraternal Order of Eagles Diabetes Research Center, University of Iowa, Iowa City, IA

Research Question: What is the effect of diet on gut microbiota composition and bacterial metabolic pathways?

Background

- Gut microbiota has been lately associated with shaping many human health conditions, including obesity and its associated metabolic disorders.
- It has been previously reported that obese humans and animals have different microbial composition residing in their gut. Furthermore, transferring microbiota from an obese individual to a leaner one was shown to induce obesity in the recipient irrespective of the type of diet.
- Finally, diet has been found to be one of the main factors molding our gut microbiota.

Methods

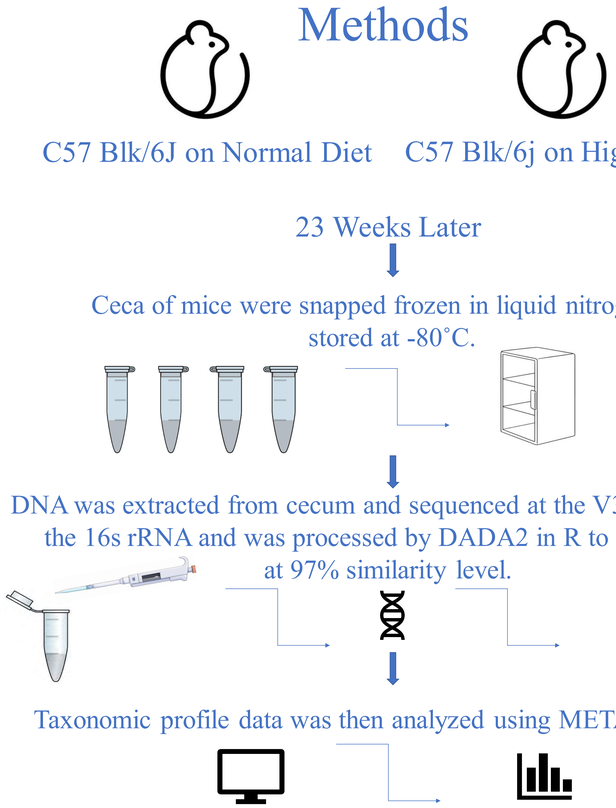

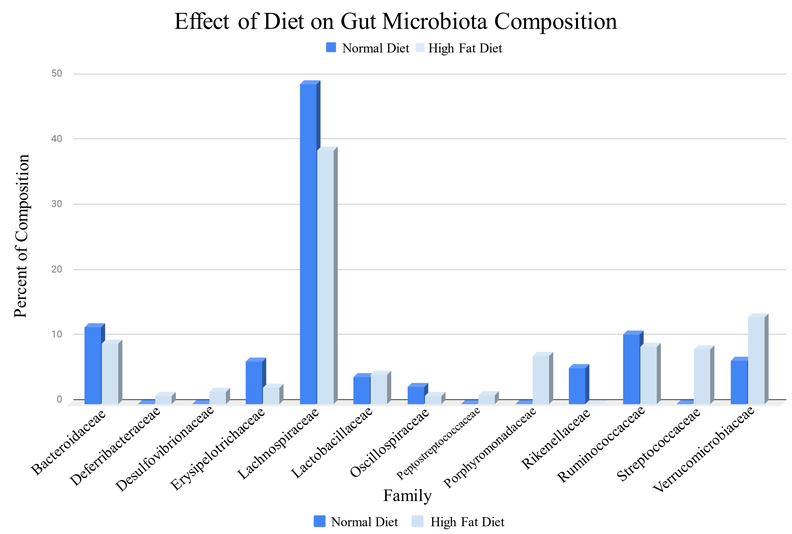

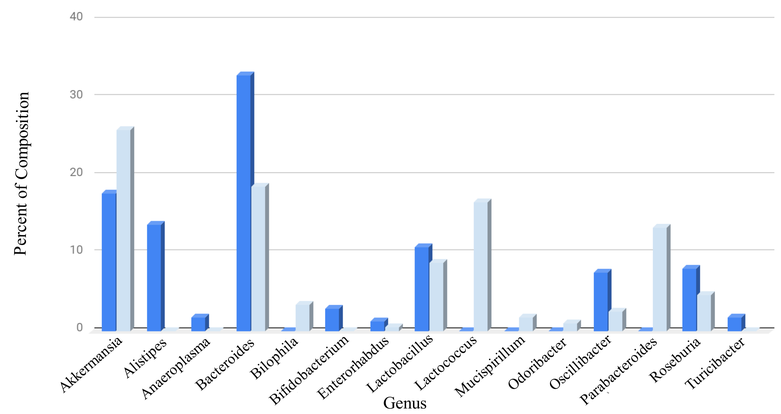

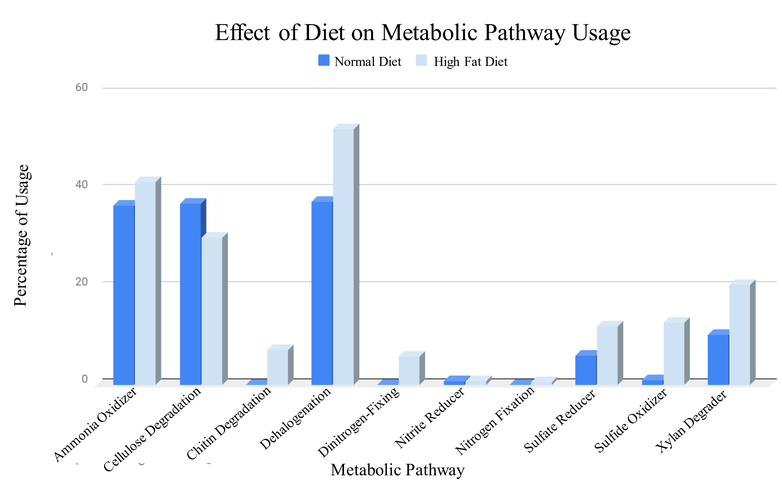

Discussion/Conclusion

1. High fat diet induces minimal but significant changes in the gut microbiota at the family level. An increase in Desulfovibrionaceae, Peptostreptococcaceae, Streptococcaceae, and Verrucomicrobiaceae, as well as a decrease in Erysipelotrichaceae and Lachnospiraceae has been associated with a state of obesity and metabolic derangement.

2. More pronounced changes were observed at the genus level. A decrease in *Bacteroides and Alistipes*, and an increase in *Lactococcus* and *Parabacteroides* was detected in high fat diet-fed mice. These bacterial genera have also been associated with a state of obesity and metabolic derangement. Paradoxically, we observed an increase in *Akkermansia*, which has been attributed to a leaner, healthier state.

3. At the bacterial metabolic pathway level, we observed an increase in chitin and xylan degradation, dehalogenation, sulfate reduction and sulfide oxidation in high fat diet-fed mice compared to those on a regular diet. Many of these molecular reactions have been associated with increased utilization of alternative energy source. These findings suggest that a high fat diet induces a newer gut environment that is more avid for energy harvest.

Acknowledgements

I would like to thank the Belin-Blank Center, SSTP, Dr. Mokadem and his research group, and the University of Iowa for providing me with the opportunity to do this research.

References

Ley, Ruth E., Backhed, Fredrik, Turnbaugh, Peter, Lozupone, Catherine A., Knight, Robin D., & Gordon, Jeffrey I. (2005). Obesity alters gut microbial ecology.(MICROBIOLOGY)(Author Abstract). *Proceedings of the National Academy of Sciences of the United States, 102*(31), 11070-11075.

Ley, R., Turnbaugh, P., Klein, S., & Gordon, J. (2006). Human gut microbes associated with obesity. *Nature, 444*(7122), 1022-1023.

Peter J. Turnbaugh, Ruth E. Ley, Michael A. Mahowald, Vincent Magrini, Elaine R. Mardis, & Jeffrey I. Gordon. (2006). An obesity-associated gut microbiome with increased capacity for energy harvest. *Nature, 444*(7122), 1027-1031.

Patients' Consent For Supervised Pelvic Exams Under Anesthesia, Performed by Medical Students

Krisha Keeran, Emily Jacobs MD, Karen Summers MPH, Rachel Mejia DO
Department of Obstetrics and Gynecology, University of Iowa Hospitals and Clinics

The University of Iowa | Belin-Blank Center

The University of Iowa

Research Objectives

- Determine the proportion of patients who give consent for a medical student to perform a supervised pelvic exam under anesthesia
- Analyze the possible variables that may impact a patient's choice to consent for a supervised pelvic exam by a medical student under anesthesia

Background

- Medical students often perform pelvic exams for educational purposes at training hospitals[1]
- Eight states have prohibited nonconsensual pelvic exams [1]
- Prior studies have demonstrated that many physicians are not regularly consenting patients for pelvic exams under anesthesia performed by medical students [2]
- Medical students are often uncomfortable with the thought of performing pelvic exams on patients who they believe have not been unequivocally consented [3] [4]
- When surveyed, 62% of patients indicated that they would give consent to medical students to perform pelvic exams [5]
- No prior studies have determined patients' actual consent rates to a supervised pelvic exam performed by a medical student under anesthesia

Methods

Sample selection

- Retrospective data review conducted with data from UIHC patients from May 1, 2016 – December 31, 2017

Abstracted data from UIHC records/specimens and EPIC

- Fields examined:
  - patient age
  - surgical procedure
  - surgeon
  - surgical OB/GYN division
  - individual acquiring consent
  - if the patient consented to a medical student performing a supervised pelvic exam under anesthesia

Analyzed Data

- Statistical analysis performed using SPSS:
  - Descriptive Statistics
  - Chi square
  - T-test

Sample Characteristics

Patient inclusion/exclusion criteria

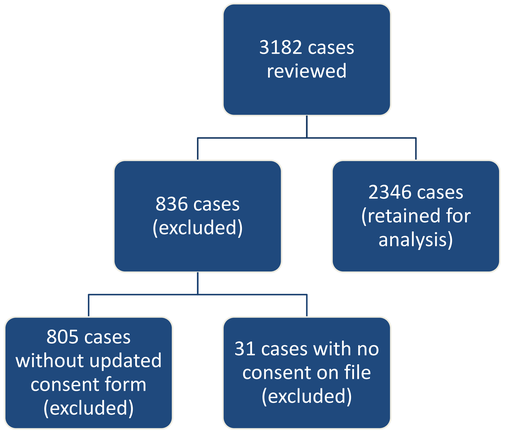

		Total sample (n=2346)
Age	Mean ± SD	51 ± 17.3
	Range	9 - 98
Approach	Laparoscopy	44.3% (1039)
	Laparotomy	16.5% (388)
	Vaginal	36.3% (852)
	Laparoscopy and Vaginal	1.9% (44)
	Other	0.9% (22)
Divisions	General Obstetrics and Gynecology	27.8% (652)
	Gynecologic Oncology	51.0% (1196)
	Reproductive Endocrinology and Infertility	10.8% (254)
	Urogynecology and Reconstructive Pelvic Surgery	10.4% (244)
Consenter Roles	Fellow	11.0% (259)
	Nurse Practitioner	0.3% (8)
	Resident	57.2% (1343)
	Staff	31.4% (736)

Results

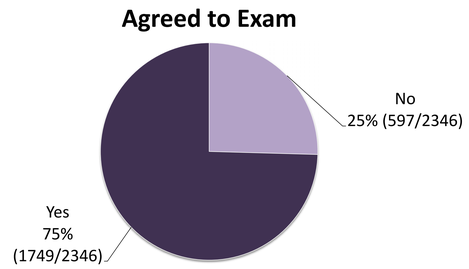

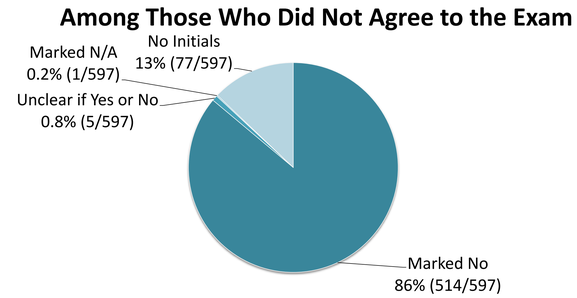

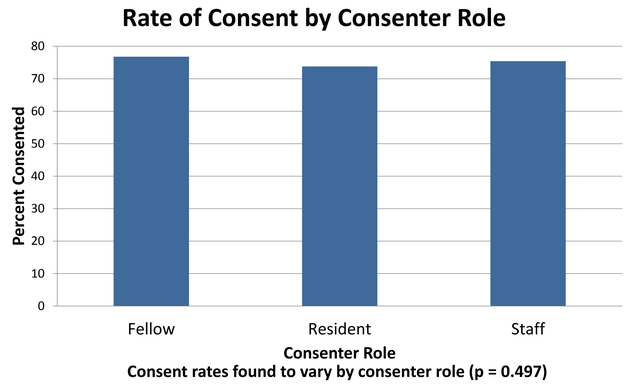

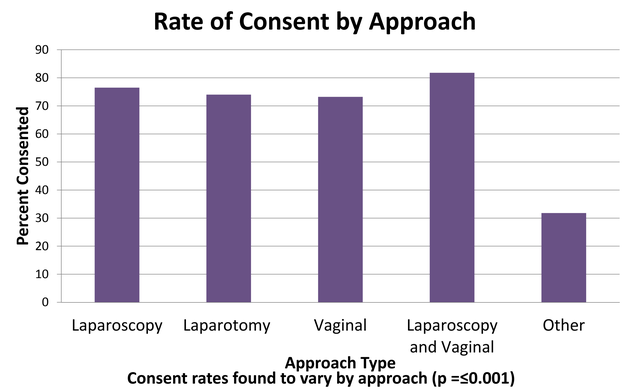

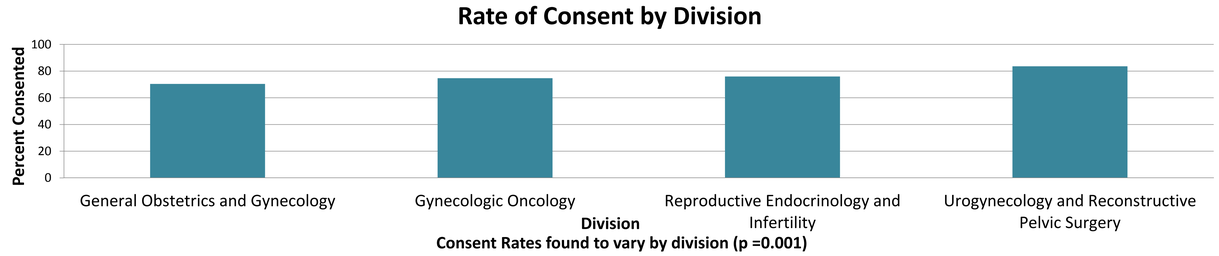

Conclusions

- 75% of patients consented to a supervised pelvic exam under anesthesia performed by a medical student
- No evidence of relation between consenter role and consent rate (p = 0.497)
- Evidence of relation between procedure approach and consent rate (p ≤ 0.001)
- Evidence of relation between division and consent rate (p = 0.001)

Implications

- It does not appear that this update to the consent form inhibits learning opportunities for medical students
- Institutions in other states can use this information when planning to update their consent forms and address concerns

Future Directions

- Determine the percentage of university-affiliated hospitals that require patients to sign consent forms for exams under anesthesia by medical students
- Conduct a process evaluation to examine reasoning behind consent form errors
- Examine reasons for denial of consent from a patient's perspective

Acknowledgements

Special thanks to Karen Summers, Dr. Mejia, Dr. Jacobs, all members of the Department of Obstetrics and Gynecology, the Belin-Blank Center, the Secondary Student Training Program for their assistance in making this research study possible

References

1. Tsai, J. (2019). Medical students regularly practice pelvic exams on unconscious patients. Should they? *Elle.* Retrieved from https://www.elle.com/life-love/a28125604/nonconsensual-pelvic-exams-teaching-hospitals/
2. Wolfberg AJ. (2007). The patient as ally – learning the pelvic examination. *N Engl J Med,* 356 (9): 889-890. doi: 10.1056/NEJMp068016
3. Tocce K, Teal SB. (2013). Practicing pelvic examinations by medical students on women under anesthesia: why not ask first? *Obstet Gynecol,* 121 (2 Pt 1): 378. doi: 10. 1097/AOG.0b013e3182677a28
4. Gibson, E., & Downie, J. (2012). Consent requirements for pelvic examinations performed for training purposes. *CMAJ: Canadian Medical Association journal = journal de l'Association medicale canadienne,* 184(10), 1159-1161. doi: 10. 1503/cmaj. 110725
5. Wainberg, S., Wrigley, H., Fair, J., Ross, S. (2010). Teaching pelvic examinations under anesthesia: what do women think? *J Obstet Gynaecol Can,* 32 (1), 49-53. doi: 10.1016/S1701-2163(16)34404-8.
6. SPSS Inc. Released 2017. SPSS for Windows, Version 25.0. Armonk, NY: IBM Corp.

Quantification of the Mechanical Properties of Crystalline 9-Anthracene Carboxylic Acid Ribbons

Vedanta Kompella[1], Thiranjeewa Lansakara[2], Alexei Tivanski[2]

Kennedy High School, Cedar Rapids, IA[1]; Department of Chemistry, The University of Iowa[2]

The University of Iowa

Belin-Blank Center
College of Education
The University of Iowa

Background

9 –Anthracene Carboxylic Acid (9-ACA)

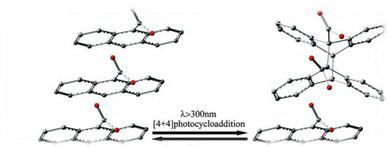

- 9-Anthracene Carboxylic Acid (9ACA) is a crystalline material which **changes it shape when exposed to light** (**[**4+4] Photo**dimer**ization)
- Forms **Ribbons** at the **Microscale**
- **Reverts to its original form** (eventually)
- **Ribbons twist** (2-4 min), then untwist (5-15 min)
- Can be **repeated** for **multiple cycles**
- Ideal for application as **actuators** in **small machines** because **unaffected by illumination conditions**

Atomic Force Microscopy (AFM)

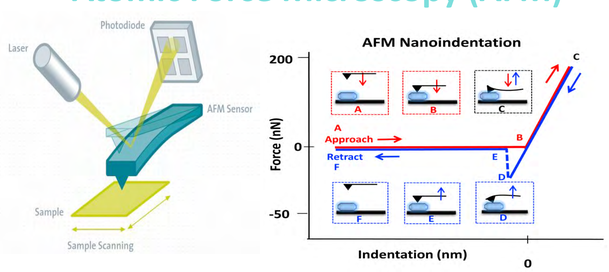

- AFM uses a sharp tip to indent samples
- Data is the **force** vs **tip's indentation depth**
- use **models** which **fit the data** to determine mechanical **properties**
- Use **Johnson-Kendall-Roberts (JKR) Model** to find the **Young's Modulus (measure of elasticity)**

Objectives

1. How does elasticity of Ribbons change **after exposure** to **light**?
2. What's the **difference** in elasticity between Macro Crystals and Ribbons?

Methodology

We often experienced **low yields** of ribbons, and even then, they tended to **agglomerate** (making them unusable for the AFM).

Drying the ribbons faster (via a desiccator w/vacuum or smaller drops on slides) seemed to stop the latter.

Achieving more accurate concentrations and **adding more solution** (like 3.8 mg in 2 ml) **even slower** seemed to increase yield.

Macro Crystals Synthesis: Slow Evaporation

- **5.7 mg 9-ACA** dissolved in **1.0 mL filtered ethyl acetate**
- vial **sealed** with a **polyethylene lid pierced by a needle**
- crystallized as ethyl acetate evaporated over many days
- Crystals **ground up** before use in the AFM **(very rough)**

UV Irradiation

- Used **Metal Halide Lamp (200 W, 10%)** for irradiation
- UV Light filter: **360 nm**
- Exposed for **1-2 min**
- 9-ACA exhibited **fluorescence (both forms)**

Micro Ribbons Synthesis: Floating Drop Method

- **1.9 mg 9-ACA** dissolved in **1.0 mL filtered ethyl acetate**
- **slowly added** to surface of MilliQ **purified H_2O in Petri dish**
- covered and left in the dark for 48 h (for solvent evaporation)
- Pipetted onto a **quartz slide** for AFM use

Results and Discussion

Optical Microscope Images of Crystalline 9-ACA

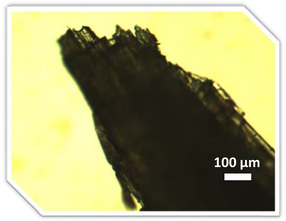

Crystals Before UV

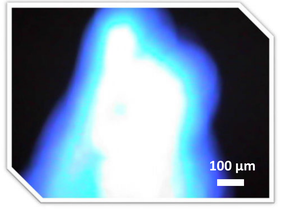

Crystals After UV

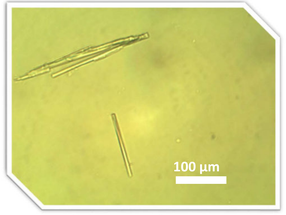

Ribbons Before UV

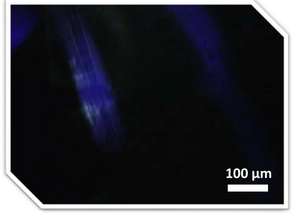

Ribbons After UV

Results:

- Ribbons have **unusually high** Young's Modulus before exposure (9.6-13.4 GPa vs 1-7 GPa)
- Ribbons become MUCH **more elastic after** light exposure (more than 2x)
- **Less variability** in their elasticity **after exposure**
- Ribbons **slightly less elastic** than Macro Crystals (9.58 GPa)
- Crystals and Ribbons have **approx. same variability in elasticity**
- Crystal and Ribbons have **similar elasticity**

Powdered X-Ray Diffraction (PXRD)

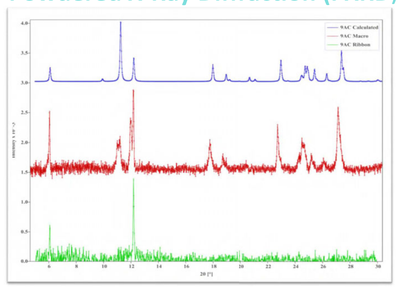

AFM Results for Young's Modulus

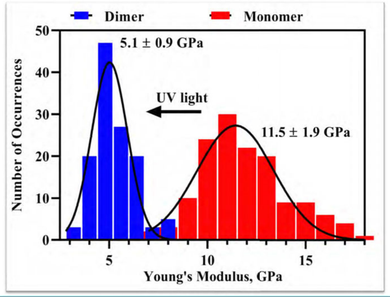

AFM Micro Ribbon Imaging

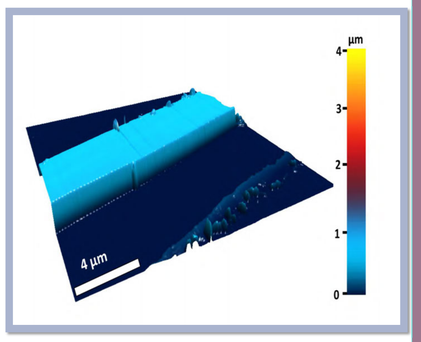

- **Increased Adhesion force after exposure** to light (5.2 nN vs 8.2 nN)
- Ribbons have higher aspect ratio (width/height) than needles (20 vs. 6)

Conclusions

Implications

- **Higher elasticity of photo reacted ribbons explains why ribbons don't shatter, but twist**
- Fluorescence seemed to fade away over multiple cycles (like previous studies)
- Photobleached Ribbons didn't revert to the monomeric form, showed no fluorescence (unlike more robust nanorods of 9-ACA)
- Similar elasticity of Ribbons and Crystals – probably probing on same crystallographic plane (002 or 004, unknown)
- PXRD confirms sample is 9-ACA, Fluorescence and changes in Adhesive Force confirms [4+4] Photodimerization

Future Directions

- Understanding why ribbons have large Young's Modulus and relation to crystal planes
- Finding hardness of ribbons and macro crystals for engineering applications
- Seeing how elasticity and hardness changes over multiple cycles and with photobleaching
- Calculating optical to mechanical energy conversion factor (see usefulness as actuator)
- Finding mechanical properties of better derivatives (such as 4-Flouro 9-ACA)
- Finding the mechanical properties of other Micro ribbons for comparison (9-Methyl Anthracene, 4 chlorocinnamic acid, etc.)

Acknowledgments

Special thanks to the Tivanski Lab for Mentorship and Guidance!

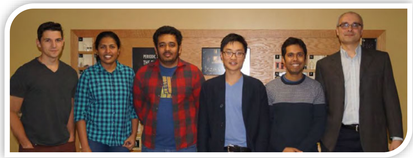

References

1. Kaupp, G. (1992). Photodimerization of anthracenes in the solid state: New results from atomic force microscopy. Angewandte Chemie International Edition in English, 31(5), 595-598. doi:10.1002/anie.199205951
2. Kim, T., Zhu, L., Al-Kaysi, R. O., & Bardeen, C. J. (2014). ChemInform Abstract: Organic Photomechanical Materials. ChemInform, 45(25). doi:10.1002/chin.201425297
3. Zhu, L., Al-Kaysi, R. O., Dillon, R. J., Tham, F. S., & Bardeen, C. J. (2011). Crystal structures and photophysical properties of 9-Anthracene Carboxylic Acid derivatives for photomechanical applications. Crystal Growth & Design, 11(11), 4975-4983. doi:10.1021/cg200883b
4. Zhu, L., Al-Kaysi, R. O., & Bardeen, C. J. (2011). Reversible photoinduced twisting of molecular crystal microribbons. Journal of the American Chemical Society, 133(32), 12569-12575. doi:10.1021/ja201925p
5. Zhu, L., Tong, F., Salinas, C., Al-Muhanna, M. K., Tham, F. S., Kisailus, D., Bardeen, C. J. (2014). Improved solid-state photomechanical materials by fluorine substitution of 9-Anthracene Carboxylic Acid. Chemistry of Materials, 26(20), 6007-6015. doi:10.1021/cm502866e
6. Zhu, L. (2011). Solid-state Photochemical and Photomechanical Studies of Nanostructures and Microstructures of Anthracene Derivatives. UC Riverside. ProQuest ID: Zhu_ucr_0032D_10642. Merritt ID: ark:/13030/m5fx7dc8. Retrieved from https://escholarship.org/uc/item/6mc871s2
7. https://www.witec.de/assets/Uploads/WITec-AFM-Principle.png

The Effects of Stimulant Medication Status on Task Switching Performance in Youth with ADHD

Margaret Li [1], Jonathan Schacherer, B.S.[2], and Eliot Hazeltine, Ph.D.[2]

[1] Palo Alto High School, Palo Alto, CA, [2] Department of Psychological & Brain Sciences, University of Iowa

INTRODUCTION

- Attention Deficit Hyperactivity Disorder (ADHD) is one of the most commonly diagnosed neurodevelopmental disorders.
- Behaviorally, ADHD is characterized by inattention, hyperactivity, or a combination of the two.
- Due to decreased frontal lobe efficiency, individuals with ADHD also exhibit deficits in various cognitive processes like inhibitory control (Tamm et al., 2004).
- To assess inhibitory deficits, task-switching procedures are often used.
- Previous work using a task-switching paradigm has demonstrated increased response time and error rate performance in ADHD youth (Cepeda et al., 2000).
- To ameliorate the cognitive deficits in ADHD, many individuals are prescribed stimulant medication (e.g., Ritalin, Adderall).

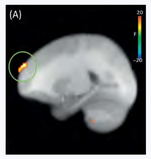

- Questions persist regarding whether information acquired under the influence of medication affects performance when tested.
- Medication and practice are both known to improve task performance, but how these factors interact is uncertain (Swanson & Kinsbourne, 1976).

Figure 1. Individuals with ADHD exhibit less volume in the left inferior frontal gyrus, which contributes to higher cognitive functions and the working memory required for learning

OBJECTIVES

1) Examine whether ADHD children exhibit impaired task-switching performance compared to non-ADHD children and how medication helps to alleviate some of these deficits.
2) Assess how the correspondence between medication status on Day 1 and Day 2 affects overall performance.

PROCEDURE

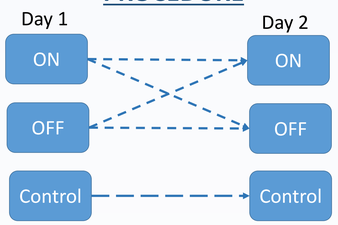

Figure 2. Randomization procedure for all groups: participants with ADHD completed the tasks either on or off medication on Day 1, and the opposite on Day 2.

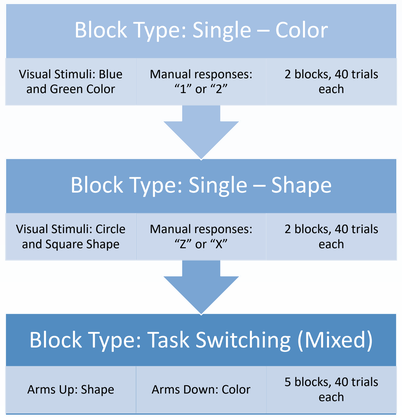

Figure 3. Participants were instructed to execute their responses accordingly based on block types: single or mixed

METHODS AND FIGURES

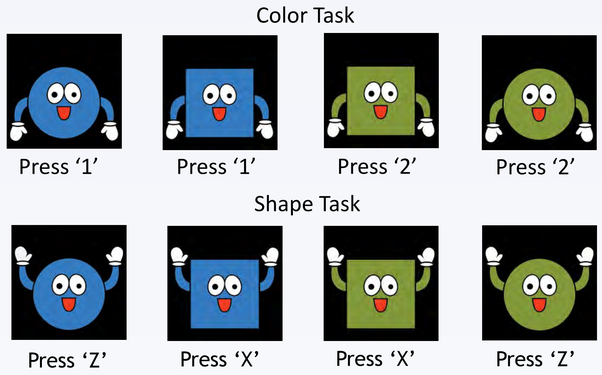

Figure 4. Single Task Stimuli and Corresponding Manual Responses

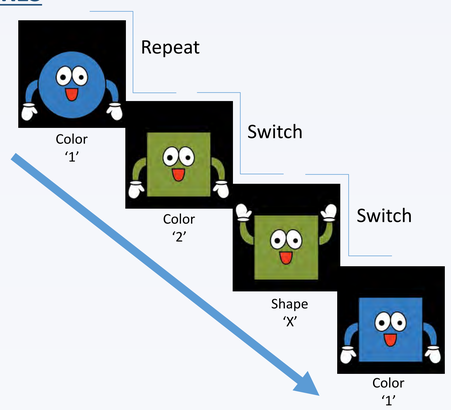

Figure 5. Task Switching Block: Repeat vs. Switch trials

RESULTS: RESPONSE TIME (RT)

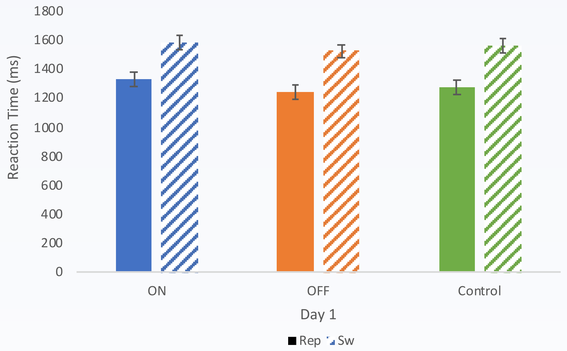

Figure 6. Day 1 Mean RTs for Repeat and Switch trials

On Day 1, the reaction times for switch trials are longer than repeat trials. The switch costs (switch RT – repeat RT) are similar for all groups.

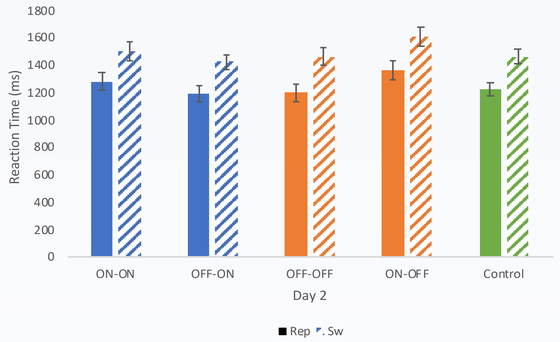

Figure 7. Day 2 Mean RTs for Repeat and Switch Trials

On Day 2, the reaction times for switch trials are longer than repeat trials. The switch costs (switch RT – repeat RT) are similar for all groups but are smaller compared to Day 1.

RESULTS: ERROR RATE (ER)

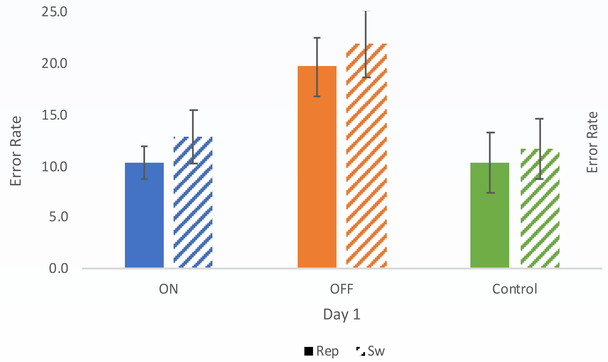

Figure 8. Day 1 Mean ERs are reported for Repeat and Switch trials

On Day 1, the error rate of the OFF group was substantially higher compared to the ON and control groups. The error rates for switch trials were higher than repeat trials across all groups. The switch costs remain similar across all groups.

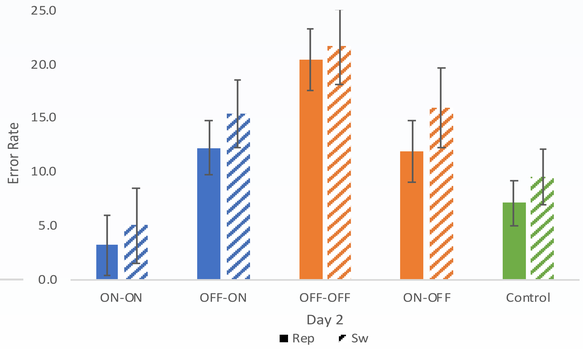

Figure 9. Day 2 Mean ERs for Repeat and Switch trials

On Day 2, the error rate of the ON-ON group was smaller compared to all other ADHD groups. Switch trials still remain less accurate than repeat trials across all groups. The switch costs also remain similar across all groups.

ANALYSIS

Demographic and Behavioral Data for the ADHD and Control Groups

Variable	ON-ON	OFF-OFF	ON-OFF	OFF-ON	Control
Sex	7 M; 3 F	6 M; 4 F	6 M; 3 F	8 M; 5 F	8 M; 11 F
Age	12.00 (1.19)	11.91 (2.16)	12.10 (2.19)	11.77 (2.30)	11.92 (1.44)
Medication dosage (mg)	39.80 (12.85)	27.67 (12.854)	32.78 (18.60)	26.62 (17.94)	26.62 (17.94)
WRAT-Reading Scaled score	106.30 (15.17)	105.70 (8.33)	104.25 (11.56)	105.85 (12.01)	109.11 (11.73)
Conners-3 Parent t-scores					
Hyperactivity	71.60 (20.34)	74.5 (15.79)	70.22 (18.12)	75.77 (17.33)	48.58 (9.48)
Inattentive	76.40 (12.48)	78.5 (10.12)	79.11 (11.06)	77.23 (11.19)	48.11 (9.48)
Learning	63.10 (11.54)	71.9 (13.79)	60.44 (11.36)	61.46 (12.53)	47.53 (6.64)

Table 1. Reported means (standard deviations) for demographics and behavioral data for all groups

Response Time Significance

RT Significance	F(1, 55)	p-value	ηp2
Day	7.670	0.008	0.122
Trial type	291.50	<.001	0.841
Day*Trial type	7.240	0.009	0.116

Between Subjects	F(4, 55)	p-value	ηp2
Group	1.240	0.307	0.082

Table 2. Response time significance was found in differences between day and trail type

Error Rate Significance

ER Significance	F(1, 55)	p-value	ηp2
Day	4.130	0.047	0.070
Trial type	13.44	0.001	0.196

Between Subjects	F(4, 55)	p-value	ηp2
Group	4.920	0.002	0.264

Table 3. Error rate significance was found in differences between day, trail type, and medication groups

CONCLUSION

- Overall, stimulant medication appears to improve children with ADHD's ability to inhibit the previous, now-irrelevant task and prepare for the upcoming task compared to those off medication. Performance between ADHD-ON and controls was near-equivalent.
- We found no evidence of state-dependent or drug-induced facilitated learning. Rather, the interaction between medication status on Day 1 and Day 2 appears to drive performance such that the number of times an ADHD youth is off medication worsens overall performance.

REFERENCES

Cepeda, N. J., Cepeda, M. L., & Kramer, A. F. (2000). Task switching and attention deficit hyperactivity disorder. *Journal of Abnormal Child Psychology*, *28*(3), 213-226.

Swanson, J., & Kinsbourne, M. (1976). Stimulant-Related State-Dependent Learning in Hyperactive Children. *Science*, *192*(4246), 1354-1357.

Tamm, L., Menon, V., Ringel, J., & Reiss, A. L. (2004). Event-related FMRI evidence of frontotemporal involvement in aberrant response inhibition and task switching in attention-deficit/hyperactivity disorder. *J Am Acad Child Adolesc Psychiatry*, *43*(11), 1430-1440.

ACKNOWLEDGEMENTS

Special thanks to Jonathan Schacherer and Dr. Eliot Hazeltine for their guidance on this project and the Belin Black Center for their support. This project was partially funded by the U of Iowa GPSG program.

Effect of mesocarnivores on nesting bird abundance

Jason Liang[1], Heather Sander[2], Brandon McDougall[2]
Westford Academy[1], University of Iowa[2]

Belin-Blank Center, College of Education, The University of Iowa

The University of Iowa

Background

- Urban environments play a key role in conserving biodiversity (1-3)
- Studies of relationships between different groups of urban species such as mesocarnivores and nesting birds are needed to build knowledge of urban biotic communities and support the design of urban biodiversity conservation approaches

Research Objective: To identify effects of mesocarnivore presence on bird nesting guild abundance

- Expected effect to vary with mesocarnivore species and nesting guild
- Presence of ground-dwelling mesocarnivores will negatively influence ground and shrub nester abundance and have no significant link with tree nester abundances.
- Tree-climbing mesocarnivores will negatively impact tree nesters.

Methodology

- Mammal sites were identified by arraying three transects along an urbanization gradient across the study area (4)
- Divided transects into 10 km^2 blocks within which we selected 4 sample sites using random sampling stratified by land cover.
- Sampled mesocarnivores on each of the resulting 39 sites by deploying motion-sensitive trail cameras for 30 days in July (2017-2018) and identified 9 species. Considered mesocarnivore species present if detected by camera on a site.

- Identified 3-5, 50-m bird survey sites within 1 km of each mammal site using land-cover based stratified random sampling.
- Surveyed sites at least twice in June and July, 2017-18, recording counts of all species seen or heard. We recorded 59 native species.
- Used counts to indicate breeding-season abundance of each species on each site
- Aggregated counts to bird nesting guild (tree, shrub, ground, primary cavity, secondary cavity) to identify abundance of birds in each guild on each birding site.
- Matched these with mesocarnivore detections to identify presence of mesocarnivores at bird sites

- Analyzed resulting dataset using Wilcoxon rank-sum tests to identify significance of differences in nesting guild abundance with and without each mesocarnivore.

Results

Abundance of most nesting guilds did not differ significantly when most mesocarnivore species were present.

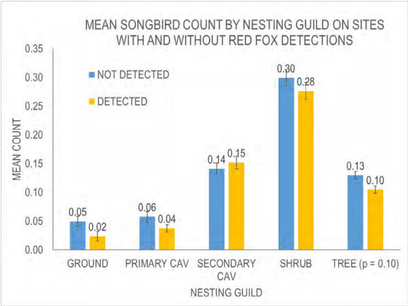

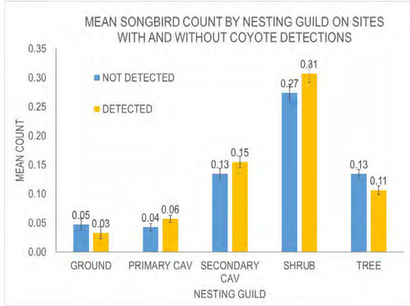

Tree nester abundance was lower when red foxes were present, but not significantly (p = 0.10)

Secondary cavity nester abundance was significantly lower when house cat (*Felis catus*) and Virginia opossum (*Didelphis virginiana*) were present (p < 0.05)

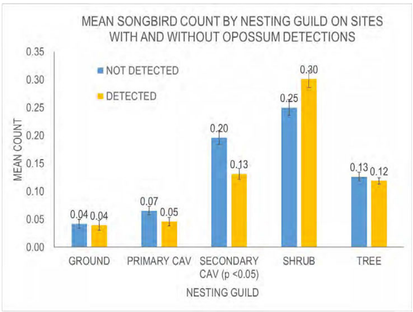

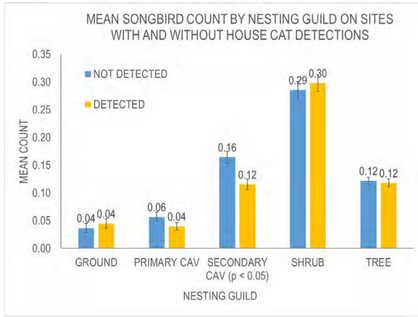

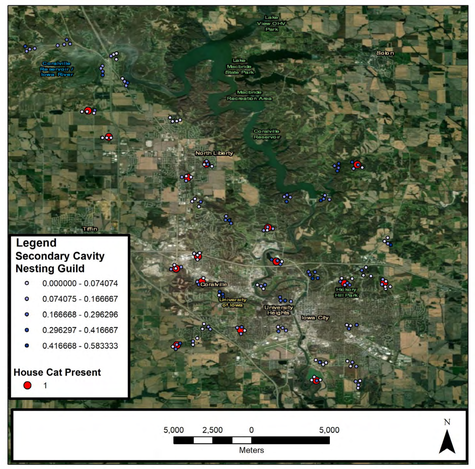

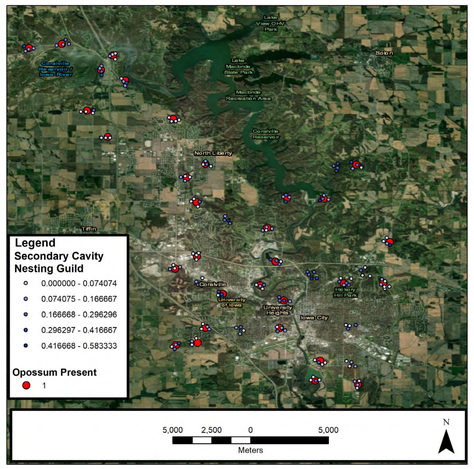

Conclusions and Implications

Key Findings

- Most nesting guilds are uninfluenced by mesocarnivores
- Cat and opossum may reduce secondary cavity nester abundance
- Red fox may reduce tree nester abundance.

Conservation Implications

- Conservation of secondary cavity and tree nesters should consider cat, opossum, and red fox management.
- Overpopulation of these guilds or their rarity in resource-rich habitats may signal the need to manage these mesocarnivores for population control or to reduce predation.

Future Studies

- We used nesting songbird abundance and mesocarnivore occurrence estimates that were not adjusted for detectability. Future analyses should use detectability-adjusted estimates.
- Inspect similar relationships across all seasons instead of just breeding season
- Consider other environmental attributes that could influence songbird abundance and mesocarnivore presence

Scan me

References

1. Aronson MFJ et al. (2014) A global analysis of the impacts of urbanization on bird and plant diversity reveals key anthropogenic drivers. *Proc R S Lond B: Biol Sci281*.
2. Ellis EC (2013) Sustaining biodiversity and people in the world's anthropogenic biomes. *Curr Opin Environ Sust 5*, 368-372.
3. Ellis EC, Ramankutty N (2008) Putting people in the map: Anthropogenic biomes of the world. *Frontiers in Ecology and the Environment 6*, 439-447.
4. Magle et al. (2019). Advancing urban wildlife research through a multi-city collaboration. *Front Ecol Evolution 17*, 232– 239.

Acknowledgements

I'd like to thank Heather Sander, Brandon Macdougall, Adam Skibbe, and Steve Hendrix for all the mentorship, help, and support they graciously provided me during these five weeks of research.

Optimizing gene delivery for osteodifferentiation by varying ratio of pFGF-2 to pBMP-2

Jessica Luan[1] Timothy Acri[2], Dr. Aliasger K. Salem[3]

[1]Amador Valley High School, [2,3]Department of Pharmaceutical Sciences and Experimental Therapeutics, University of Iowa

Introduction

- Certain types of bone fractures cannot heal spontaneously and therefore require therapeutic intervention (Einhorn and Gerstenfeld, 2014)
- FGF-2 and BMP-2 are proteins that regulate the differentiation of osteoblasts (bone-forming cells) from unspecialized stem cells.
- Co-delivery of genes encoding for BMP-2 and FGF-2 synergistically enhances bone formation. (Atluri, Seabold, Hong, Elangovan, & Salem, 2015)

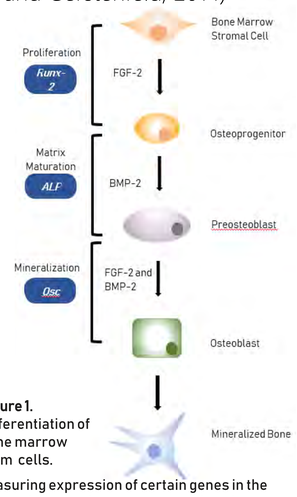

Figure 1. Differentiation of bone marrow stem cells.

Measuring expression of certain genes in the differentiation pathway may indicate osteogenic potential of different ratios of FGF-2 and BMP-2.

Research Objective

- Maximize cell viability and transfection efficiency of PEI-pDNA complexes
- Determine ratio of pFGF-2 and pBMP-2 that optimizes bone formation

Nanoplex Fabrication

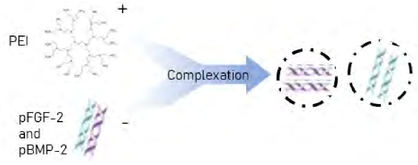

Figure 2. Fabrication of PEI-pDNA complexes. The positively charged amine groups (N) on PEI form electrostatic interactions with negatively charged phosphate (P) backbone in DNA allowing for formation of complexes.

Nanoplex Characterization

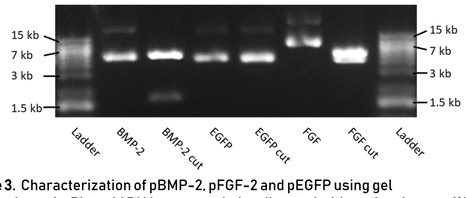

Figure 3. Characterization of pBMP-2, pFGF-2 and pEGFP using gel electrophoresis. Plasmid DNA was restriction digested with agel and run on 1% agarose gel. Lengths of pDNA fragments matched standard values

Nanoplexes	Size (nm) ± SEM	PDI ± SEM	Zeta Potential (mV) ± SEM
PEI-pBMP-2	127.4 ± 1.7	0.1385 ± .001061	34.61667 ± .42694
PEI-pFGF-2	130.7 ± 1.7	0.1385 ± .002475	34.16667 ± .683943
PEI-pEGFP	86.285 ± .865	0.223 ± .007071	31.26667 ± 1.185093

Table 1. Size, polydisperity index, and zeta potential of nanoplexes of N/P ratio of 10.

Evaluation of Cell Viability

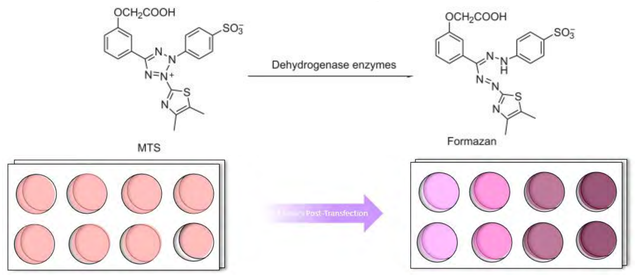

Figure 4. MTS Protocol. Color change indicates formazan production by viable cells. The degree of color change was measured spectrophotometrically to determine percent viability.

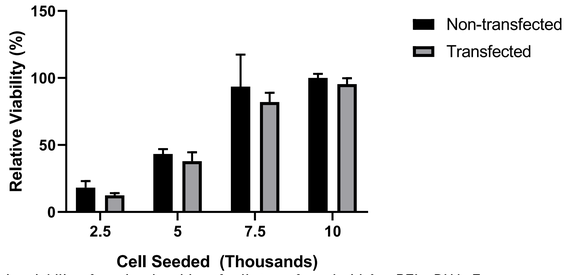

Figure 5. Relative viability of varying densities of cells transfected with 1 ug PEI-pDNA . Formazan production from MTS assay assessed spectrophotometrically. Density of 10,000 cells had highest viability 24 hours post-transfection.

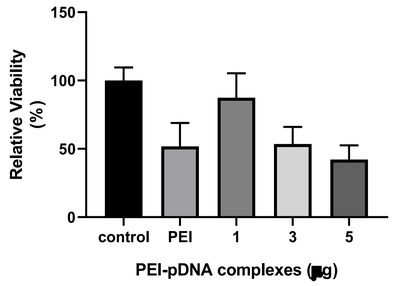

Figure 6. Relative viability of BMSCs transfected with varying amounts of PEI-pDNA complexes 24 hours post-transfection. Formazan production from MTS Assay measured spectrophotometrically. 1 ug of nanoplexes was determined to be least cytotoxic.

Evaluation of Transfection Efficiency

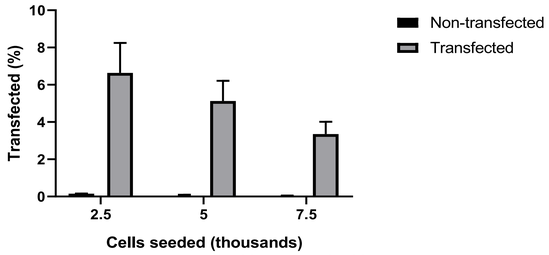

Figure 7. Transfection efficiency at varying BMSC densities. BMSCs successfully transfected with pEGFP were gated using flow cytometry at 48 hours post-transfection. Non-transfected cells were included as a reference. 2,500 cells/well exhibited highest transfection efficiency.

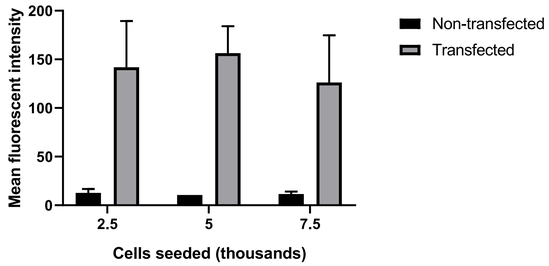

Figure 8. Mean fluorescent intensity of varying BMSC densities. BMSCs successfully transfected with pEGFP measured using flow cytometry at 48 hours post-transfection. Non-transfected cells were included as a reference. No significant difference was found in mean fluorescent intensity.

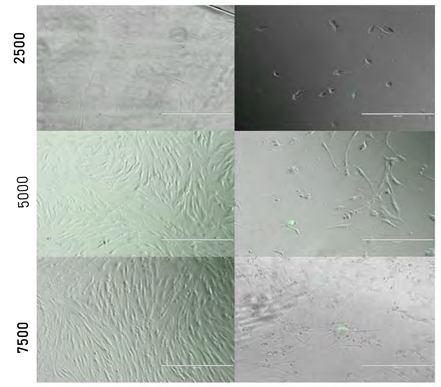

Figure 9. Fluorescent microscopy imaging of BMSCs transfected with PEI-pEGFP complexes. Differences in plasmid uptake in cell densities of 2500, 5000, and 7500 cells/well were qualitatively assessed.

Effect of co-delivery on protein production

	C	P	B	B+F0.3	B+F0.6	B+F1.0
Average	27.40588	36.25882	27.54314	27.87647	28.54314	35.82745
Std Dev n=4	18.35633	20.22893	10.88358	15.53725	17.42631	18.82544

Table 2. Average BMP-2 protein concentration (ug/uL). BMP-2 production was quantified by spectrophotometrically measuring BMP-2 secretions in supernatant using an ELISA assay.

	C	P	B	B+F0.3	B+F0.6	B+F1.0
Average	33.65101	34.83429	89.74073	40.05814	77.63075	27.58703
Std Dev n=4	16.44317	11.48195	28.07668	12.96731	41.29263	13.16083

Table 3. Average FGF-2 protein concentration (ug/uL). FGF-2 production was quantified by spectrophotometrically measuring FGF-2 secretions in supernatant using an ELISA assay.

- Previous studies have found significant increases in BMP-2 production with co-delivery of pBMP-2 and pFGF-2 (Atluri et al., 2015)
- However, no significant differences in either BMP-2 or FGF-2 production were found.

Conclusion

- Cell viability was highest when 1 ug of nanoplexes was added. Transfection efficiency decreased with increase in cell density.
- However, cell viability 24 hours post-transfection increased at higher cell densities.
  - Thus, parameters of 1 ug of nanoplexes and 10,000 cells/well seeding density were used for ELISA assays.
- ELISA results did not indicate significant differences in protein production through varying ratio of pFGF-2 and pBMP-2 complexes.
  - Expanding the range of concentrations and repeating the procedure may lead to conclusive findings.

Future Directions

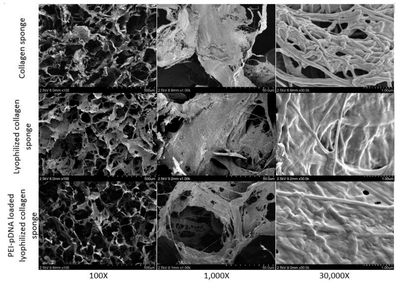

Figure 11. SEM imaging of lyophilized collagen scaffolds loaded with PEI-pDNA, lyophilized collagen sponge, and collagen sponge. Lyophilization rather than seeding with complexes changes surface morphology of collagen scaffold.

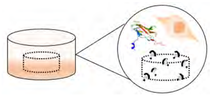

Figure 12. Visual representation of future directions. Nanoplex-loaded scaffolds may be evaluated through similar methods for cell viability, transfection efficiency, and genetic marker expression.

- Further study of osteogenic potential of free nanoplexes versus that of nanoplexes seeded on scaffolds
  - Nanoplexes are source of osteoinductive factors.
  - Scaffolds provide mechanical support necessary for osteoconduction.
  - Thus seeded scaffolds may be studied to better investigate potential clinical applications.
- Findings on optimal parameters (quantity of PEI-pDNA complexes and cell density) may be applied for future in vitro studies

Acknowledgements

Many thanks to Tim Acri, Dr. Salem and the Belin-Blank Center for making this project possible.

References

Atluri, K., Seabold, D., Hong, L., Elangovan, S., & Salem, A. K. (2015). Nanoplex-Mediated Codelivery of Fibroblast Growth Factor and Bone Morphogenetic Protein Genes Promotes Osteogenesis in Human Adipocyte-Derived Mesenchymal Stem Cells. *Molecular pharmaceutics*, *12*(8), 3032–3042./ doi:10.1021/acs.molpharmaceut.5b00297

Einhorn TA, Gerstenfeld LC. Fracture healing: mechanisms and interventions. *Nat Rev Rheumatol*. 2015;11(1):45–54. doi:10.1038/nrrheum.2014.164

Healing the costs of doing research: Repairing radiation damage with ultraviolet treatment

Liam Mackey (Highview Academy), James Wetzel (Department of Physics and Astronomy, University of Iowa)

Introduction

Hadron calorimeters are used across a wide spectrum of applications in high-energy physics, such as high-radiation environments in particle detectors.
As we endeavor to reach new energy scales in particle physics, the radiation damage incurred on components of these calorimeters will increase, necessitating the use of radiation-hard materials or methods for repairing existing materials.

We find that ultraviolet light can be used to repair radiation damage at a greatly accelerated rate compared to the natural rate, and even outpaces the decrease in transmittance caused by the radiation damage itself.

This implies that it is possible to completely remove the need to replace optical fibers – which would necessitate significant time and budgetary concerns – or continuously recalibrate detection devices by preventing damage from becoming a problem in the first place.

Methodology

Two B-2(200) WLS fibers ("Fiber 1" and "Fiber 2") were cut and polished. Both were irradiated for sixteen hours at the cesium-137 source at the University of Iowa's RadCore facility.
Fiber 1 was allowed to recover naturally with exposure to ambient light, while Fiber 2 was exposed to UV light in sub-ten minute intervals.

Spectra of both were taken using a xenon PX-2 laser processed by SpectraSuite software, the spectrum data from which was plotted using MATLAB, integrated, normalized, and checked for percent difference and systematic/random error.

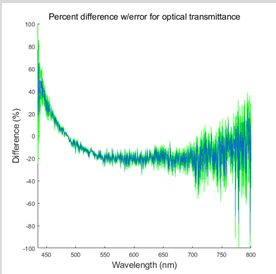

Fig. 1: Percent difference between transmittance of recovered fiber and never-irradiated fiber. Green shading represents the extent of systematic and statistical error.

Findings

- Ultraviolet treatment is definitively superior to natural recovery, leading to recovery of radiation damage at a rate (especially given Fiber 2 started out more severely damaged than Fiber 1) **significantly higher than the natural** -- as can be seen in **Fig. 5**.
- This outpaces the rate at which damage is incurred to the fibers, implying that novel new methods for repairing radiation damage using UV treatment during intrinsic calorimeter inactivity between particle collisions could be utilized to negate existing light attenuation.

Fiber 1

- This first fiber is a 59.7cm long Kuraray B-2(200) wavelength-shifting (WLS) fiber, and was left untreated with UV light to obtain the natural recovery rate from radiation damage.
- Upon receiving a dose of 21.5 kilogray of radiation, the fiber's light transmittance had dropped to 26.3% of pre-irradiation. 80% was attained at 32.5 hours, and over approximately 43 hours from start, the fiber returned to its peak (100%) transmittance.

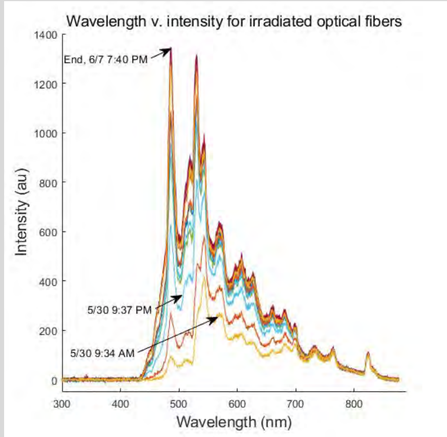

Fig. 2: Intensity of light transmitted versus wavelength for the first fiber, recovering over the week of 5/30 to 6/7.

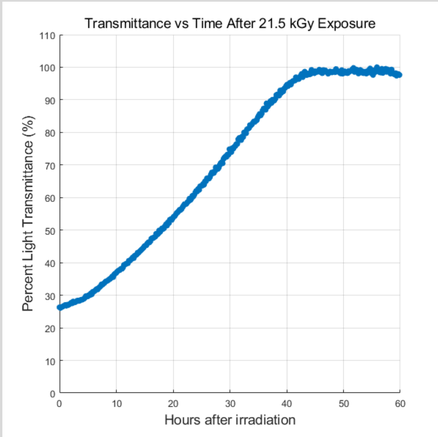

Fig. 3: Transmittance of light through the damaged fiber as a percentage of the peak value versus time (measured in hours).

Fiber 2

- The second fiber is a 60cm long Kuraray B-2(200) WLS fiber, and was treated with UV light in sub-10min direct exposures, having spectra taken every ten minutes with continuous measurement.
- Upon receiving a dose of 21.9 kilogray of radiation, the fiber's light transmittance had dropped to 20% of pre-irradiation. Over 9.6 hours, the fiber returned to 80% of baseline transmittance.

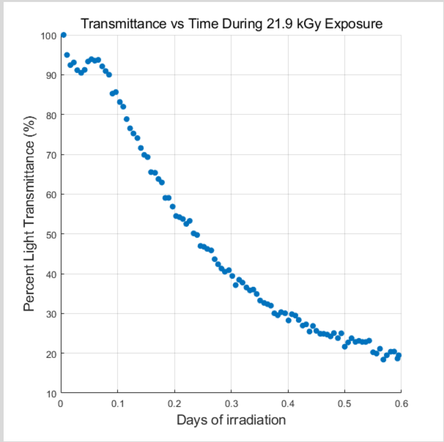

Fig. 4: Transmittance of light through the damaged fiber as a percentage of the peak value versus time (measured in days).

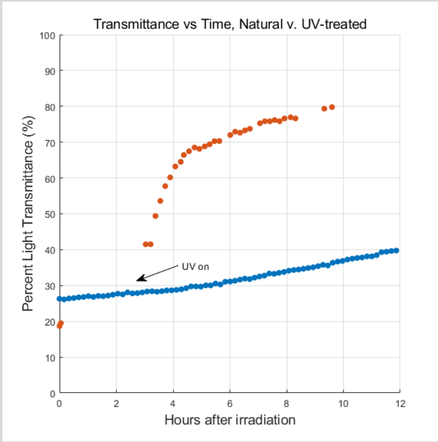

Fig. 5: Transmittance of light through the UV-treated fiber as a percentage of the peak value versus time (measured in hours), shown plotted in orange against the first / untreated fiber.

Miscellany

1. Baseline pre-irradiation versus immediately post-irradiation spectrum graphs of the first fiber.
2. A diagram of the inner workings of a high-energy calorimeter, in this case the CMS at CERN.
3. Second fiber spectrum during irradiation, with gamma radiation spikes.

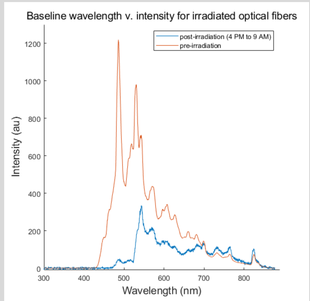

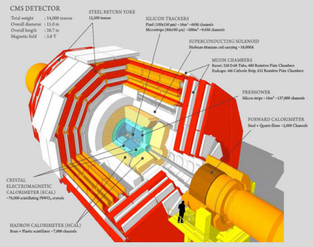

Calorimeter diagram sourced from the CMS detector group at CERN's Large Hadron Collider,

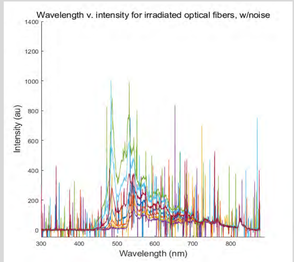

Acknowledgements

I'd like to thank my mentor, Dr. James Wetzel, and the rest of the HEP group at the University of Iowa for guiding me in my research – as well as SSTP and my parents for allowing me to reach this opportunity in the first place.

A Serious Game for Flood Mitigation: Automated Level Generation

Anthony Maggio 1, Yusuf Sermet 2, Ibrahim Demir 2

Basis Independent Silicon Valley 1, IIHR 2

Background

- Flood simulations have long been a concern to both conduct studies and raise awareness for such studies on open sourced sites. Though it had been conducted before, this study seeks to create a simulator in a online video game format that would semirealistically demonstrate a terrain on the bank of a river during the time of a flood.
- It is shown that such studies is able to raise awareness among individuals not previously acquainted with the topic, as show by a study conducted on students. (Felicio et al., 2014).
- A previous system called Stop Disasters was an inspiration for the design of the game, though with several modifications (Blasko-Drabik et al., 2013).
- The program is created mainly with JavaScript with HTML. The JavaScript reads from the Google Maps API and is central to most of the programming involved in the designing of this game.
- The project is divided into two sections, one section for autogenerating a level of the player's choice and another for laying out the graphics of the level per information from the first section. This study seeks to complete the former.

Method

- The generation of levels requires the program to read the pixels of the map and generate a corresponding map. The process of generating a map is beyond the scope of this presentation.
- The program generates on click a region on the map that can be manipulated by the player to conform with the player's desired playing field. The player selects the desired region allows the program to analyse the region. This is done by converting the Google Maps into a static image suing the Google Maps Static API. The program removes labels and minor roads to allow for ease of analysis.
- The program divides each pixel into a rgba (Red-Green-Blue-alpha) value and identifies it as a type of terrain since the map already colors it. These can then be processed by the game and generated into a level. The division into terrain types is precise since for most of Google Maps similar types of constructions (i.e. buildings, roads, etc.) are marked with similar colours, though there are exceptions.
- The terrain types can then be mapped to a tiling system and tiled into a game level. That is the main involvement of the second section and is beyond the scope of the first.

Examples

(Bottom Center) The program analyses the pixels of the image and maps them to an array defining the terrain types. It then returns the rgba values of a pixel and the terrain type it maps to. Since in Google Maps with labels removed separate terrains are indicated with colour, it becomes possible to identify them this way. The result is show in the demonstration designated by the arrow.

(Center & Right) The selection of a Google static image on the map and the analysis of the pixels as demonstrated in the code above are shown. The selecting section is draggable and editable by mouse movements and is therefore flexible. The selection also results in the program analysing the pixels of the static image and identifying the type of block represented by the pixels, as show.

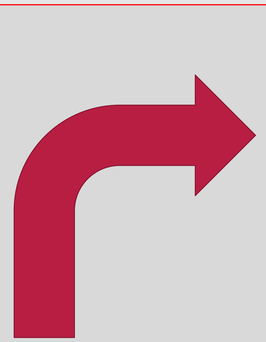

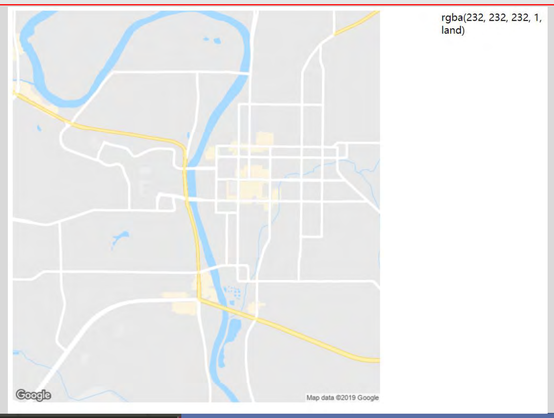

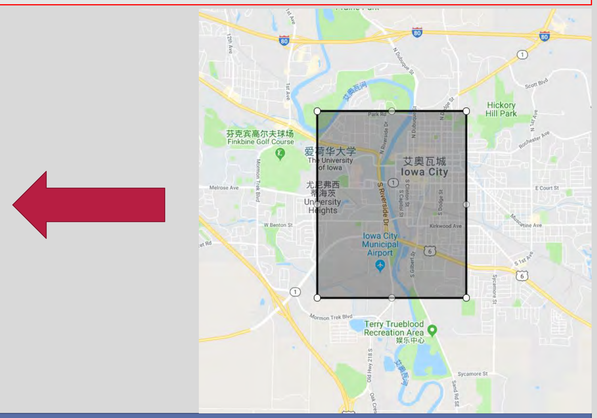


```
function pick(event, type) {
  var x = event.layerX;
  var y = event.layerY;
  var terrain = ["water", "building slot", "pavement", "
    land", "nothing"];
  var pixel = ctx.getImageData(x, y, 1, 1);
  var data = pixel.data;
  if (data[0] == 170 && data[1] == 218 && data[2] == 255)
     {
    type = terrain[0];
  } else if (data[0] == 238 && data[1] == 238 && data[2]
    == 238 || data[0] == 254 && data[1] == 247 && data[2]
     == 238) {
    type = terrain[1];
  } else if (data[0] == 255 && data[1] == 255 && data[2]
    == 255 || data[0] == 255 && data[1] == 242 && data[2]
     == 175) {
    type = terrain[2];
  } else if (data[0] == 0 && data[1] == 0 && data[2] == 0
    ) {
    type = terrain[4];
  } else {
    type = terrain[3];
  }
  var rgba = 'rgba(' + data[0] + ', ' + data[1] + ', ' +
    data[2] + ', ' + (data[3] / 255) + ', ' + type + ')';
  color.style.background =  rgba;
  color.textContent = rgba;
}
canvas.addEventListener('mousemove', pick);
```

Further Developments

- The two sections of the game remain to be integrated in order to form a complete simulation.
- Many aspects of the game remain incomplete and require modification in order to make it sufficiently realistic. Several other serious games have already become sophisticated enough such that they are realistic on a 3D scale (Khoury, et al., 2018).
- Details regarding the workings of a disaster remain to be implemented.
- The program has inaccuracies with mapping since there are exceptions to colouring on Google Maps with some of the pixels marked with unusual rgba values between an ordinary value that can be identified and a generic tile.

Sources

- Felicio, S.P.A.S., Silva, V.S.R., Dargains, A.R., et al., 2014, Stop Disasters Game Experiment with Elementary School Students in Rio de Janeiro: Building Safety Culture, Proceedings of the 11th International ISCRAM Conference.
- Blasko-Drabik, H., Blasko, D., Lum, H., et al., 2013, Investigating the Impact of Self-Efficacy in Learning Disaster Strategies in an On-Line Serious Game, Proceedings of the Human Factors and Ergonomics Society 57th Annual Meeting.
- Khoury, M., Gibson, M., Savic, D., et al., 2018, A Serious Game Designed to Explore and Understand the Complexities of Flood Mitigation Options in Urban–Rural Catchments, Water.

Development of probe to detect and identify damage by reactive neurotransmitter metabolites

Mia Moon[1], Brianna Cagle[2], Rachel A. Crawford[2], Jonathan A. Doorn, PhD[2]

[1]Bergen County Academies, Hackensack, NJ; [2]Department of Pharmaceutical Sciences and Experimental Therapeutics, University of Iowa, Iowa City, IA

BACKGROUND

3,4-dihydroxyphenylacetaldehyde (DOPAL) in Parkinson's Disease (PD)

In the brain, the neurotransmitter dopamine (DA) undergoes enzyme-mediated oxidation to produce a toxic metabolite called **3,4-dihydroxyphenylacetaldehyde (DOPAL).**[1]

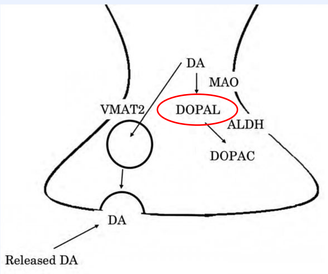

Figure 1. Pathway of dopamine uptake and metabolism in a neuron. Dopamine can spontaneously or enzymatically (via monoamine oxidase) be oxidized to produce DOPAL. (Cagle, Simonsen, Lehmler, & Doorn, 2018).[2]

The "catecholaldehyde hypothesis," suggests that DOPAL has shown to play a role in the pathogenesis of Parkinson's Disease (PD) by damaging dopaminergic neurons through several toxic mechanisms:

- auto-oxidizes to form quinones that stimulate production of reactive oxygen species.
- lipid peroxidation of cell, vesicular, and mitochondrial membranes.
- stimulates alpha-synuclein protein to bind to tropomyosin receptor kinase B, which interferes with neurotrophic activities.
- **binds covalently with proteins through a Michael addition and alter the functionalities of enzymes and transporters.**[3]

OBJECTIVE

Main objectives:

- to detect and/or identify the protein targets of DOPAL.
- generate a method to investigate the proteins damaged by a reactive metabolite of dopamine that is thought to contribute to PD.

It is hypothesized that DOPAL will bind to bovine serum albumin in the control experiment as well as certain proteins in the N27 cell lysate via Michael addition mechanism.

METHODS

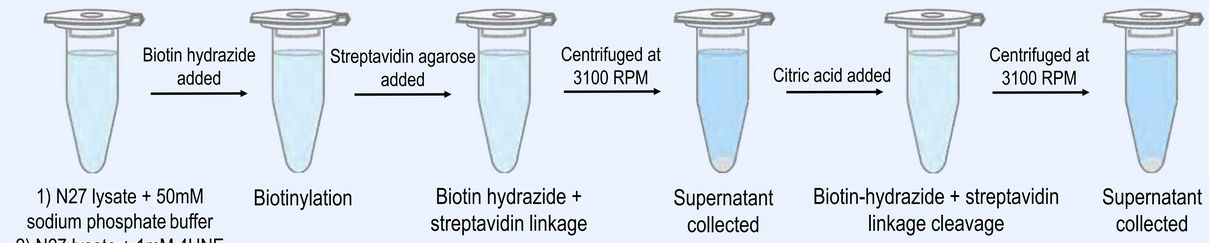

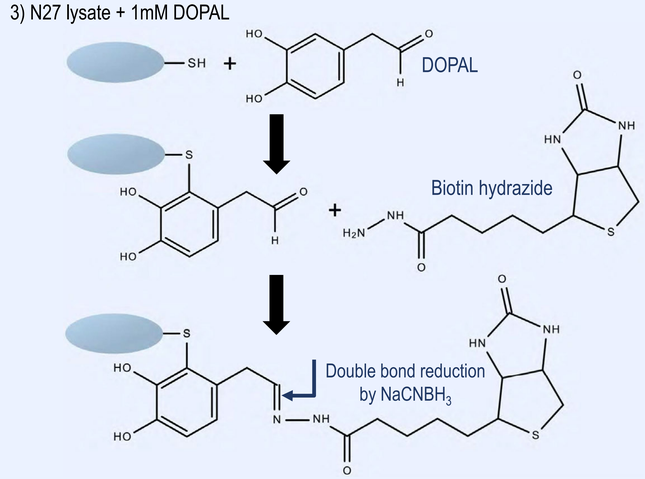

Figure 3. Biotinylation of protein reactive aldehydes with biotin hydrazide. DOPAL binds to proteins via Schiff base or Michael addition, and the aldehyde attaches to a hydrazide bound to a biotin. Sodium cyanoborohydride reduces double bonds. (Modified from Codreanu, 2012).[4]

Figure 2. Probe method to detect modified proteins by DOPAL. Biotin and streptavidin have a strong linkage that can be used to extract proteins modified by 4HNE and DOPAL. 4HNE is byproduct aldehyde of lipid peroxidation and was used as a positive control while the 50mM sodium phosphate buffer was used as a negative control.

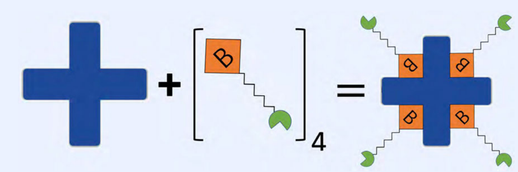

Figure 4. Biotin hydrazide and streptavidin linkage. Up to four biotin hydrazide molecules bound to a modified protein can link with one streptavidin molecule. (Modified from ThermoFisher).

Bicinchoninic acid (BCA) assay and SDS-PAGE were used to determine protein concentration or identification.

RESULTS

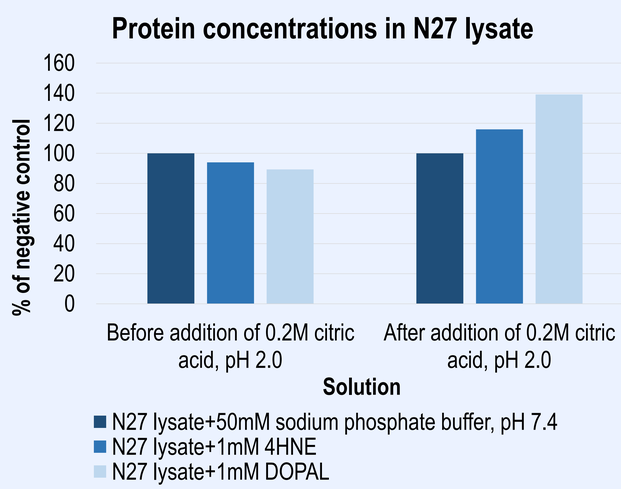

Figure 5. Concentrations of N27 lysate proteins with 50mM sodium phosphate buffer, 1mM 4HNE, and 1mM DOPAL from BCA assay. Concentrations of protein were taken from the supernatants before and after citric acid addition.

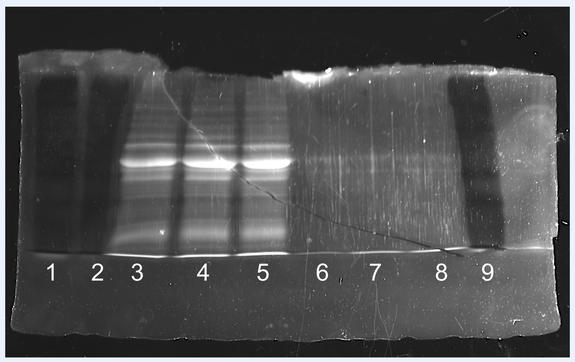

Figure 6. SDS-PAGE image of N27 lysate protein samples with 50mM sodium phosphate buffer, 1mM 4HNE, and 1mM DOPAL. Samples were run through a 10% gel and stained with SYPRO Ruby to visualize proteins in the N27 lysate. Lanes 1, 2, 9: Molecular weight size markers; lane 3, 4, 5: N27 lysate+50mM sodium phosphate buffer (pH 7.4), 4HNE, and DOPAL before citric acid, respectively; lane 6, 7, 8: N27 lysate+ 50mM sodium phosphate buffer (pH 7.4), 4HNE, and DOPAL with citric acid, respectively.

CONCLUSION

The concentration of N27 lysate protein with DOPAL was higher than that with sodium phosphate buffer, which indicates protein modification activity by DOPAL. However, the SDS-PAGE analysis shows that there were no notable differences among the three samples before the addition of citric acid. Moreover, samples with citric acid were not visible. Further experimentation is needed to validate the hypothesized Michael addition by DOPAL.

FUTURE DIRECTIONS

- Repeat initial experiments to confirm validity of results.
- Visualize N27 lysate after addition of citric acid on SDS-PAGE.
- Identify DOPAL protein targets using a proteomics-based approach with the Agilent 1290 series HPLC interfaced with an Agilent 6530 QTOF mass spectrometer.
- Develop research for PD therapeutics related to protein targets of DOPAL.

REFERENCES

1. Cagle, B. S., Simonsen, D. W., Lehmler, H. J., & Doorn, J.A. (2018). Role of 3,4-dihydroxyphenylacetaldehyde in pesticide neurotoxicity. *Society of Toxicology*.

2. Cagle, B. S., Crawford, R. A., & Doorn, J. A. (2019). Biogenic aldehyde-mediated mechanisms of toxicity in neurodegenerative disease. *Current Opinion in Toxicology*, *13*, 16-21. https://doi.org/10.1016/j.cotox.2018.12.002

3. Goldstein, D. S., Kopin, I. J., & Sharabi, Y. (2014). Catecholamine autotoxicity. Implications for pharmacology and therapeutics of Parkinson disease and related disorders. *Pharmacology & therapeutics*, *144*(3), 268–282. https://doi.org/10.1016/j.pharmthera.2014.06.006

4. Codreanu, S. G., Kim, H. Y., Porter, N. A., & Liebler, D. C. (2012). Biotinylated probes for the analysis of protein modification by electrophiles. *Methods in molecular biology (Clifton, N.J.)*, *803*, 77–95. doi:10.1007/978-1-61779-364-6_7

ACKNOWLEDGEMENTS

Special thanks to Dr. Jonathan A. Doorn, Brianna S. Cagle, Rachel A. Crawford, Kate R. Bowman, the Secondary Student Training Program, and the Belin-Blank Center for their help in making this project possible.

Examining an iterative development of reward functions to generate autonomous driving models using reinforcement learning

Sashrika Pandey, Denise Szecsei, Ph.D.

Irvington High School; Department of Computer Science, The University of Iowa

Introduction

- **Machine learning** is the training of a model on data sets before it is used on a test data set to generate a predicted result
- **Reinforcement learning** uses a reward function to encourage certain behaviors
  - If a model adheres to the coded guidelines, then new models can be built off of it to explore other behaviors (Qiang & Zhongli, 2011, p. 1143)
  - Pre-training a model can decrease training time by reducing the initial learning curve (Kim, Cha, Ryu, & Jo, 2019, p. 2)
  - Using past data and trends is practical for the processing of large amounts of signals (Moon, Cheong, Yeom, & Woo, 2019, p. 345)

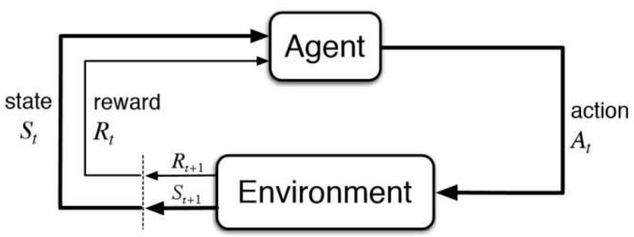

Figure 1. The stages of reinforcement learning
Image Credit: https://www.kdnuggets.com/2018/03/5-things-reinforcement-learning.html

- **Amazon Web Services' DeepRacer**
  - Virtual car undergoes training for user-inputted time and then evaluation

Figure 2. Deep Racer car
Image Credit: https://aws.amazon.com/deepracer/

Figure 3. Track visualization
Image Credit: https://aws.amazon.com/deepracer/

Research Objectives

- Determining an optimal combination of parameters and their respective rewards in the model
- Building off of previous models to determine how past iterations can influence future performance
- Observe applicability of model on track segments

Methods

Strategies

1. **Track curvature**
   - Relative Distance

     $d = \frac{|w_1 w_3|}{|w_1 w_2| + |w_2 w_3|}$
   - Bezier Curves

     $K = \frac{|x'y'' - x''y'|}{((x')^2 + (y')^2)^{3/2}}$
   - Vector Calculations

     $cos\theta = \frac{<u,v>}{||u|| \cdot ||v||}$
2. **Progress per step**
3. **Speed**

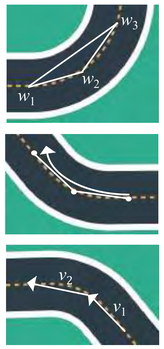

Figure 4. Curvature representations

Development Cycle

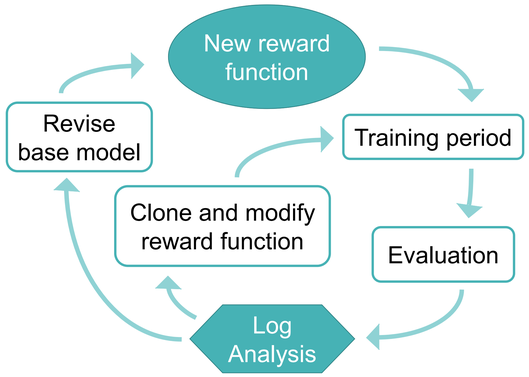

Figure 5. Model development cycle

Results

Figure 6. Distribution of times for evaluation laps in various model series

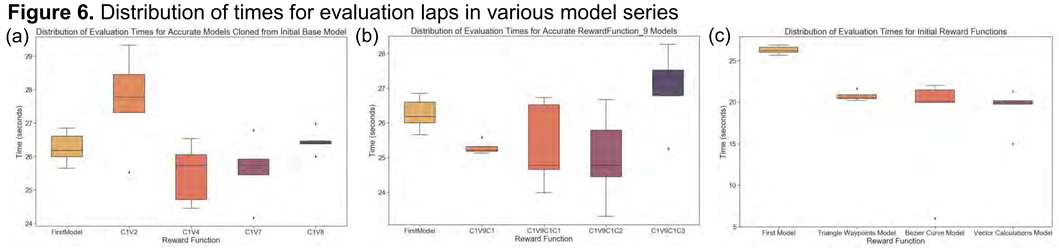

Figure 7. Track paths taken by virtual car during training period for various initial reward functions

(a) Initial Model (b) Relative Distance (c) Bezier Curves (d) Vector Calculations

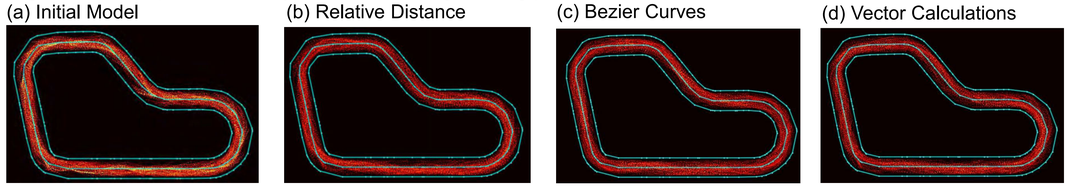

Figure 8. Representation of path taken for an evaluation lap for various initial reward functions

(a) Initial Model (b) Relative Distance (c) Bezier Curves (d) Vector Calculations

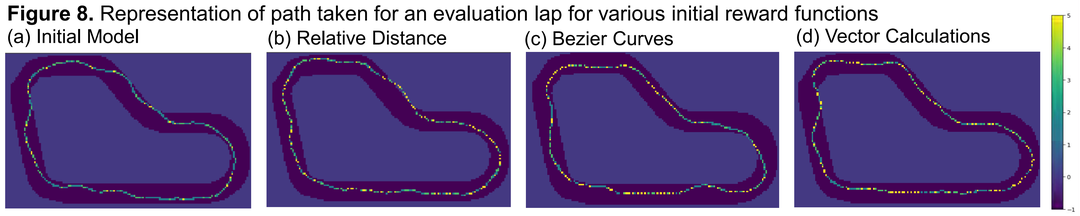

Figure 9. Cumulative rewards for initial reward functions during training period

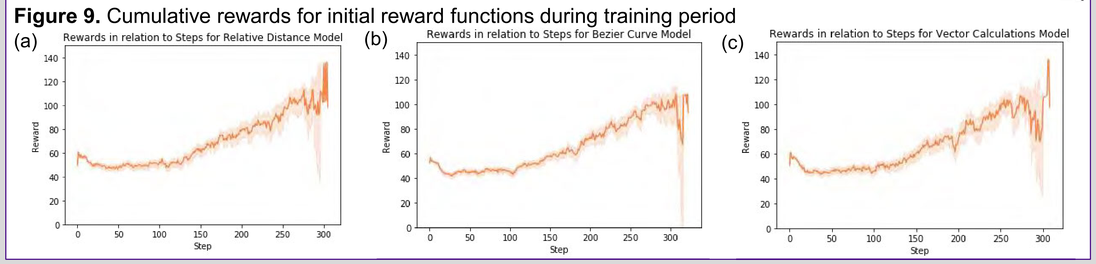

Conclusion

- **Vector calculations** for curvature yielded the fastest and most accurate performance
- Rewarding progress relative to steps was effective
- Models developed as **newly initialized reward functions** performed better than corresponding cloned models
- Successive iterations of reward functions did not always produce improved models

Future Directions

- Build off of successful models to optimize car path and speed in both virtual and physical Deep Racer
- Explore the use of iterative learning models in navigation based solely on sensor input
- Apply reinforcement learning reward functions to situations where certain behaviors are favored

Figure 10. Deep Racer on a physical track

Figure 11. Interior components of the car

DeepRacer GitHub repository

Acknowledgements

Thank you to my mentor Dr. Denise Szecsei, the Belin-Blank Honors Center, and SSTP for this opportunity. An additional thanks to the University of Iowa's Computer Science Department, the Information Technology Services, and the AWS DeepRacer team for their assistance throughout this project.

References

Kim, J., Cha, S., Ryu, M. & Jo, M. (2019). Pre-training framework for improving learning speed of reinforcement learning based autonomous vehicles. *2019 International Conference on Electronics, Information, and Communication (ICEIC)*, Auckland, New Zealand, 1-2. doi: 10.23919/ELINFOCOM.2019.8706441.

Moon, J., Cheong, M., Yeom, I. & Woo, H. (2019). Deep reinforcement learning based sensor data management for vehicles. *2019 International Conference on Information Networking (ICOIN)*, Kuala Lumpur, Malaysia, 345-349. doi: 10.1109/ICOIN.2019.8718108.

Qiang, W. & Zhongli, Z. (2011). Reinforcement learning model, algorithms and its application. *2011 International Conference on Mechatronic Science, Electric Engineering and Computer (MEC)*, Jilin, China, 1143-1146. doi: 10.1109/MEC.2011.6025669.

Downregulation of novel progesterone receptor (PR) repressor genes SETDB1 and HDAC2 restores functional PR expression

Leyi Qiu[1], Vanessa Camp[2], Shujie Yang[3]

[1]Chengdu Shude High School (Foreign Language Campus), [2, 3]The University of Iowa Department of Pathology

Background

- **Endometrial cancer (EC)** is the most common gynecologic malignancy, causing over 11,000 deaths every year.
- **Progesterone** is a key tumor suppressor in endometrial cancer. After binding with **progesterone receptor (PR)**, progesterone can inhibit cell growth, promote apoptosis, and facilitate cell differentiation.
- Existing progestin-based therapy has a low response rate in poorly-differentiated endometrial cancer due to the **loss of PR expression**.
- **HDAC inhibitors (HDACi)** have been shown to effectively restore the expression of PR.
- **HDAC2**, one of the histone deacetylases (HDAC) gene family members that mainly inhibit gene transcription, expresses highest among all the other HDAC family members in all endometrial tumor types.
- **SETDB1,** a gene that encodes histone lysine methyltransferase to silence tumor suppressor gene and cause carcinogenesis, correlates with worst survival of EC patients.

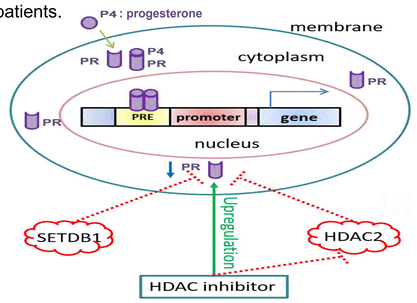

Figure 1. A suggested model of PR expression regulated by SETDB1 and HDAC2 in endometrial cancer. PRE is the progesterone response element which is recognized by the progesterone-activated progesterone receptor. In endometrial cancer cells, PR is downregulated, and HDACi can upregulate PR expression. Our hypothesis is that the HDAC2 and SETDB1 genes are novel PR repressors.

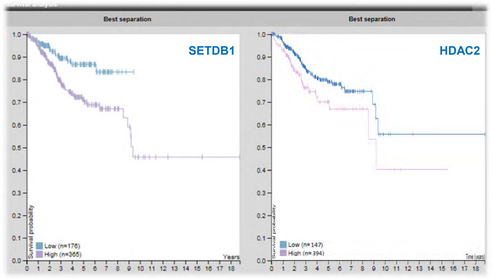

Figure 2. SETDB1 and HDAC2 are unfavorable prognostic markers for endometrial cancer. The statistical results suggest that the highest SETDB1 and HDAC2 expression correlates with the worst survival of EC patients (adapted from the Human Protein Atlas).

Objective

The objective of this study is to investigate the mechanism of PR downregulation. Specifically, we want to confirm that the SETDB1 gene and HDAC2 gene are two novel progesterone receptor repressors.

Methods

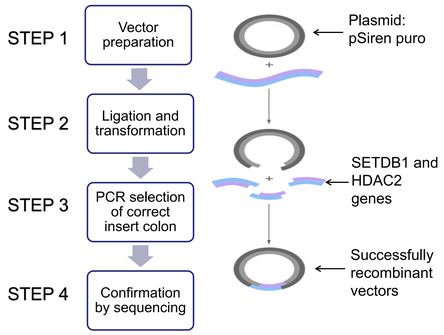

Method 1

STEP 5 in **Gene Knockdown by RNA Interference**

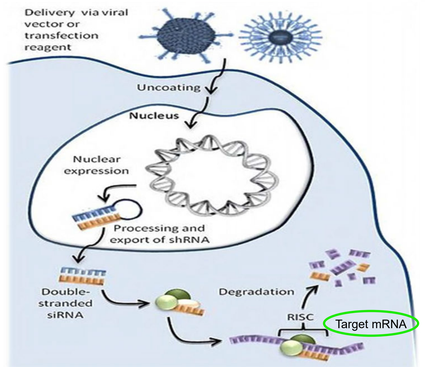

Figure 3. Forming small hairpin RNA (shRNA) in target cells after transduction to degrade target gene. Virus with shRNA for target DNA is transfected into cells, and the shRNA is processed into short interfering RNA (siSNA). One strand of the siRNA duplex is loaded into the endogenous RNA-induced silencing complex (RISC). This guide strand siRNA then localizes RISC to the mRNA of the target genes (SETDB1 and HDAC2). The cleaved mRNA is degraded by other endogenous nucleases.

Method 2

STEP 5 in **Gene Knockout by Crispr Cas 9**

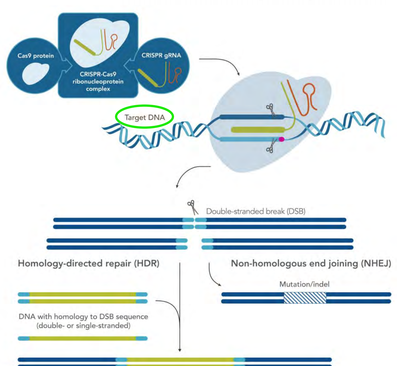

Figure 4. Crispr Cas 9 mechanism. Single guide RNA (sgRNA) with a short "guide" sequence attaches to target sequences of DNA in a genome. The RNA also binds to the Cas9 enzyme which cuts the DNA at the targeted location.

Results

Using Enzyme Digestion to Cut the Vector

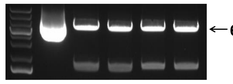

Figure 5. Enzyme digestion of the empty vector. Confirming the size (6.4kb) of vector plasmid pSiren Puro.

Using PCR Amplification to Verify the Inserts

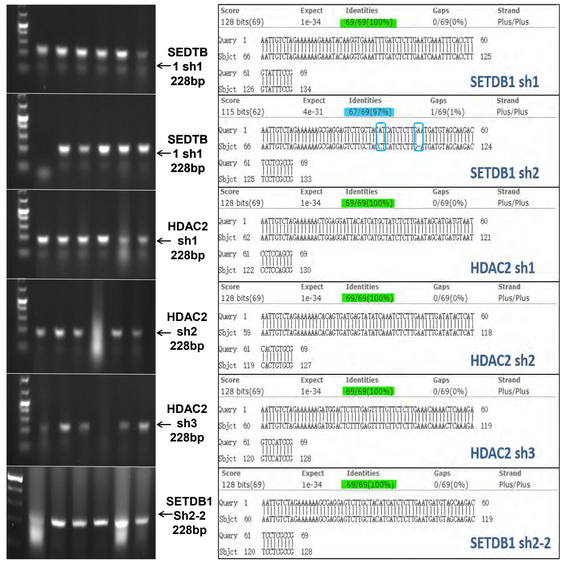

Figure 6.1.(left) Verifying the insert in the plasmid vector using Polymerase-Chain Reaction (PCR). Six colonies from each agar plate were picked out and were applied in PCR to check the correct insert (228 bp). **Figure 6.2.(right) Confirmation of the DNA sequences which target SETDB1 and HDAC2 gene segments by Sanger sequencing.** Basic Local Alignment Tool (BLAST) is used to compare sequencing results. All the inserted sequences matched with the real SETDB1 or HDAC2 gene sequences except SETDB1 sh2. Therefore, we selected 6 more colons from the SETDB1 sh2 plate and sent them to sequencing again. The result matched the SETDB1 sh2 sequence.

HDAC2 knockout Increases Functional PR Expression at Protein Level

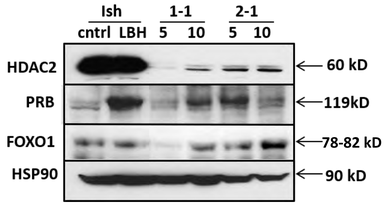

Figure 7. Assessing HDAC2 knockout at the protein level by Western Blot. Knocking out HDAC2 increases PR and its downstream gene FOXO1 expression in Ishikawa cells. These results verify that the downregulation of HDAC2 can upregulate the expression of PR and its downstream gene.

SETDB1 knockout Increases PR Expression at mRNA Level

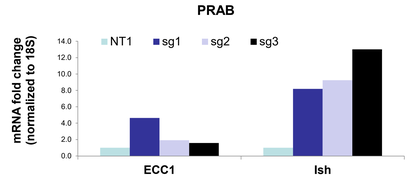

Figure 8. Verification of PR upregulation following by SETDB1 knockout through real time PCR . In both Ishikawa and ECC1 cells, PGRA/B displays an increase in expression after knocking out SETDB1 using 3 pieces of sgRNA.

SETDB1 Knockout Increases Functional PR Expression at Protein Level

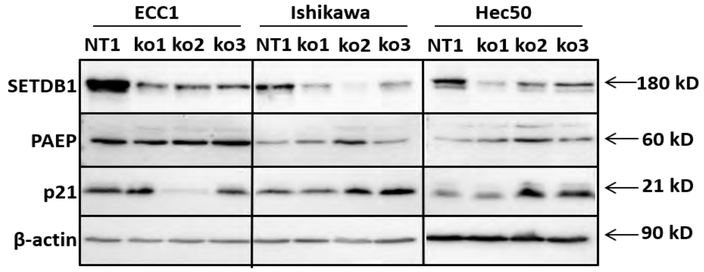

Figure 9. Assessing SETDB1 knockout at the protein level by Western Blot. After knocking out SETDB 1 in ECC1, Ishikawa and Hec50 cells, proteins PAEP and p21 increases. These results verify that downregulated SETDB1 can upregulate the expression of these PR downstream genes.

Conclusion

- Downregulation of HDAC2 and SETDB1 restores functional PR expression
- HDAC2 and SETDB1 are novel PR repressors
- HDAC2 and SETDB1 are potential targets in endometrial cancer

Applications

If the SETDB1 gene is verified to be the bona fide PR suppressor, the drug can be designed to inhibit SETDB1 expression, and therefore, restore normal PR function.

If the HDAC2 gene is proved to be the bona fide PR suppressor, there can be improvement in HDAC inhibitors. Specifically, HDACi can be designed to solely target the HDAC2 gene instead of the whole HDAC family including (from HDAC1 to HDAC11). In that case, several side effects caused by the misfunction of other HDAC genes due to HDACi can be prevented.

Future Directions

- Validation in other cell lines, and study the effect on cell proliferation
- Chromatin immunoprecipitation (ChIP) assay to verify the direct PR repression by SETDB1 and HDAC2
- Transcriptome analysis to study broader effect of SETDB1 and HDAC2 downregulation
- In vivo study

References

Karanth, A. V., Maniswami, R. R., Prashanth, S., Govindaraj, H., Padmavathy, R., Jegatheesan, S. K., . . . Rajagopal, S. (2017). Emerging role of SETDB1 as a therapeutic target. *Expert Opinion on Therapeutic Targets, 21*(3), 319-331. doi:10.1080/14728222.2017.1279604

Ren, J., Zhang, J., Cai, H., Li, Y., Zhang, Y., Zhang, X., . . . Li, J. (2014). HDAC as a Therapeutic Target for Treatment of Endometrial Cancers. *Current Pharmaceutical Design, 20*(11), 1847-1856. doi:10.2174/1381612811319990528

Yang, S., Jia, Y., Liu, X., Winters, C., Wang, X., Zhang, Y., . . . Leslie, KK. (2014). Systematic dissection of the mechanisms underlying progesterone receptor downregulation in endometrial cancer. *Oncotarget,5* (20):9783-97.

Acknowledgements: This research is supported by NIH RO1 CA238274 grant to SY, HCCC-PACT grant to SY, the University of Iowa Department of Pathology Startup and Belin-Blank Center SSTP.

Diversity of a Recently Discovered Gene with Under-Explored Implications on Nitrogen Cycling

Belin-Blank Center, College of Education, The University of Iowa

Rishi Ray[1, 2]; Patrick Richards[1]; Weilun Zhao[1]; Timothy Mattes[1], PE, PhD

[1]Department of Civil and Environmental Engineering, University of Iowa[1]; [2]Barrington High School, Illinois

The University of Iowa

Introduction

- The nitrogen cycle is extremely important in wastewater treatment plants (WWTP)
- Recent literature presents potential presence of nitric oxide dismutase (*nod*) that may exhibit oxygenic activity believed to be impossible in anoxic WWTP conditions[1, 4, 5]
- $2NO \rightarrow N_2 + O_2$ dismutation by methane oxidation coupled with nitrate reduction[3]
- Significant implications for global climate change[2]
- Diversity and abundance of *nod* gene in Iowa wastewater & soil reported in this study

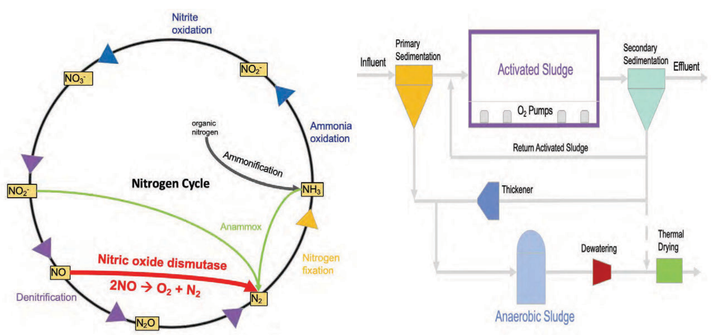

Methods

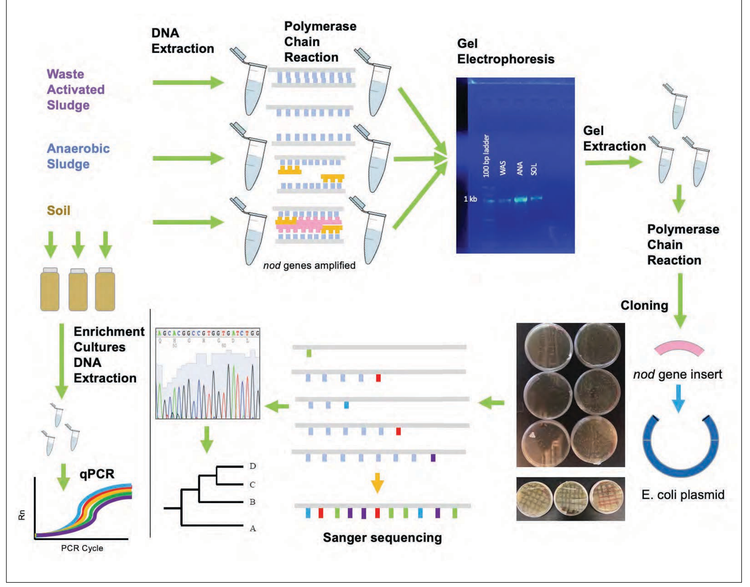

Results

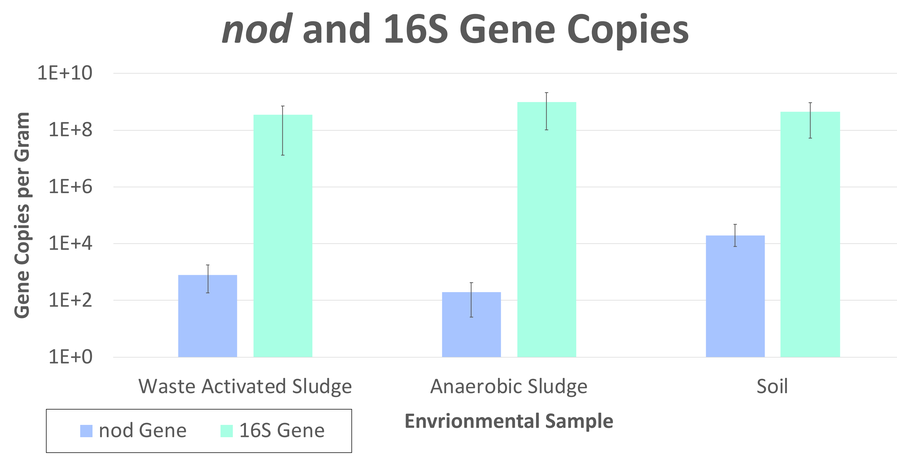

Figure 1: Quantitative PCR analysis of nod gene copies and 16S gene copies. Values determined with averaged data of two extractions from environmental samples. Error bars set at minimum and maximum. Much lower than expected abundance with ≤0.005% nod genes in samples.

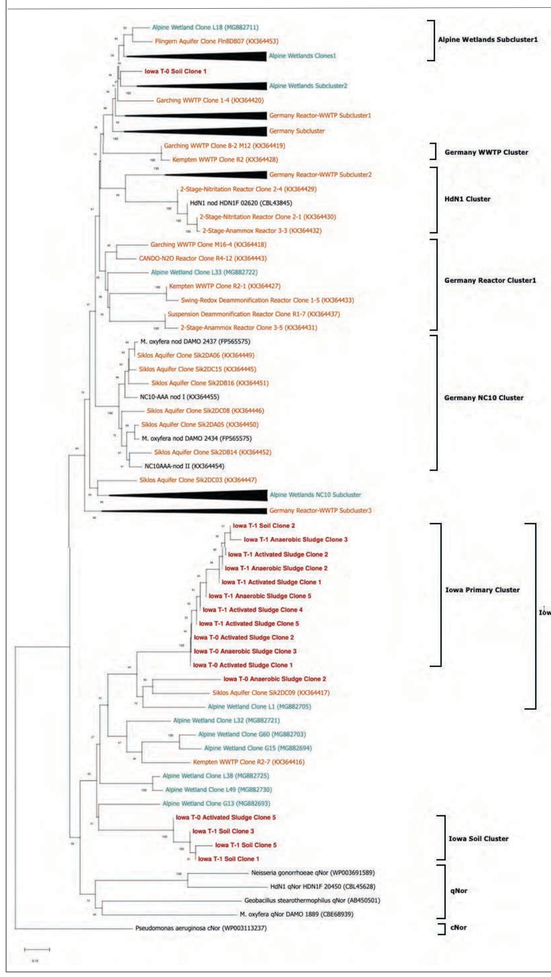

Figure 2: Bootstrapped neighbor-joining phylogeny of putative nod and selected qNor and cNor sequences (1000 replicates). Clones generated in this study are shown in green. Clones generated in China[4] are shown in blue and clones generated in Germany[5] are shown in orange. Reference sequences are shown in black. Compressed branches include highly similar clones. The accession numbers of reference sequences used and of selected sequences are shown in parentheses. Scale bar represents 0.10 base substitutions per site. Two distinct Iowa clusters are represented appear to support presence of nod gene diversity.

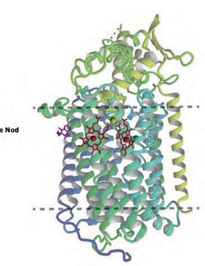

Figure 3: Ribbon representation of qNor structure of G. stearothermophilus[1].

Conclusion

- qPCR data shows evidence of *nod* gene presence in all environmental samples. Unexpectedly low *nod* gene abundance is observed in samples, significantly lower than ~1-2% *nod* gene abundance found in prior literature[5].
- Found two distinct clusters of Iowa *nod* genes indicate some diversity of *nod* genes in Iowa wastewater & soil. Clusters include both wastewater and soil samples, supporting similar *nod* variations to be in both types of samples.
- *nod* variations in different geographic locations tending to cluster most strongly amongst each other suggests *nod* variations tend to differ in distinct global locations.
- Some *nod* variations clustering more closely to distant geographic locations suggests that there are, in fact, nod variations that are present in different locations.

Implications

Determining *nod* abundance and diversity in nitrogen-rich Iowa presents a step toward understanding the impact of *nod* in the nitrogen cycle on the local and global scale. Understanding *nod* will allow scientists and engineers to better develop wastewater treatment processes and potentially contribute to lowering greenhouse gas emissions which dominate the pressing global climate change issue.

Acknowledgements

I am grateful to Mattes Lab for guiding me in conducting my project. I would like to thank Professor Timothy Mattes for giving me the opportunity to work in his lab, Patrick Richards and Weilun Zhao for their guidance and commitment, and Jessica Ewald for her assistance. Thank you to the Belin-Blank Center. This work was supported by NSF Grant 1802583.

References

1. Ettwig, K. F., Speth, D. R., Reimann, J., Wu, M. L., Jetten, M. S. M., & Keltjens, J. T. (2012). Bacterial oxygen production in the dark. *Frontiers in Microbiology*. https://doi.org/10.3389/fmicb.2012.00273
2. Law, Y., Ye, L., Pan, Y., & Yuan, Z. (2012). Nitrous oxide emissions from wastewater treatment processes. Philosophical Transactions of the Royal Society, 1265-1277. https://doi.org/10.1098/rstb.2011.0317
3. Wu, M. L., van Teeseling, M. C. F., Willems, M. J. R., van Donselaar, E. G., Klingl, A., Rachel, R., . . . van Niftrik, L. (2011). Ultrastructure of the denitrifying methanotroph "candidatus methylomirabilis oxyfera," a novel polygon-shaped bacterium. *American Society for Microbiology*. https://doi.org/10.1128/JB.05816-11
4. Zhang, Y., Ma, A., Liu, W., Bai, Z., Zhuang, X., & Zhuang, G. (2018). The occurrence of putative nitric oxide dismutase (nod) in an alpine wetland with a new dominant subcluster and the potential ability for a methane sink. *Hindawi, 2018*. https://doi.org/10.1155/2018/6201541
5. Zhu, B., Bradford, L., Huang, S., Szalay, A., Leix, C., Weissbach, M., . . . Lueders, T. (2016). Unexpected diversity and high abundance of putative nitric oxide dismutase (nod) genes in contaminated aquifers and wastewater treatment systems. *American Society for Microbiology*. https://doi.org/10.1128/AEM.02750-16

Significant association between Dual-Path Platform® CVL assay and Soluble *Leishmania* Antigen ELISA in the diagnosis of canine leishmaniosis

F. Tang[1,2], E.S. Kontowicz[1], B. Scorza[1] and C. Petersen[1]

1 College of Public Health, Center for Emerging Infectious Diseases, Department of Epidemiology, The University of Iowa, Iowa City, IA 52242

2 Walnut High School, Walnut, CA 91789

DPP® CVL assay is an efficient test that can accurately **diagnose canine leishmaniosis**, a potentially **fatal** disease, in the place of gold standard diagnostic tests, such as **SLA ELISA**.

Background

- Approximately 100,000 new cases of visceral leishmaniasis (VL) each year, "fatality rate in developing countries can be as high as 100% within 2 years" (CDC)
  - Caused by *Leishmania donovani* or *Leishmania infantum* (Larson et al., 2018, p. 381)
  - Vectors: phlebotomine sand flies (Ready, 2014, p.148)
- Primary reservoir host: dogs- canine leishmaniosis (CVL)
- Endemic to hunting hounds in the US, passes along through vertical transmission only right now (Boggiatto et al., 2011, p.1)
- Current gold standard diagnostic tests are all lab tests; need field tests that are more convenient and efficient (Srivastava et al., 2010, p.1)
  - Past study has shown correlation between Dual-Path Platform (DPP)® CVL assay and Immunofluorescence Antibody Test, but not between Soluble *Leishmania* Antigen (SLA) Enzyme-linked Immunosorbent Assay (ELISA)
- A past study has shown that LeishTec® (vaccine) helps reduce clinical progression and *leishmania* related mortality (Toepp et al., 2018, p. 6433)

A)

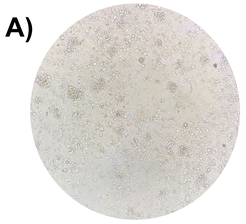

B)

Figure 1:
A) *Leishmania infantum* parasites
B) Female phlebotomine sand fly accessed on 7/10/19 from *CDC*/Frank Hadley Collins
https://www.vettimes.co.uk/news/vets-in-uk-need-to-know-about-leishmaniasis/

Study Question

- What is the relationship between the leishmaniasis diagnostic results of the DPP® CVL assay and SLA ELISA?

Hypothesis

- There is a significant association between DPP® CVL assay and SLA ELISA results.

A)

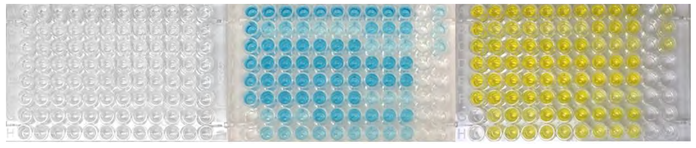

B)

Figure 2: A) Basic steps of ELISA and B) Unused DPP® assay (left) and positive reading on a DPP® assay (right)

Methods

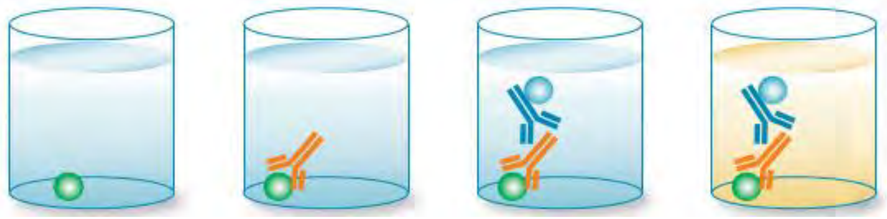

1. Prepare antigen (2ug/mL) and coat wells. Block to prevent non-specific binding.
2. Add sample serums (1:500 dilution).
3. Add secondary antibody: rabbit anti-dog antibody. TMB substrate turns contents blue.
4. Stop reaction with H_2SO_4 acid. Read plate with Omega software.

Figure 3: Contents of a plate well throughout indirect SLA ELISA
Accessed on 7/12/19 from *Bio-Rad*
https://www.bio-rad-antibodies.com/elisa-types-direct-indirect-sandwich-competition-elisa-formats.html

Results

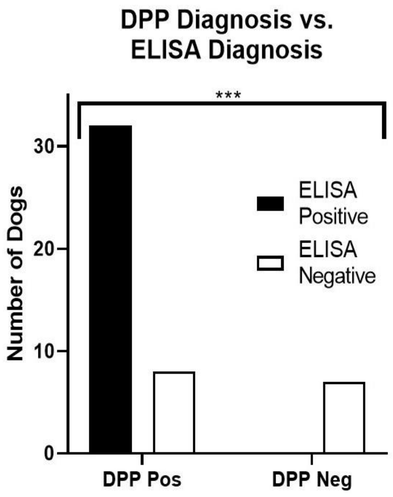

Figure 4: Significant correlation between DPP® and SLA ELISA diagnostic results. Fisher's Exact Test determined there was a significant relationship between DPP® diagnosis and ELISA diagnosis (***: p = 0.0001). It was found that DPP® had a sensitivity of 80% and specificity of 100%.

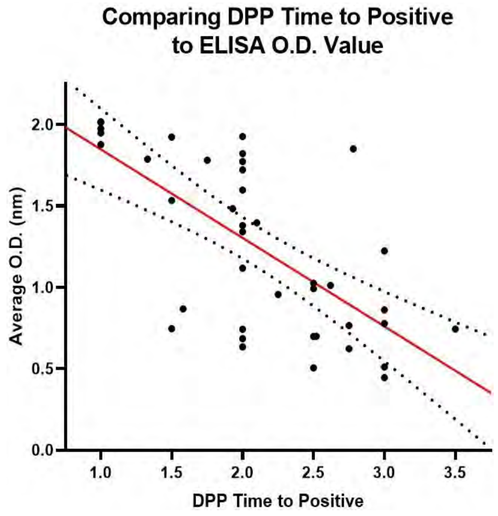

Figure 5: Significant correlation between ELISA optical density (O.D.) values and time to positive for DPP® test in our positive dogs. Ordinary Linear regression found a significant relationship between ELISA O.D. values and DPP® time to positive (r^2 = 0.4569, p = 1.695 * $^{10-6}$)

Results cont.

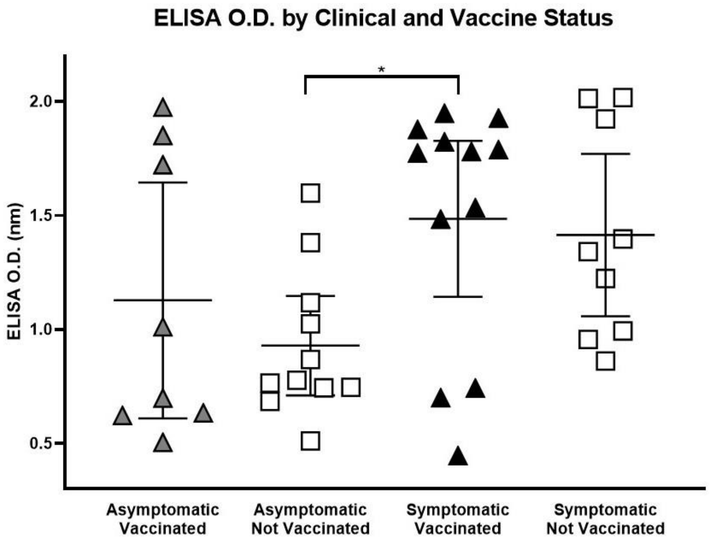

Figure 6: Significant ELISA O.D. difference between symptomatic, vaccinated dogs and asymptomatic, not vaccinated dogs. Ordinary One-Way ANOVA with Tukey's multiple comparisons test showed only one significant difference (*: p = 0.0469) in mean values between symptomatic, vaccinated dogs and asymptomatic, not vaccinated dogs.

Conclusion and Future Directions

- DPP® CVL assay is a reliable and valid diagnostic test that can be used on the field
- There is a significant increase in average O.D. as DPP® time to positive decreases
- Vaccinated, symptomatic dogs have more robust immune response, that is likely due to vaccine effects, when compared to asymptomatic, not vaccinated dogs
- Future studies can include:
  - Comparing ELISA O.D. values to DPP® Micro Reader values
  - Testing outside of the hunting dog population

References

Boggiatto, P. M., Gibson-Corley, K. N., Metz, K., Gallup, J. M., Hostetter, J. M., Mullin, K., & Petersen, C. A. (2011). Transplacental transmission of Leishmania infantum as a means for continued disease incidence in North America. *PLoS Neglected Tropical Diseases, 4,* e1019.

CDC - Leishmaniasis. (n.d.). Retrieved from https://www.cdc.gov/parasites/leishmaniasis/

Larson, M., Toepp, A., Scott, B., Kurtz, M., Fowler, H., Esfandiari, J., . . . Petersen, C. (2016). Semi-quantitative measurement of asymptomatic L. infantum infection and symptomatic visceral leishmaniasis in dogs using Dual-Path Platform® CVL. *Applied Microbiology and Biotechnology, 1,* 381–390.

Ready P. D. (2014). Epidemiology of visceral leishmaniasis. *Clinical Epidemiology*, *6*, 147–154. doi:10.2147/CLEP.S44267

Srivastava, P., Dayama, A., Mehrotra, S., & Sundar, S. (2010). Diagnosis of visceral leishmaniasis. *Transactions of the Royal Society of Tropical Medicine and Hygiene, 1,* 1–6.

Toepp, A., Larson, M., Wilson, G., Grinnage-Pulley, T., Bennett, C., Leal-Lima, . . .Petersen, C. (2018). Randomized, controlled, double-blinded field trial to assess *Leishmania* vaccine effectiveness as immunotherapy for canine leishmaniosis. *Vaccine, 43,* 6433–6441.

Acknowledgements

I would like to thank the Petersen Lab, Belin-Blank Center, and the University of Iowa for providing such an amazing opportunity to aspiring researchers.

Learning From Profanity – Offensive Speech Detection via Transfer Learning

Xintong Yu[1,2]; Ingroj Shrestha, PhD[2]; Jonathan Rusert, PhD[2]; Padmini Srinivasan, PhD[2]
[1]Phillips Exeter Academy, [2]University of Iowa

Introduction

- Increasing propagation of offensive speech on social media.
- Significant investment from governments, companies, and researchers to regulate this phenomenon.
- While censorship curtails freedom of speech, unregulated offensive speech provokes hate crime and eventually jeopardizes a platform's utility.

Offensive Speech

Personal attacks or degrades to another user. Offensive speech contains terms with recent or historical meaning relating to a particular gender, race, sexual orientation, or other characteristic of a user or group of users.

Related Work

- Popular classifiers include deep learning models such as CNNs, RNNS ,as well as ensemble models.
- In the 2019 OffensEval (Zampieri, et al., 2019) task, the pretrained BERT model (Devlin, Chang, Lee, & Toutanova, 2018) achieves promising performance.
- However, the performance of the above models relies on enormous amount of task-specific training data , which poses a challenge since it is costly and time-consuming to create such datasets. We tackle this problem by transfer learning.
- Transfer Learning applies classification knowledge learned from a previous domain to a new domain (Pan et al.,2010).

Our contribution

- We present a new transfer learning model that extracts features from another external text corpora to monitor offensive tweets.
- We demonstrate that the new approach is able to consistently improve the F-1 score of baseline models by approximately 5.39%.

Objectives

- Implement a variety of deep learning models as baselines, including the latest Google BERT model.
- Investigate the efficacy of transfer learning architectures and compare their performance with baseline models.

Data and Methodology

Data Description

The Offensive Language Identification Dataset (OLID) contains 13400 tweets for training and 860 tweets for test. Tweets are labeled as either Offensive **(OFF)** or Not-Offensive **(NOT)**

- **OFF -** @ USER Just block the idiot. He's not even worth this post.
- **NOT -** @USER You are so sweet and adorable

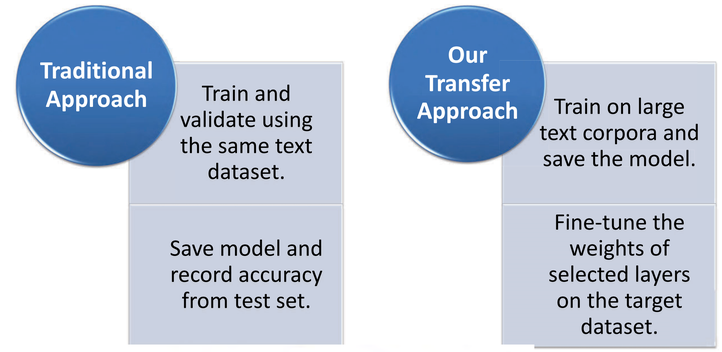

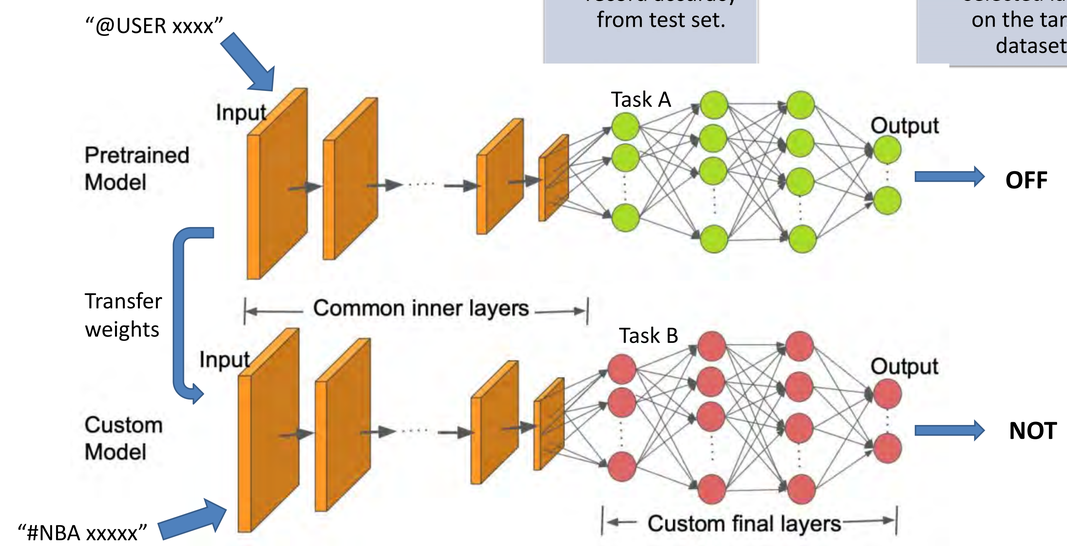

- Baseline models: Logistic Regression, Support Vector Machine(SVM) , CNN, LSTM, BiLSTM, GRU, CNN-LSTM, CNN-GRU, CNN-BiLSTM as well as the fine-tuned BERT model.
- Transfer learning models: Pretrain two sets of models, one on the Kaggle Sentiment Analysis dataset (1.6M tweets) and the other on the Jigsaw Toxicity dataset (153k Wikipedia comments).
- Fine-tune the models on the target dataset using 2 configurations: (1) setting all layers as trainable or (2) setting only the dense layers trainable

Results

- F-1 score = $2\times\frac{Precision \times Recall}{Precision+Recall}$, which penalizes both false positive and false negative results.
- The performance of BERT and the six best performing models are reported below :

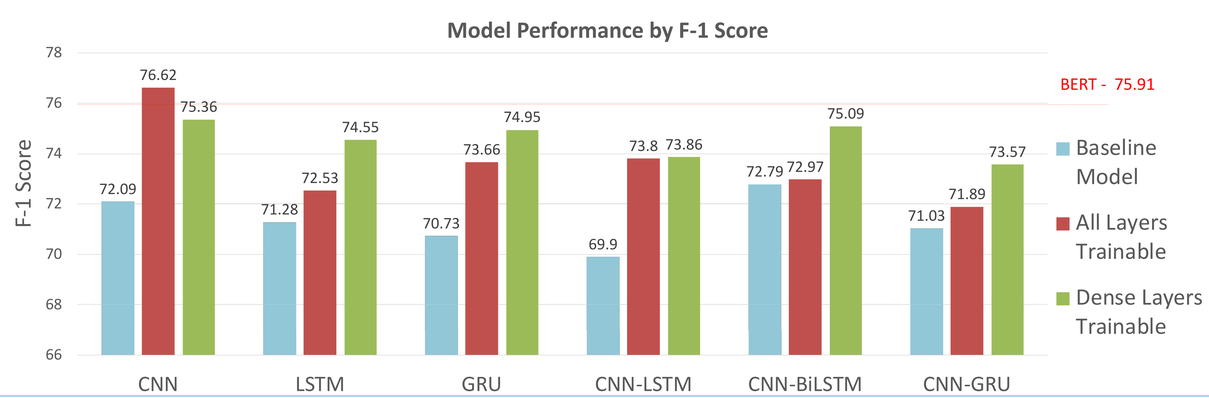

Discussion

- The sentiment analysis dataset, due to the relative shortness of its tweets, does not produce reasonable accuracies and is thus not included in the results.
- For the toxicity dataset, all transferred models consistently outperform their respective baseline by an average of 5.39%.
- Transferred CNN model performs best with all layers trainable while other models involving Recurrent layers achieve higher F – 1 with only dense layers trainable. Intuitively, this is because CNN focuses on filtering keywords specific to each corpus, and RNNs overfit if all weights are fine-tuned.
- Notably, the transferred CNN model outperforms the BERT model by 0.69.

Conclusions & Future Work

We design transfer learning architecture to detect offensive speech in Twitter. The proposed method is able to consistently improve the performance of deep learning models. While CNN performs better with layers all trainable, models with RNN prefer only trainable dense layers. In the future we aim to experiment with other datasets for pretraining and implement more diversified transfer learning architectures.

Acknowledgement

Special thanks to Asad Mahmood, Osama Khalid, and all members of the computer lab for providing the guidance needed to complete this project. Special thanks to Dr. Lori Ihrig and Dr. Duhita Mahatmya for leading the Secondary Student Training Program.

Contact Information

<Xintong Yu>
<Phillips Exeter Academy>
Email : xyu@exeter.edu
Phone : 914-672-2320

References

Devlin, J., Chang, M.-W., Lee, K., & Toutanova, K. (2018). Bert: Pre-training of deep bidirectional transformers for language understanding. *arXiv preprint arXiv:1810.04805*.

Pan, S. J., & Yang, Q. (2009). A survey on transfer learning. *IEEE Transactions on knowledge and data engineering*, 22(10), 1345-1359.Pennington, J., Socher, R., & Manning, C. (2014).

Glove: Global vector for word representation. *Proceeding of the 2014 conference on empirical methods in natural language processing (EMNLP)*, (pp. 1532-1543).

Zampieri, M., Malmasi, S., Nakov, P., Rosenthal, S., Farra, N., & Kumar, R. (2019). Semeval-2019 task 6: Identifying and categorizing offensive language in social media (offenseval). *arXiv preprint arXiv:1903.08983.*

Effects of potassium channel mutations on motoneuron morphology in *Drosophila* giant-neuron cultures

Veda Amalkar[1], Jeffrey Zhang[2], Tristan O'Harrow[3], Cassandra Burke[3], Atulya Iyengar[3], Chun-Fang Wu[3]

[1]Valley High School, [2]Centerville High School, [3]Department of Biology, University of Iowa

INTRODUCTION

- *Drosophila* are used as a model organism for their relatively small genome, short life cycle and ability to reproduce large numbers of offspring.
- Potassium channels play a vital role in neuronal function by restoring the resting potential after an action potential occurs.
- Cytochalasin B (CCB), a cell-permeable mycotoxin, blocks cytokinesis in cells without having an effect on nuclear division. In this experiment, CCB was used to create giant neurons in order to make neuronal growth more evident (Wu 1990).
- *In vitro* cultures are ideal for studying neuronal properties and analyzing altered mechanisms in mutants (Wu 1983).
- This experiment used *ether-a-go-go (eag)* and *Shaker (Sh)* mutants as well as a wild-type control.

RESEARCH OBJECTIVES

The primary objective of this experiment was to determine the changes in motoneuron morphology as an effect of potassium channel mutations in *Drosophila* giant-neuron cultures. Additionally, we observed the role of heat on neuronal growth in the cultures.

METHODS

1 Virgin and egg collection

Virgin females were collected in the mornings while unconscious under CO2 and subsequently kept at room temperature for mating to occur.

2 Culture preparation

Embryos were decoronated and cells were extracted from 4-5 embryos per culture. The cells were then placed into culture medium which consisted of amino acids, glucose, CCB and other components to foster neuron growth.

3 Microscopy and imaging

Pictures were taken over a span of fifteen days under both fluorescence and brightfield. Fluorescent images revealed the motoneurons and brightfield images allowed the neurites to be captured more clearly.

4 Analysis of neuronal growth

After pictures of the cultures were taken, neurons were counted and categorized based on polarity. Additionally, terminal complexity of neurons was assessed. Finally, neuronal growth from cultures of different temperatures was compared.

wild-type | *eag*^{4PM} (Kv10) | *eag*^{1} (Kv10) | *Sh*^{M} (Kv1) | *Sh*^{120} (Kv1)

- Cultures of all five genotypes were kept in both room temperature and high temperature (29°C) environments
- All genotypes had C164-GCaMP (Gal4-UAS system), a genetically encoded fluorescent calcium indicator, to drive fluorescence in motor neurons

RESULTS

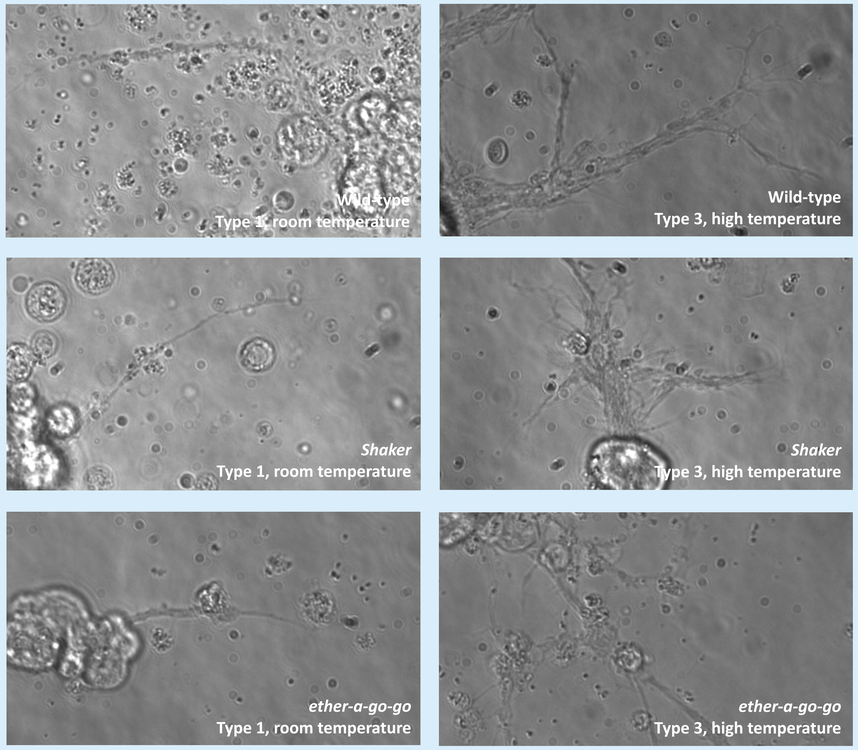

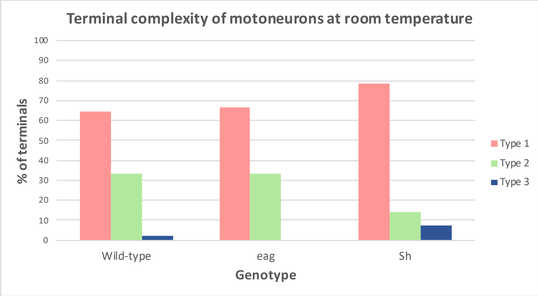

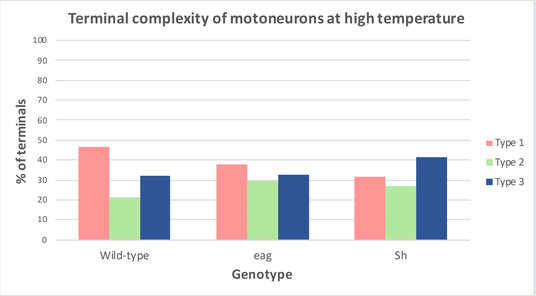

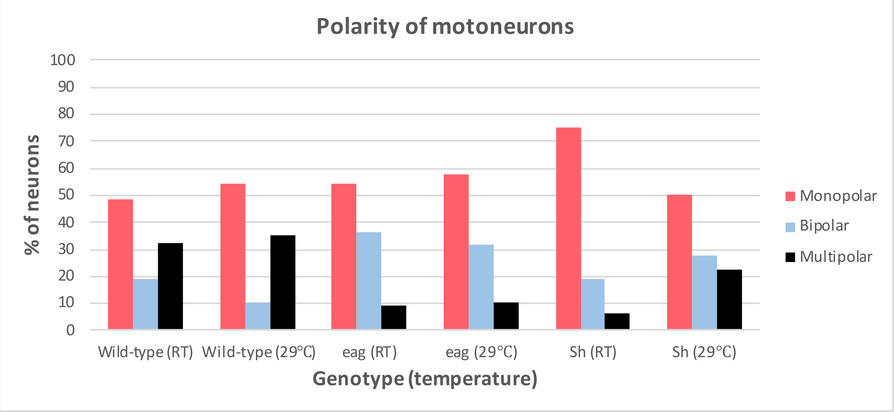

Polarity

Monopolar

Neurons with one distinct neurite stemming from the cell body

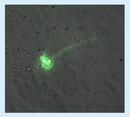

Bipolar

Neurons with two distinct neurites stemming from the cell body

Multipolar

Neurons with three or more neurites stemming from the cell body

Terminal complexity

Type 1

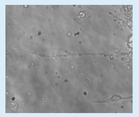

Type 2

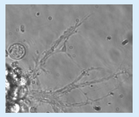

Type 3

Based on level of complexity, we classified terminals into three types

CONCLUSIONS

- Motor neurons with mutations do not display higher terminal complexity.
- **Terminal complexity**
  - Higher temperatures increase terminal complexity of neurons regardless of genotype.
  - Similar growth of the three terminal branch types was observed in all genotypes at room temperature.
    - Predominantly Type 1, followed by Type 2 and Type 3 respectively.
- **Polarity**
  - Temperature change had a more drastic effect on *Shaker* neurons than wild type and *eag*.
  - Proportions of monopolar, bipolar and multipolar neurons in *eag* and *Shaker* neurons were similar.
  - There was a significant genotype effect on polarity between the mutant and wild-type cultures.

IMPLICATIONS and FUTURE DIRECTIONS

- Epilepsy, a common neurological disorder, occurs when potassium channels fail to repolarize the neurons and cause repeated firing of signals.
- Future work:
  - Breeding flies with different channel mutations together and culturing the neurons

REFERENCES

Benzer, S. (1973). Genetic dissection of behavior. *Scientific American*, *229*(6), 24–37.

Wu, C.-F., Suzuki, N., & Poo, M.-M. (1983). Dissociated neurons from normal and mutant drosophila larval central nervous system in cell culture. *The Journal of Neuroscience*, *3*(9), 1888–1899.

Wu, C.-F., Sakai, K., Saito, M., & Hotta, Y. (1990). Giant drosophila neurons differentiated from cytokinesis-arrested embryonic neuroblasts. *Journal of Neurobiology*, *21*(3), 499–507.

ACKNOWLEDGEMENTS

I would like to express my gratitude to the members of the Wu lab and my peers at SSTP for supporting me throughout these 5 weeks. Thank you to the Belin-Blank Center and the University of Iowa for this amazing opportunity.

The impact of demographic factors on baseline simulated driving performance

Alex Wang[1], Thomas Burt[2], Dawn Marshall[2], Timothy Brown[2]

[1]Saratoga High School, [2]National Advanced Driving Simulator, University of Iowa

Objectives

The study compared the simulator driving performance of drivers of varying demographics.

Specifically, we hypothesized:

- Speed will be higher for males than females.
- Speed will decrease with increasing age.
- Standard deviation of lane position (SDLP) will not be affected by driver sex.
- SDLP will have a parabolic relationship with driver age.

Source: towardsdatascience.com

The study used 10,725 points of female data and 11,197 points of male data with the drivers aged between 16 and 67.

Results

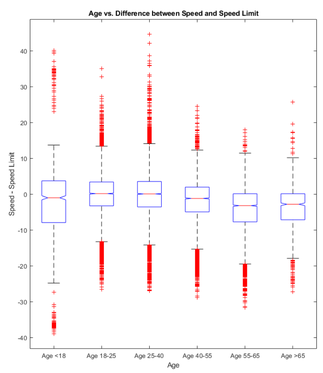

Figure 1: Older drivers tend to drive slower and deviate less from the speed limit.
Linear model for age and speed limit vs. speed: $R^2 = 0.76$ and coefficient of speed = -0.097

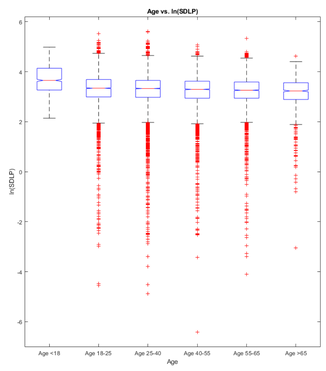

Figure 2: SDLP varies more for younger drivers and appears to decrease across age, but no model was found that accounts for variability of data.

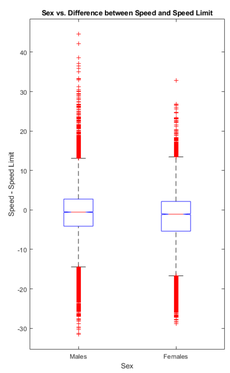

Figure 3: Speed is higher and varies more for males.
t-test: $p < 0.001$ and mean difference = 1.26

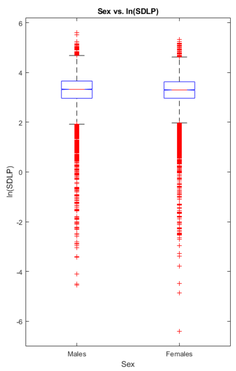

Figure 4: SDLP between sexes is similar.
t-test: $p = 0.12$ and mean difference = 0.016

Conclusions/Implications

The results of this study serve to direct future simulated driving studies in their sampling of drivers. It is imperative to consider teen drivers because they tend to drive differently from the rest of the population.

In terms of sex:

- Both sexes should be included when looking at speed, but unnecessary when looking at SDLP

In terms of age:

- Drivers of all ages should be included when looking at both speed and SDLP.

Future Directions

- Consider other factors on driving performance such as experience and miles driven per year
- Analyze effects on other variables such as standard deviation of speed and lane crossings

Introduction

Influence of Age

- Younger drivers generally underestimate risk factors and overestimate their ability (Borowsky et al., 2010); therefore, they are the age group most at risk for fatal crashes.
- Elderly drivers display greater inconsistency in maintaining headway and lateral position (Bunce et al., 2012) and drive slower when distracted (Horberry et al., 2006).

Influence of Sex

- Younger men were more likely to engage in fatal crashes, but women had a higher risk of nonfatal crashes (Massie et al.,1995).

Methods

Baseline Simulated Driving

We used drive data from NADS-1 and miniSim under normal driving conditions, meaning that there were no external distractions and the driver was not drowsy or under the influence of drugs or alcohol.

Data Analysis Process

Raw data broken into 120-second chunks and reduced in MATLAB → Reduced data collected in a central repository → Microsoft Access to query data for relevant studies and variables → Data imported to MATLAB or plots and statistical tests

Figure 5 (Left): The outside view of the high-fidelity NADS-1 simulator
Figure 6 (Middle): The inside of NADS-1 with a 360-degree panoramic view and a full car chassis
Figure 7 (Right): The miniSim comprised of three desktop monitors
Source: all photos from nads-sc.uiowa.edu

References

Borowsky, A., Shinar, D., & Oron-Gilad, T. (2010). Age, skill, and hazard perception in driving. *Accident Analysis & Prevention*, 42(4), 1240-1249.

Bunce, D., Young, M. S., Blane, A., & Khugputh, P. (2012). Age and inconsistency in driving performance. *Accident Analysis & Prevention*, 49, 293-299.

Horberry, T., Anderson, J., Regan, M. A., Triggs, T. J., & Brown, J. (2006). Driver distraction: The effects of concurrent in-vehicle tasks, road environment complexity and age on driving performance. *Accident Analysis & Prevention*, 38(1), 185-191. doi:https://doi.org/10.1016/j.aap.2005.09.007

Massie, D. L., Campbell, K. L., & Williams, A. F. (1995). Traffic accident involvement rates by driver age and gender. *Accident Analysis & Prevention*, 27(1), 73-87.

Acknowledgements

A special thanks to Dr. Brown, Mx. Marshall, Thomas Burt, Kevin Tang, and all the other staff at the National Advanced Driving Simulator. Thank you to the Belin Blank Center and the University of Iowa for allowing me to attend this amazing opportunity at SSTP.

An analysis of corn stover production with image recognition across an agriculture field

Eddie Wang[1]; December Weir[2]; Caglar Koylu, PhD[1,2], Dr. Mark Linderman, PhD[1,2]
Palo Alto High School[1] - Department of Geographical and Sustainability Sciences, The University of Iowa[2]

Introduction & Background

- Remote sensing is when a sensor, usually a camera, is attached to a drone or satellite to scan the planet, obtaining geographical information about the land.
- Precision agriculture is a type of farming management that utilizes remote sensing to measure variables in crops for decision making.
- In this case, we will focus on the production of corn stover, a fundamental agricultural by-product of corn harvests.
  - We chose corn stover because it was difficult for farmers to know how much material they should extract, thus hindering their ability to maximize their profits.
- In previous studies, people have utilized remote sensing technology to measure pH, organic matter, etc. to identify corn stover.
- Hyperspectral sensors typically measure about 100 to 200 spectral bands of 5-10 nm bandwidths along a continuous electromagnetic spectrum.
- Using their canopy reflectance, we could determine the biophysical properties of the stover.
- This study has two intentions:
  1. Use image processing algorithms to identify corn stover in pictures taken by a handheld camera.
  2. Using remote sensing technology, a specific waveband will be found using hyperspectral cameras that can differentiate corn stover from other materials such as soil.

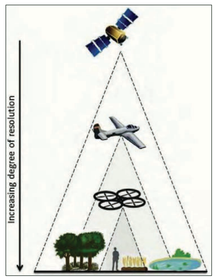

Figure 1. Various remote sensing setups

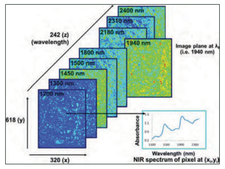

Figure 2. Hyperspectral imaging. Notice the continuous spectrum.

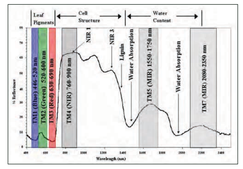

Figure 3. Electromagnetic values of a hyperspectral image.

Research Question & Hypothesis

- Can hyperspectral sensors detect a unique band of frequency among corn stover to determine the impacts on the cover crop yield?

Hypothesis:

- **H_a: Hyperspectral sensors can detect a unique band of frequency in corn stover.**
- **H_0: Hyperspectral sensors cannot detect a unique band of frequency in corn stover.**

Methods and Materials

Remote sensing:

- The remote sensing setup that will be used is a hyperspectral camera attached to a propeller plane.
- Aerial images of field crops will be operated through Parge, ENVI and ArcMap.
  - Parge will process the images through raster pixel data.
  - Wavelength of the pixels will be identified in ENVI.

Image processing:

- 30 randomly 1x1 meter plots of corn stover will be selected at 1879 T Ave South Amana, IA 52334, a corn farm near the University.
- Pictures of the plots will be taken using a handheld camera.
- Using a software called ERDAS Imagine, an algorithm using the RGB values of the selected plots will be derived to identify the presence of corn stover in the pictures.

Figure 4. Hawkeye hyperspectrometer.

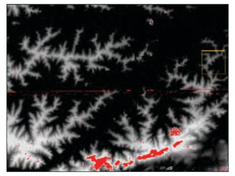

Figure 5. DEM flight plan.

Results

- By using image processing algorithms, we were able to determine a fairly accurate algorithm to identify both corn stover and vegetation by studying and placing restrictions on the RGB values of the photos.
- Algorithms used(simplified syntax for presentational purposes):

Vegetation:

If [Green/(Red+0.1)>1.2] or [Red>Green>Blue and Red+Green+Blue>270]

Stover:

If [Red+Green+Blue>570] and [Red-Green<30] or [Red-Green<15 and Green-Blue<15 and 60<Green<120]

Highlighting vegetation

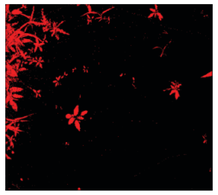

Figure 6. Original image

Highlighting stover

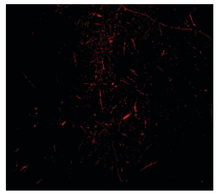

Data

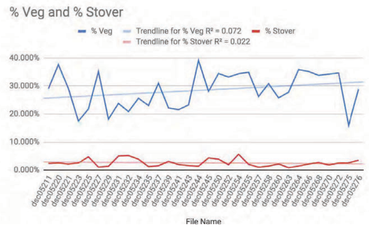

Figure 7 (left). The variance of corn stover and vegetation across the 30 plots. Notice how for both lines, $R^2 < 0.1$

Figure 8 & 9. Reflectance across different wavelengths for stover **(bottom left)** and soil **(bottom right)**

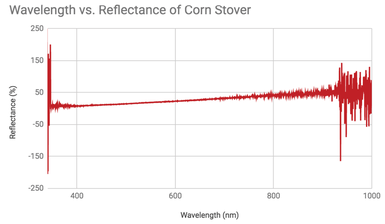

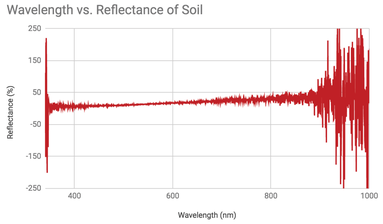

Conclusions

1. Primary data of raw material aerial images were collected from the Hawkeye hyperspectral push broom sensor of an A-series sensor of 400-1000nm and an X-series sensor of 900-1700nm. Soil and stover reflectance were measured using a handheld near infrared spectrometer. Finally, a DEM file of the study site was collected from LiDAR data(see figure 5).
2. The key to the best image processing algorithm happened to be through the use of ratios. This is the solution to the problem with shadows potentially darkening the image, because when shadows shine over corn stover, the RGB values of the image decrease by a uniform and linear amount.
3. Corn stover and soil have a noticeable difference in reflectance indices, which could be used to differentiate stover from its surrounding material in an agricultural field. Furthermore, it was discovered that based on raw data, a change in carotenoids from stover could be the cause of the band difference.

Future Directions

- Hyperspectral data is still being processed at the moment to identify band differences.
- Image recognition for stover and vegetation could be improved by integrating more advanced computer vision techniques such as machine learning.
- Once a unique band is identified, models to detect the presence of corn stover can enhance precision agricultural methods increasing profit for farmers and producing agrarian surpluses.

Figure 10. Decorative image

References

1. Ahamed, T., Tian, L., Zhang, Y., & Ting, K. C. (2011). A review of remote sensing methods for biomass feedstock production. *Biomass and bioenergy*, *35*(7), 2455-2469
2. Dale, L. M., Thewis, A., Boudry, C., Rotar, I., Dardenne, P., Baeten, V., & Pierna, J. A. F. (2013). Hyperspectral imaging applications in agriculture and agro-food product quality and safety control: a review. *Applied Spectroscopy Reviews*, *48*(2), 142-159
3. Graham, R. L., Nelson, R., Sheehan, J., Perlack, R. D., & Wright, L. L. (2007). Current and potential US corn stover supplies. *Agronomy Journal*, *99*(1), 1-11
4. Haddad, M. A., & Anderson, P. F. (2008). A GIS methodology to identify potential corn stover collection locations. *Biomass and Bioenergy*, *32*(12), 1097-1108
5. Seelan, S. K., Laguette, S., Casady, G. M., & Seielstad, G. A. (2003). Remote sensing applications for precision agriculture: A learning community approach. *Remote Sensing of Environment*, *88*(1-2), 157-169.

Acknowledgements

Thanks to everyone in the REU program and anyone that has aided me in this wonderful opportunity. Special thanks to Pierre Yan, Siyong Huang, Richard Deng, Benjamin Hong, and Vikki Xu. Extra jumbo special thanks to Dr. Mark Linderman, Dr. Caglar Koylu and December Weir.

Seizure-free, but amnesic: Changes in verbal learning performance following anterior temporal lobe resection

Carolina Deifelt Streese, Jacob Wu, Kenneth Manzel, Daniel Tranel
Department of Neurology, University of Iowa

Introduction

Temporal lobe epilepsy (**T L E**) is drug-resistant in 30% of the cases. For some, **temporal lobe resection** (**T L R**) surgery is the only way to treat seizures[1]. Even so, surgery is successful in eliminating seizures only 50-60% of the times and reduces seizure frequency in another 20-30% of the cases[2].

Meanwhile, 60% of left TLR and 30% of right TLR surgery cases resulted in verbal memory declines [3 4], an unintended complication that is the focus of our research project.

Hypothesis

To investigate the effect of laterality (left/right) on post-surgical memory decline, we investigated the following claims:

(1) **Left** (but not **right**) TLR patients will see significant verbal memory loss ▼ after surgery

(2) The shape of the learning curve for all groups will be **logarithmically concave down**

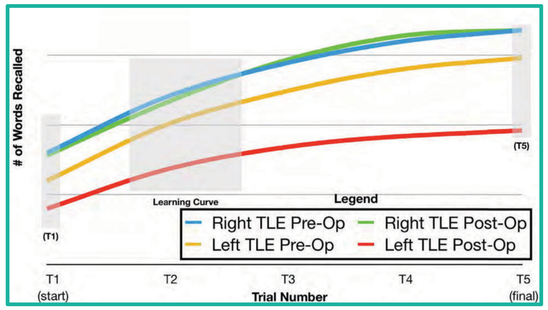

Figure 1. Prediction of Verbal Memory Score on the Rey-AVLT as a function of Trial Number; Blue curve represents Right TLE patient before surgery, which we predict is comparable to the Green Curve representing Right TLE patient after surgery. Yellow curve indicates left TLE patient before surgery, which we predict to be better than Red curve which is Left TLE patient after surgery.

Method

Rey-AVLT was analyzed because it specifically measures verbal memory, revealing trial-trial improvements. Trial 1 (T1) of the Rey-AVLT reveals the patient's initial memory, whereas Trial 5 (T5) is assumed to be indicative of their peak performance.

	Right TLE Patients	Left TLE Patients
n	23 pre, 11 post	20 pre, 13 post
gender	14 M, 9 F	13 M, 7 F
*age at pre-op testing**	31.73 ± 7.95	39.42 ± 12.8
education (years)	13.17 ± 2.12	12.75 ± 1.58
handedness	19 RH, 4 LH	15 RH, 4 LH, 1 MH
epilepsy chronicity	15.40 ± 10.63	22.75 ± 17.26
* significantly different between groups t(30.88) = 2.32, p<.05		

Figure 2. Table summarizing basic demographics data

$$y = \text{initial} + \beta_1 \cdot \text{trial} + \beta_2 \cdot \text{period} + \beta_{13} \cdot \text{laterality} + \beta_4 \cdot \text{trial}^2 + \beta_5 \cdot \text{trial} \cdot \text{period} + \beta_6 \cdot \text{trial} \cdot \text{laterality} + \beta_7 \cdot \text{period} \cdot \text{laterality} + \beta_8 \cdot \text{period} \cdot \text{trial}^2 + \beta_9 \cdot \textit{laterality} \cdot \text{trial}^2 + \beta_{10} \cdot \text{trial} \cdot \text{period} \cdot \text{laterality} + \beta_{11} \cdot \text{trial}^2 \cdot \text{period} \cdot \text{laterality} + \text{random subject intercept} + \text{random subject linear slope}$$

Left temporal lobe epilepsy patients have significantly altered learning curves that are not affected by surgery

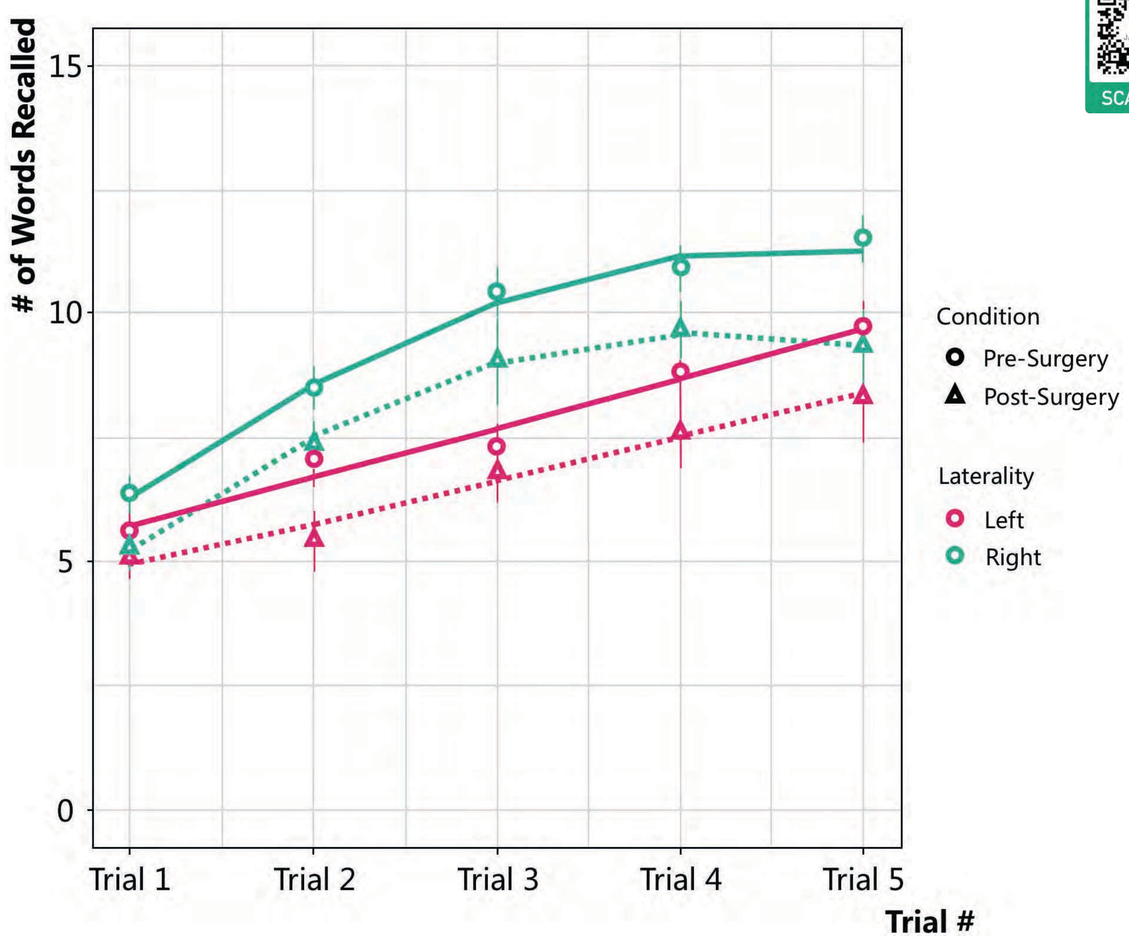

Figure 3. Graph of results collected from our investigation, where x-axis shows the trial number and the y-axis graphs the number of words recalled, showing right TLE patients before (solid green line) and after surgery (dotted green line) in comparison to left TLE patients before (solid pink line) and after surgery (dotted pink line)

SCAN ME

Results

We found an effect of **laterality** on T5 but not T1, and an effect of **pre/post** period on T1 but not T5. We found **no interaction** between laterality and pre/post period on T1/T5 score.

The shape of the learning curve was unexpectedly different for left vs. right (t(244.44) = 4.207, p < .001). Unlike the **linear** curve for **left**-sided patients, **right** TLE patients showed **concave downward growth** in learning curve as we predicted. Similarly, left-sided vs. right-sided cases had different **initial growth rate** (T2-T1), with **left** acquiring .88 fewer words than **right** (t(280.42) = -4.58. p < .001).

	Laterality (L/R)	Pre/Post Period	Interaction
T1	*None* t(49.74)=-1.24, p=.21	-.48 after surgery t(276.54)=2.95, p<.01	*None* t(276.54)=.34, p=.730
T5	-3.91 **left** t(260.74)=-5.32, p<.001	*None* t(246.29)=.75, p=.451	*None* t(246.29)=.52, p=.599
Initial Growth	-.88 **left** t(280.42)=-4.58, p<.001	*None* t(250.38)=.007, p=.995	*None* t(250.38)=.37, p=.706
Quadratic Slope	sig. different t(244.44)=4.20, p<.001	*None* t(244.44)=.51, p=.605	*None* t(244.44)=-.48, p=.628

Figure 4. Table summarizes the effect of laterality, pre/post period, and their interactions on T1 & T5 recall and slopes; statistical significance included

Conclusion

- Concerns for aggravated memory loss should affect not only left TLR surgeries, as **both groups are susceptible to declines**
- It is possible that while both hemispheres contribute differentially to verbal memory, their interconnectedness requires the **integrity of both for optimal performance**
- It takes longer for **left** TLR patients to reach the same memory performance, so specific post-surgical **intervention** may focus on repetition and extended exposure

Acknowledgements

I am genuinely grateful to Carolina Deifelt Streese, Kenneth Manzel, and Dr. Daniel Tranel for their eager support and guidance throughout research.

1 | González, H. F. J., Goodale, S. E., Jacobs, M. L., Haas, K. F., Landman, B. A., Morgan, V. L., & Englot, D. J. (2019). Brainstem Functional Connectivity Disturbances in Epilepsy may Recover After Successful Surgery. Neurosurgery, 0(0), 1–12. doi:10.1093/neuros/nyz128

2 | Pedley, T., & Scharfman, H. E. (2006). Temporal Lobe Epilepsy. Neurobiology of Disease, 1–5.

3 | Jehi, L. E. (2014). Prediction and Prevention of Verbal Memory Decline after Temporal Lobectomy. Epilepsy Currents, 14(1), 19–21. doi: 10.5698/1535-7597-14.1.19

4 | Kamm, J., Boles Ponto, L. L., Manzel, K., Gaasedelen, O. J., Nagahama, Y., Abel, T., & Tranel, D. (2018). Temporal lobe asymmetry in FDG-PET uptake predicts neuropsychological and seizure outcomes after temporal lobectomy. Epilepsy and Behavior, 78, 62–67. doi:10.1016/j.yebeh.2017.10.006

Bayesian Estimates of Bluetongue Virus Evolutionary Rates

Sandro Xiao[1], Andrew Kitchen, PhD[2]
Pleasant Valley High School [1], University of Iowa[2]

Introduction

- Bluetongue Virus (BTV) is a well-documented virus that concerns farmers due to leading to mortalities primarily affecting sheep and livestock; wildlife can act as carriers as well[1]
- BTV is a double-stranded (ds) RNA virus of the family *Reoviridae,* genus *Orbivirus*[1] – this is of particular interest due to the rarity of dsRNA genomes, even amongst viruses. Gaining a greater understanding of the BTV genome teaches us about the evolution of organisms with similarly structured dsRNA genomes
- The BTV genome consists of 10 linear segments ranging from 822 to 3954 base pairs, coding for 7 structural proteins and 3 nonstructural proteins[1]
- BTV segment 2 serotype 1 (BTV-1) is the focus of study. We will estimate the mean evolutionary rate and geographic origin for BTV-1 using segment 2 sequences.
- Implication is in understanding the history of BTV and how it has evolved, moved, and changed over time.

Methodology

Samples of BTV were collected from open access NIH genetic sequence database Genbank with the documentation of locus name, year of sampling, and geographic location. They were run through ClustalX and then manually aligned on Seqotron in order to distinguish the difference in base pair substitutions. Aligned segments' genome samples were run through BEAST for Bayesian analysis using the Markov chain Monte Carlo (MCMC) method to estimate the posterior distributions of the evolutionary rate and geographic origin. Corresponding locus name and dates were stochastically reassigned through RStudio Cloud and individually analysed with BEAST. The resulting randomized rate estimates provided a null distribution to which the original rate estimate was compared to determine our confidence in this rate estimate. The migration rates of BTV inferred in our phylogeographic analysis were assessed by calculating the Bayes factor for each, which provides an odds ratio for the presence of the rate.

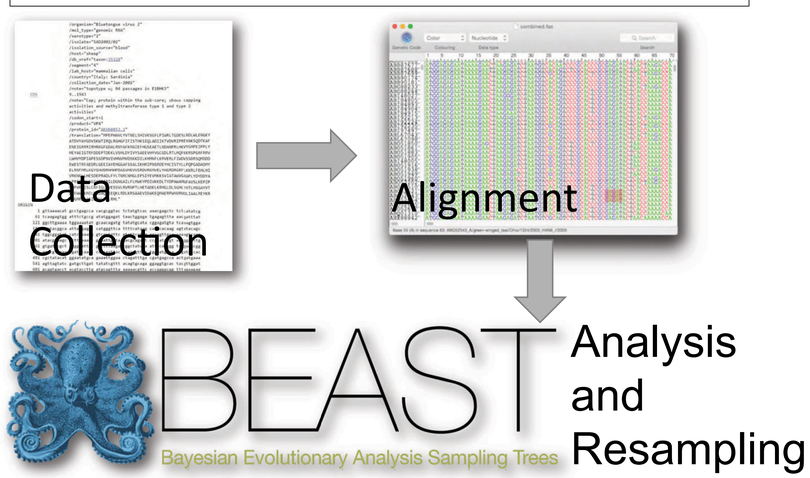

Results

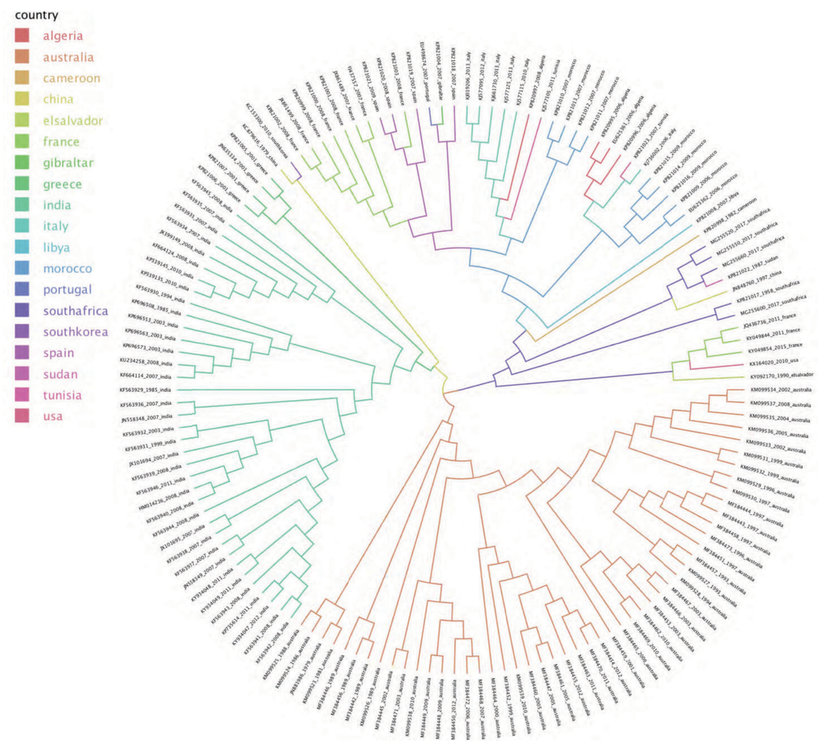

Fig 1. Phylogenetic tree depicting evolutionary connection of BTV-1 samples and location

X	DZ	AU	CM	CN	SV	FR	GI	GR	IN	IT	LY	MA	PT	ZA	KR	ES	SD	TN	US
algeria	X	0.1613	0.6235	0.2428	0.4188	0.6153	0.2704	0.1377	0.1264	**55.842**	1.3819	**9.3685**	0.2254	0.7494	0.1581	1.782	0.1908	**3.7967**	0.3074
australia		X	0.3175	**3.7605**	0.3601	0.2122	0.1507	2.1051	1.3624	1.9684	0.2662	0.1605	0.1426	0.5431	2.7221	0.1908	0.3235	0.1402	0.2553
cameroon			X	1.2674	0.8223	0.6647	0.2064	0.2771	0.237	0.7101	2.1608	1.0108	0.1949	**8.6586**	0.349	0.8032	0.7494	0.252	0.579
china		0.8925		X	1.0278	0.5908	0.1842	**4.2058**	**3.0158**	0.2855	0.7475	0.367	0.1621	**17.671**	**10.146**	0.4528	0.9484	0.1581	0.6601
el salvador					X	1.8653	0.3541	0.3354	0.2304	0.349	0.6116	0.4897	0.3371	1.9415	0.4049	1.0801	0.7222	0.2645	2.3122
france						X	1.6517	0.2453	0.1515	0.8713	0.7975	0.918	1.6575	1.127	0.3082	**3252.4**	0.3439	0.141	**4.7652**
gibraltar							X	0.1564	0.1459	0.3541	0.2329	0.6363	1.4937	0.2072	0.1826	**15.602**	0.1361	0.1337	0.349
greece				0.9533				X	**30.14**	0.1402	0.1949	0.1793	0.141	0.4677	**3.4079**	0.2155	0.247	0.1515	0.252
india				0.9288				0.7766	X	0.1208	0.1581	0.1256	0.0966	0.2998	2.3743	0.185	0.1646	0.128	0.1646
italy	1.5252									X	1.6886	**11.974**	0.3379	0.8328	0.1605	2.5888	0.1809	**11.476**	0.3294
libya											X	2.5985	0.1949	2.7951	0.2737	1.3409	0.4475	0.3294	0.5745
morocco	1.2747									1.2934		X	0.0275	1.3072	0.9328	0.2889	0.1105	0.0499	0.1448
portugal													X	0.1776	0.1515	**17.813**	0.145	0.1159	0.4058
south africa			0.9377	0.9578										X	0.7259	1.1308	**79.406**	0.199	1.1993
south korea				0.9597				0.94							X	1.5163	**35.536**	0.0655	0.689
spain						1.6801	1.0302						1.0226			X	0.2956	0.1483	1.6586
sudan														0.9052	1.0113		X	0.1386	0.5332
tunisia	1.1408									1.3088								X	0.2163
usa						0.9496													X

Fig 2. Upper half of table depicting Bayes Factors of phylogeographic sampling locations rates. Lower half depicting well-supported migration rates (BF > 3).

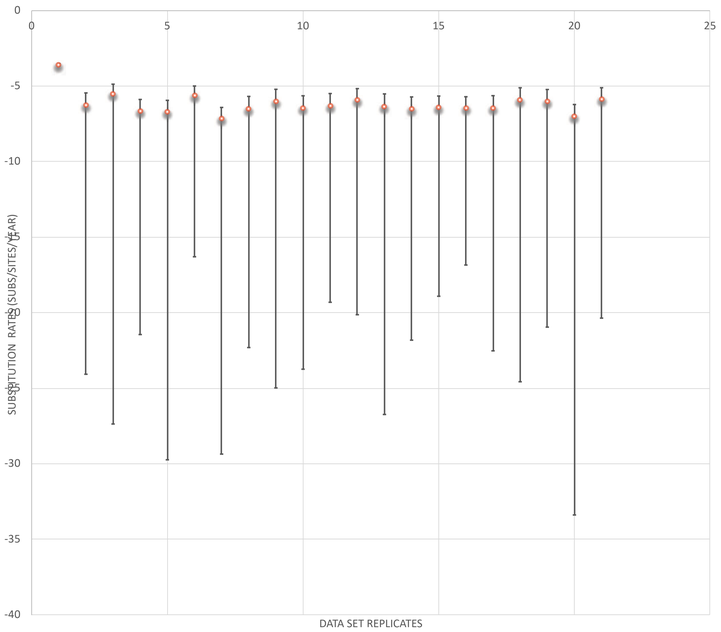

Fig 3. Plot of empirical evolutionary rate estimate for BTV (column 1) in comparison to 20 randomized BTV rate estimates (columns 2-21). Note the empirical rate estimate does not overlap with the randomize rate estimates.

Conclusion

The evolutionary mean rate of Bluetongue Virus segment 2 serotype 1 (BTV-1) was estimated to be 2.63 x 10^{-4} substitutions per site, per year. It was determined to be statistically significant after falling outside of the error bars of the upper and lower bounds of higher posterior density (HPD) interval of 95% of the sampled values (Fig. 3). We can compare this estimate to a study performed by Carpi et al. (2010), who found "that Seg -2, -3, -6, and -10 evolve at mean rates of between 0.52 and 6.9 x 10^{-4} substitutions per site, per year"[1], allowing us to postulate that our conclusion to be reasonable as it is within the range of the findings set by this previous study.

From our phylogeographic analysis and calculations, 19 of our migration rates between sampling locations were well-supported by Bayes factors that were greater than our critical value of 3.0 (Fig. 2): DZ-IT (1.53), DZ-MA (1.28), DZ-TN (1.14), AU-CN (0.89), CM-ZA (0.94), CN-GR (0.95), CN-IN (0.93), CN-ZA 0.96), CN-KR (0.96), FR-ES (1.68), FR-US (0.95), GI-ES (1.03), GR-IN (0.78), GR-KR (0.94), IT-MA (1.29), IT-TN (1.31), PT-ES (1.02), ZA-SD (0.91), and KR-SD (1.01). As a result of the BEAST analyses, Figure 1 displays the evolutionary relations between BTV-1 samples collected based on date and location of sampling. From this, it can be concluded that the origin of BTV-1 is South Africa (ZA).

This study will be further developed and continued following this portion of the project through the similar data collection and analyses of the other BTV-1 segments - 1, -3, -4, -5, -6, -7, -8, -9, and -10, and the other serotypes, to determine their respective evolutionary rates and geographic origins. One outstanding question concerns cross-serotype variation in BTV origins and history of dispersal with implications for future policy regarding vaccination campaigns and prevention of bluetongue disease in livestock.

Acknowledgements

I am grateful for Dr. Drew Kitchen and his dependable guidance. I would also like to express thanks to Alex and Isiaha, the SSTP program, and the 2019 SSTP cohort for the help and support in my project.

References

1. Carpi, G., Holmes, E. C., & Kitchen, A. (2010). The Evolutionary Dynamics of Bluetongue Virus. Journal of Molecular Evolution, 70(6), 583–592. https://doi.org/10.1007/s00239-010-9354-y
2. Drummond, A. J., & Rambaut, A. (2007). BEAST: Bayesian evolutionary analysis by sampling trees. BMC Evolutionary Biology, 7(1), 214. https://doi.org/10.1186/1471-2148-7-214
3. Duchêne, S., Duchêne, D., Holmes, E. C., & Ho, S. Y. (2015). The performance of the date-randomization test in phylogenetic analyses of time-structured virus data.*Molecular Biology and Evolution, 32*(7), 1895-1906. doi:10.1093/molbev/msv056
4. Schwartz-Cornil, I., Mertens, P., P. C., Contreras, V., Hemati, B., Pascale, F., Bréard, E., ... Zientara, S. (2008). Bluetongue virus: virology, pathogenesis and immunity. Vet. Res., 39(5). https://doi.org/10.1051/vetres:2008023

Films on glassy carbon electrodes: H_2 evolution and transition metal complex

Victoria Xu, Joshua Coduto[2], Christian D. Haas[2], Professor Johna Leddy[2]
Department of Chemistry, University of Iowa, Iowa City, IA[2]

Part 1 key words: Hydrogen evolution, carbon black, magnetic particles, capacitance

Background

Hydrogen fuel cells are an efficient way of storing energy from renewable and intermittent energy sources. The hydrogen evolution reaction (HER) drives energy storage and transfer, and the best electrode used is the platinum electrode. Platinum is too expensive for large scale energy purposes, so we are attempting to recreate capacitance and current by applying Nafion, magnetic particles, and carbon black mixtures as films on glassy carbon electrodes.

HER: $2H^+ + 2e^- \rightarrow H_2$

Objectives

Hypothesis: Increasing carbon black concentration increases the capacitance of the system up to a certain point where it blocks the surface of the electrode. Magnetic particles do not affect capacitance.

Objectives:
1. Find optimal concentration of carbon black in the film to enhance the capacitance of the electrochemical double layer at the surface of the electrode
2. Observe effect of magnetic particle film on the electrode

Methods

Cyclic Voltammetry (CV) Scans for HER

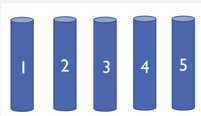

Apply different film to each electrode, set up cell in 0.5M H_2SO_4

Run scans at these scan rates for each electrode

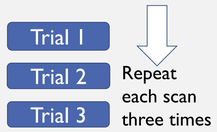

Repeat each scan three times

Data Analysis

Figure 1 shows scans of the same electrode/film at different scan rates. Using the average of the current values at 0.5 volts, we plotted scan rate values on the x-axis and the average current on the y-axis (Figure 2). In Figure 2, the slope of the best fit line represents the **capacitance** value of the electrochemical double layer.

Results

Results Table 1: Capacitance Measurements of Each Film

Film Composition	Average Measured Capacitance (microfarads)
Nafion	5.2 ± 0.5
20:1 Nafion to carbon black (by mass)	180 ± 10
10:1 Nafion to carbon black (by mass)	470 ± 43
8 micron Spherotech magnetic particles	4.5 ± 0.4
1 micron Spherotech magnetic particles (film thickness doubled)	9 ± 1

- Magnetic particles do not increase the capacitance of the electrochemical double layer.
- As expected, increasing the concentration of carbon black in the film increases the capacitance.

Implications

1. Creating an efficient fuel cell using glassy carbon electrodes will require both carbon black and magnetic particles in the film.
2. Carbon black increases capacitance only, magnetic particles increase current signal only.

Future Studies:
1. Further research into carbon black on a molecular scale.
2. Find an optimal combination of carbon black + magnetic microparticles
3. Implementing film in electrolyzer and fuel cells

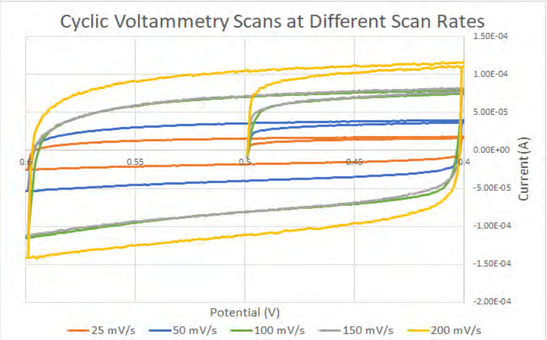

Figure 1. Cyclic voltammetry scans at different scan rates using electrode coated with 10:1 Nafion to carbon black film (Trial 1)

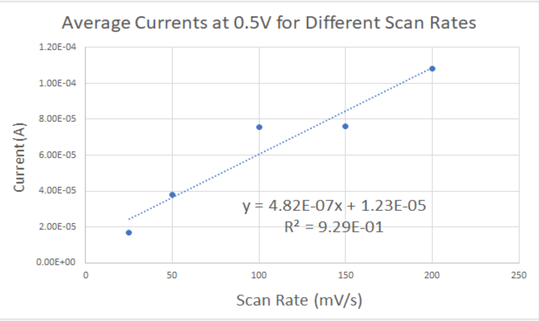

Figure 2. Currents at 0.5 V for different scan rates, where the capacitance value is the slope of the best fit line for 10:1 Nafion to carbon black film (Trial 1).

Part 2 key words: $Co(bpy)_3^{3+}$, Square Wave Voltammetry, Magnetic Particles

Background

Glassy carbon electrodes could also be used as the positive electrode in batteries. Past studies have shown that the current signal from other types of electrodes are enhanced when magnetic film is applied, and we want to see if the same result applies to glassy carbon electrodes.

Objectives

Hypothesis: Magnetic particles enhance the current response of glassy carbon electrodes.

Objective:
1. Observe effect of magnetic particles
2. Optimize film

Implications

1. Higher concentrations of magnetic particles lead to higher current.
2. However, if there are too many particles, current signal decreases.

Future Studies:
1. Continue varying concentration, particle size, and thickness of film

References

Zou, P., & Johna, L. (2006). Magnetized nickel electrodes for improved charge and discharge rates in nickel metal hydride and nickel cadmium batteries. *Electrochemical and Solid-State Letters*, *9*(2), A43-A45. https://doi.org/10.1149/1.2139977

Dunwoody, D. C., Unlu, M., Wolf, A. K. H., Gellett, W. L., & Leddy, J. (2005). Magnet incorporated carbon electrodes: Methods for construction and demonstration of increased electrochemical flux. *Electroanalysis*, *17*(15-16), 1487-1494. https://doi.org/10.1002/elan.200503297

Ramaley, L., & Krause, M. S., Jr. (1969). Theory of square wave voltammetry. *Analytical Chemistry*, *41*(11), 1362-1365. https://doi.org/10.1021/ac60280a005

Bard, A. J., & Faulkner, L. R. (2001). *Electrochemical methods: Fundamentals and applications* (2nd ed.). John Wiley and Sons.

Acknowledgements

Thank you Josh, Christian, Dr. Leddy, and the other members of the Leddy Lab for all your help and support along the way. Thank you Belin Blank Center and the SSTP Program for making this opportunity possible, and to the Army Research Office for sponsoring the work.

Methods

- Film preparation, $Co(bpy)_3^{3+}$ solution stays constant

Factors varied:
- Film thickness
- Concentration of magnetic particles
- Size of magnetic particles

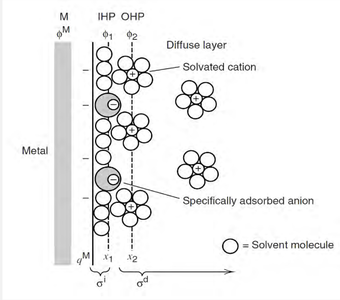

Figure 3: Model of the electrochemical double layer. Free charged particles in the solution are attracted to the electrode, and the distance between two oppositely charged layers form a capacitor (we measured this capacitance in **part 1**) (Adapted from Bard & Faulkner)

Results

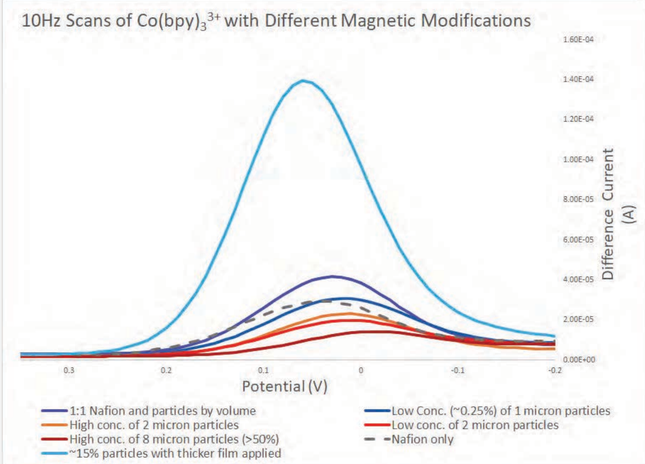

Figure 5. The blue lines represent scans where the film resulted in a higher current signal than pure Nafion film, and the red lines represent films that resulted in lower current signals than pure Nafion. A moderate amount of microparticles with 10 microliters of film applied (as opposed to 5 microliters for the other films) resulted in the highest current signal.

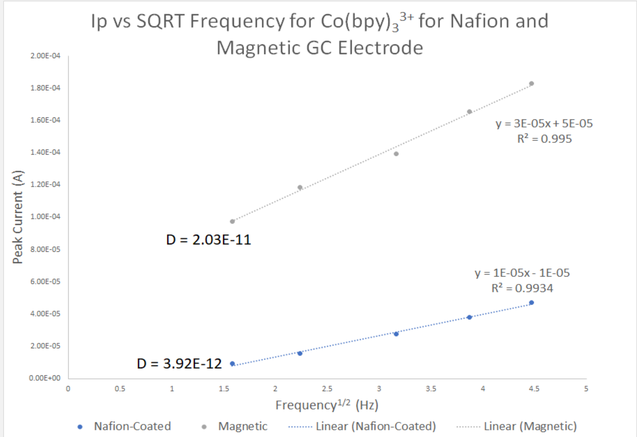

Figure 6. The slope of the lines can be used to calculate the diffusion coefficient. The magnetic film yielded a higher diffusion coefficient, which is consistent with the higher current values.

Why Square Wave Voltammetry (SWV)?

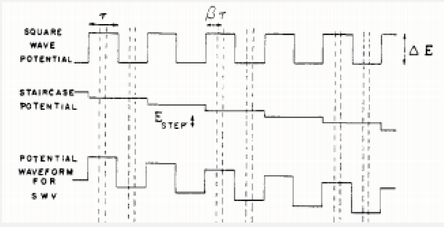

Figure 4: Wave forms in SWV (Adapted from Ramaley et al.)

While the double layer is forming, movement of charged particles creates a **charging current,** which interferes with the measured current. The smaller the change in voltage, the less time the formation of the double layer takes, and the effect of the charging current diminishes. Using SWV means that instead of a continuous increase in potential, potential would be changed in a staircase-like fashion.

Exploring genetic interactions between a neurodegeneration mutant and Alzheimer's disease in flies.

Pierre Yan[1]; Richard Deng[2]; Krishna Madhav Nukala[3]; Anthony Lilienthal[3]; Alexander G. Bassuk, MD, PhD[3]; J. Robert Manak Ph.D[3]
[1]Haddonfield Memorial High School, [2]Dougherty Valley High School, [3]University of Iowa

Introduction

Alzheimer's disease is a widespread disease that affects 1 in 10 people over the age of 65[1]. The onset of the disease has been associated with the incorrect processing of the *APP* gene in humans. This results in a build up of β-amyloid plaques in the brain[2]. The fly ortholog, *appl,* has been shown to genetically interact with members of the Planar Cell Polarity (PCP) complex (Figure 1b). More specifically, *Van gogh (Vang*) interacts with *appl* with respect to neural connectivity in the *Drosophila* brain. Another member of the PCP complex, *prickle* is known to genetically interact with *Vang*. We have recently shown that mutants of one isoform of *prickle (prickle-prickle,* or pk^{pk}) exhibit increased neurodegeneration, and we have demonstrated a genetic interaction between pk^{pk} and *appl* with regard to adult survivability. We thus sought to determine whether the pk^{pk} isoform interacts with *appl* regarding neuronal connectivity, a known role for pk^{pk}.

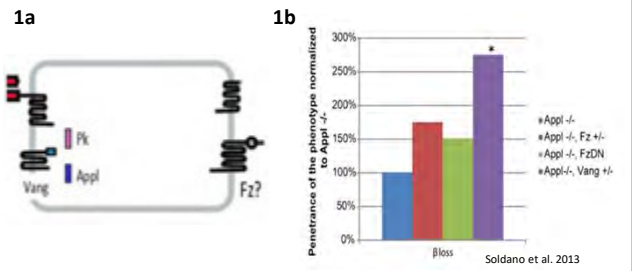

Figure 1. (1a) A schematic showing the interaction between PCP proteins vang and prickle with the Alzheimer's protein appl inside a neuron to promote proper neuronal development. **(1b)** This graph investigates the interaction between the $appl^d$ mutant and multiple mutants in the PCP complex during the development of the mushroom body of *Drosophila*. Soldano et al. demonstrated that the *appl* gene shows statistically greater disruption to proper neuron development when *vang* gene is also disrupted, hence, proving *appl* and *vang* genetically interact with each other. (figure adapted from Soldano et al., 2013)

Hypothesis

Given that both *appl* and *pk* mutants have been shown to yield neuronal connectivity defects, we hypothesize that these mutants will show a genetic interaction with regard to embryonic neuronal connectivity.

Method

1. Fly lines assayed in this experiment: w^{1118} *(+/+), $appl^d$, pk^{pk} (pk), and $appl^d$; pk.*
2. Collect the 14 - 16 hour aged embryos from the various lines and remove the chorion membrane.
3. Fix the embryos in a 50/50 heptane and methanol mixture.
4. Remove the vitelline membrane by vigorously shaking the embryos in methanol.
5. Wash the embryos and perform immunohistochemistry (IHC) to stain the peripheral and motor neurons with antibodies (22C10 is a marker for peripheral neurons and Fasciculin II is a marker for motor neurons).
6. Image the embryos using confocal microscopy and quantify the number of defects in each line.

Preliminary Results

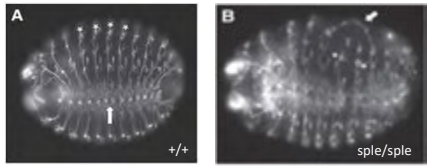

Figure 2. Staining of PNS and motor neurons using 22c10 and fas2 primary antibodies with Alexa Fluor 488 secondary antibodies.

Tao, Manak, Sowers et al. 2011

Results

	22C10	Fasciculin II	Total Counts
+/+	70	38	108
$appl^d/appl^d$	56	50	106
pk/pk	50	57	107
$appl^d/appl^d;pk/pk$	8	0	8

Results Cont.

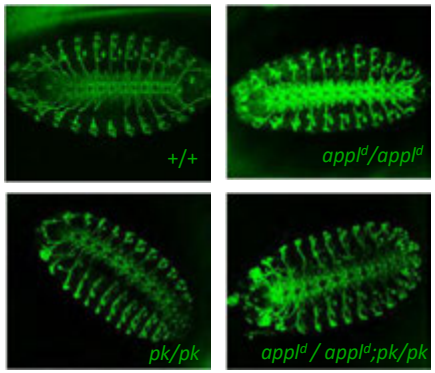

Figure 3. IHC of *Drosophila* embryos showing normal neuronal connectivity. All the embryos are stained with the antibody 22C10. Brightness and contrast are modified for ease of viewing.

Conclusions

- No wiring defects were found in any of the lines: +/+, $appl^d$, *pk*, and $appl^d;pk$
- This could be due to the fact that the sample size of each of the lines had low counts with low statistical power.
- There is also a possibility that there is no genetic interaction between *pk* and $appl^d$ despite the interaction with the PCP complex members.
- Alternatively, the phenotype of these mutants may be revealed at later developmental stages.

Future Directions

- Increase total numbers for each of the lines to increase statistical power.
- Improve the method to increase the amount of useable embryos to be imaged.

Contact

Pierre Yan
University of Iowa

References

1. Facts and Figures. (n.d.). Retrieved from https://www.alz.org/alzheimers-dementia/facts-figures
2. O'Brien, R. J., & Wong, P. C. (2011). Amyloid precursor protein processing and Alzheimer's disease. Annual review of neuroscience, 34, 185–204. doi:10.1146/annurev-neuro-061010-113613
3. Soldano, A., Okray, Z., Janovska, P., Tmejová, K., Reynaud, E., Claeys, A., . . . Hassan, B. A. (2013). The Drosophila Homologue of the Amyloid Precursor Protein Is a Conserved Modulator of Wnt PCP Signaling. PLoS Biology, 11(5). doi:10.1371/journal.pbio.1001562
4. Tao, H., Manak, J. R., Sowers, L., Mei, X., Kiyonari, H., Abe, T., ... Bassuk, A. G. (2011). Mutations in prickle orthologs cause seizures in flies, mice, and humans. American journal of human genetics, 88(2), 138–149. doi:10.1016/j.ajhg.2010.12.012

Combined Electrodialysis-Electrolysis Process for Nitrate Removal and Reduction

Richard Yin[1,2], Sattar Alsaedi[3], Syed Mubeen[3]

Adlai E. Stevenson High School[1]; Secondary Student Training Program[2]; Department of Chemical and Biochemical Engineering, University of Iowa[3]

Introduction

- High Nitrate/Nitrite levels threaten human health & infants
- Safe limit: 10mg/L (as N)
- Fertilizer→groundwater runoff
- Current methods-do not remove N2 or are energy inefficient

Goal

- Combined electrolysis+electrodialysis setup

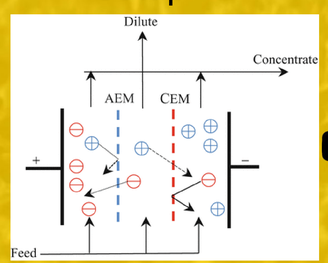

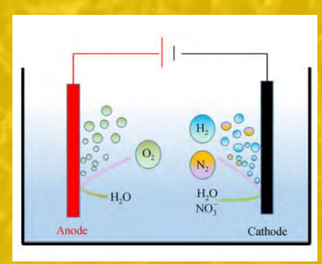

Methods

Part 1:

- Existing ED setup
- Ran at constant voltage
- Determined using limiting current density

Part 2:

- Deposition using potentiostat
- Reticulated vitreous carbon
- Constant voltage applied

Part 1: Electrodialysis

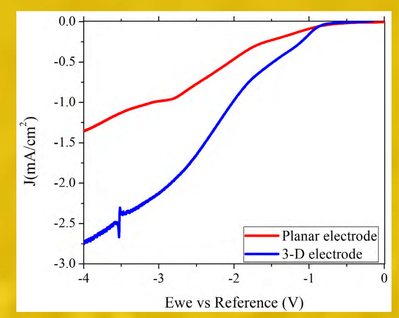

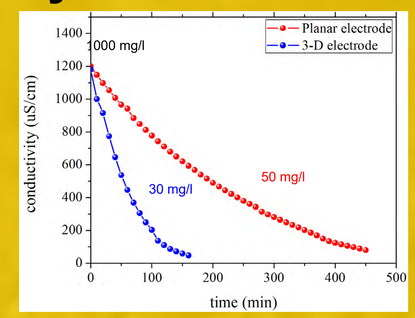

- Applied current: for ___
- Decreased conductivity lower nitrate concentration
- Carbon foam electrode was more energy efficient, and took less time to remove nitrate

Part 2: Electrolysis

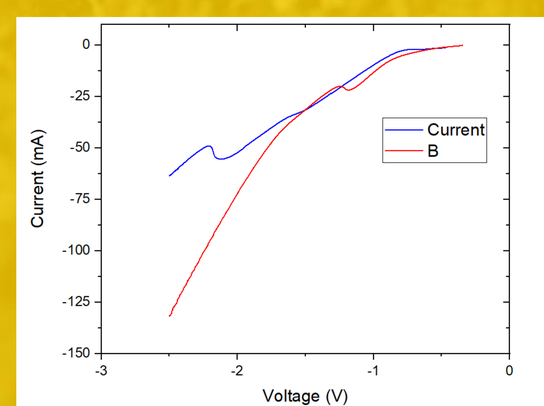

Conclusions

- ED is possible using existing setup for nitrate removal
- Clear nitrate reduction using Pd/Cu
- Acidic conditions nonideal due to competing H2 evolution

Future Work

- Study impact of pH
- Deposit nanoparticles→reduce Pd
- Determine if catalyst is most cost effective
- Combine 2 components with RED
- Evaluate efficiency, calculate cost vs existing methods

Acknowledgements

Many thanks to the following people: Sattar ALADI for mentoring me during SSTP, Dr. Syed Mubeen for providing invaluable advice, the Mubeen Research Group, the 2018 SSTP cohort, the University of Iowa, and the Belin-Blank Center

Heat stress alters mitochondria distribution and structure in cultured *Drosophila* giant neurons

Jeffrey Zhang[1], Veda Amalkar[2], Tristan O'Harrow[3], Cassandra Burke[3], Atulya Iyengar[3], Chun-Fang Wu[3]
[1]Centerville High School, Centerville, OH, [2]Valley High School, Des Moines, Iowa, [3]Department of Biology, University of Iowa

Introduction

Why *Drosophila*? (Hales, 2015)
- Fruit flies have a small genome with four chromosomes
- Easily cultured in lab, many offspring
- Short reproductive cycle of 9 to 10 days at 25 °C

Mitochondrial Fission and Fusion
- Mitochondria play a critical role in acclimatizing cells to metabolic or environmental stressors (Youle & van der Bliek, 2012).
- Mitochondrial fusion acts to reduce cellular stressors by combining the contents of multiple partially damaged mitochondria to form functional mitochondria (Youle & van der Bliek, 2012).
- Fission primarily functions to create new mitochondria while removing damaged mitochondria from the cell (van der Bliek, Shen & Kawajiri, 2013)
- Mutations in fusion and fission proteins are connected with numerous diseases, such as Parkinson's, Alzheimer's, and Huntington's (Cho, 2010; Costa, 2010; Lutz, 2009; Shirendeb, 2012; Song, 2011; Wang, 2009)

Methods

Goal: Acquire different genotypes of UAS-mito-roGFP giant neurons for analysis. UAS-mito-roGFP is a genetically encoded tag for mitochondria. It is a UAS construct driven in subpopulations of neurons by the Gal4/UAS system.

1) Collect and plate *Drosophila* embryos from crossed females and males
2) Incubate some of the cultures for each genotype at 25 °C and the others at 29 °C
3) Image neurons across multiple days under phase-contrast and fluorescence, with a focus on neurite mitochondria
4) Measure a long, short, and representative length mitochondria for every visible neuron
5) Observe and graph differences in mitochondria structure and distribution under temperature and aging effects

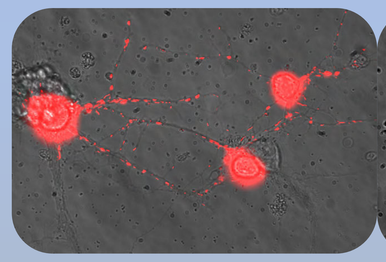

Figure 1. Mitochondria of nsyb-Gal4 tagged neurons

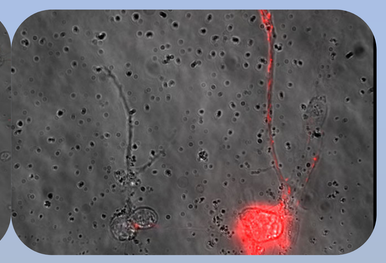

Figure 2. Mitochondria of OK371-Gal4 tagged neuron

How does heat stress effect mitochondria distribution and structure?
Do different neuron classes possess different mitochondrial morphologies?

Results

- **Mitochondria of cultures at 25 °C exhibited increased elongation, while those at 29 °C displayed punctate characteristics.**
- **As cultures become older, mitochondria median length begins to decrease.**
- **Mitochondria in neurons expressing nsyb-Gal4 possessed the greatest median length.**
- **Mitochondria in neurons expressing OK371-Gal4 had the greatest median length under heat stress.**
- **Neurons expressing TH-Gal4 demonstrated the most punctuated characteristics at both 25 °C and 29 °C.**

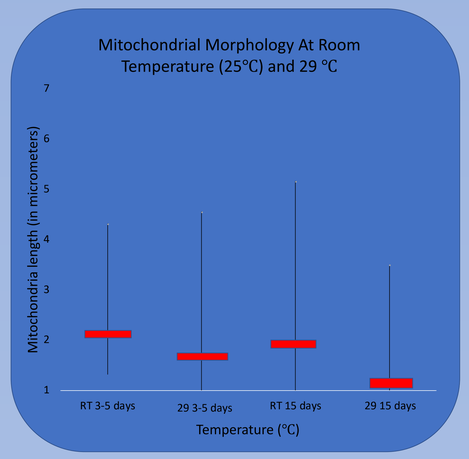

Figure 3.
- Comparison of OK371 tagged neuron mitochondria at room temperature (image A) and under heat stress (image B)
- Comparison of OK371 tagged neuron mitochondria at 3 days (image C) and 15 days (image D)

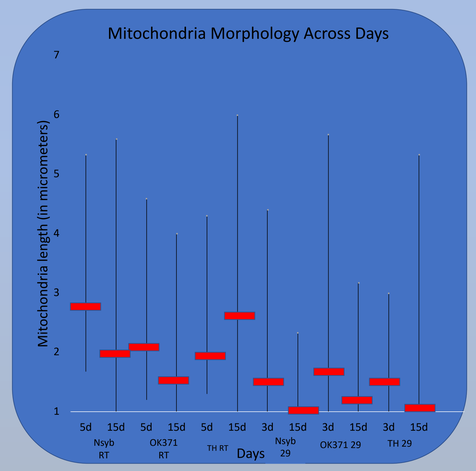

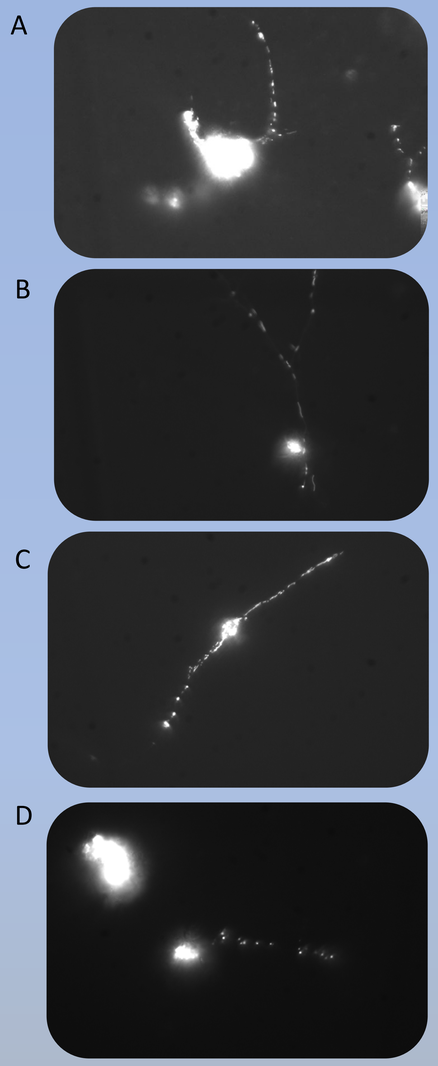

Conclusions

Our results demonstrate a clear effect of heat and age stress on mitochondrial morphology.

- The consistent pattern of punctated mitochondria at 29°C and elongated mitochondria at 25°C exemplifies the effect of heat stress
- In high stress environments decreased fusion and increased fission occur in conjunction as an adaptive response, while the opposite occurs under levels of low stress (van der Bliek, 2013)
- Consistent increase in median length of mitochondria from zero to six days demonstrate a period of growth.
- A considerable decrease in median length at thirteen and fifteen days demonstrate the effect of age stress

Future implications

- Further understanding of the specific reactions of mitochondria to stress could aid in development of treatments for mitochondrial and neurodegenerative diseases
- Inhibition of mitochondrial division may result in disease-associated phenotypes of multiple neurodegenerative diseases

References

Youle, R. J., & Van der Bliek, A. M. (2012, August 31). Mitochondrial fission, fusion, and stress.
Van der Bliek, A. M. (2013). Mechanisms of Mitochondrial Fission and Fusion. *Cold Spring Harbor Laboratory Press*.
Wu, C., Sakai, K., Saito, M., & Hotta, Y. (1990). GiantDrosophila neurons differentiated from cytokinesis-arrested embryonic neuroblasts. *Journal of Neurobiology, 21*(3), 499-507. doi:10.1002/neu.480210310
Hales, K. G., Korey, C. A., Larracuente, A. M., & Roberts, D. M. (2015, November). Genetics on the Fly: A Primer on the Drosophila Model System. Retrieved from https://www.ncbi.nlm.nih.gov/pmc/articles/PMC4649653/

Acknowledgements

I would like to thank Dr. Wu and the other lab members for advising and supporting me throughout these five weeks

Large-scale CanaryTrap implementation: Detecting data misuse by Facebook's third-party apps

Kathy Zhong[1], Shehroze Farooqi[2], Zubair Shafiq[2]

Amador Valley High School[1], Department of Computer Science, The University of Iowa[2]

Introduction and Background

Online social networks offer their users the ability to access other applications more conveniently through their interfaces. Facebook, for example, offers users millions of apps to log in via Facebook account.

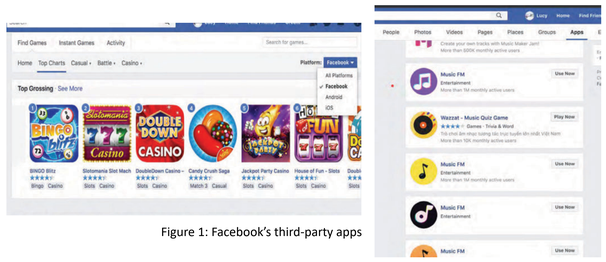

Figure 1: Facebook's third-party apps

Problem

Third-party applications ask for a multitude of information to enhance user experience. However, many of these apps are often easily breached or misuse information themselves. There have already been multiple instances of misuse of data illicitly collected via third-party applications, such as the Cambridge Analytica scandal.

The danger such threats pose increases with consideration of the fact that research has found that third-party applications tend to ask for and store more information than is considered strictly necessary (Huber et al., 2013), and are often under attack by collusion networks and other cybercriminals hoping to manipulate users' accounts (Farooqi et al., 2017).

Solution: CanaryTrap

CanaryTrap is an approach that can be used to systematically monitor the way apps are using private information by leaking honeytokens, in this case email addresses, and then monitoring the emails those accounts receive. We analyze received emails to detect the misuse of user's data by third-party applications.

Key Contributions

- Facebook's anti-abuse systems make audit by independent watchdogs, including large-scale CanaryTrap implementation, difficult
  - ➢ Create a large number of accounts to run multiple instances of experiments
  - ➢ Make accounts as realistic as possible
- Initiation of a long-term implementation of CanaryTrap over thousands of third-party apps on Facebook
  - To mimic human behavior, CanaryTrap processes around ten apps every three hours
- Some apps begin illicitly spreading data immediately, while others do so gradually
- Transition to matrix implementation of CanaryTrap
- Blackbox experimentation and analysis of Facebook's anti-abuse systems
  - Facebook looks at device activity as well as account activity
    - Factors include account creation rate, post rate, and email rotation rate

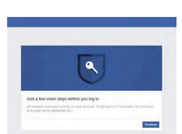

Figure 8: Facebook account locked

Method

Honeytoken: a small piece of information purposefully leaked to be monitored to detect its misuse

- ➢ Create Facebook accounts on different IP addresses; each one serves as a different instance
  - Manual creation process to prevent being locked out by Facebook's anti-abuse systems
- ➢ For each instance: change the account's primary email address, install an app, then uninstall it, before repeating the process
  - This way, we have a 1-1 mapping between email address and third-party app
  - This process is automated, using Selenium

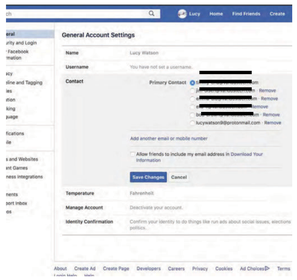

Figure 2a: Changing primary emails

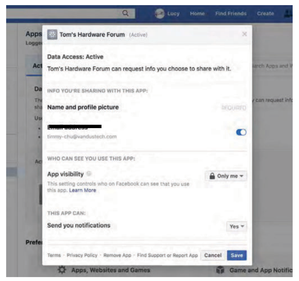

Figure 2b: Installing third-party apps

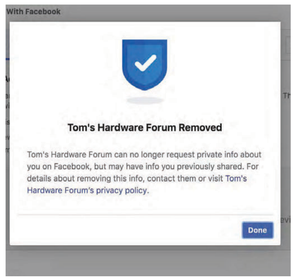

Figure 2c: Removing installed apps

- ➢ Analyze the emails received and categorize them as *recognized* (sent by the respective app installed with that email as the primary address) or *misuse* (sent by an app not related to the installed app)
  - We manually further inspect *misuse* categorizations to avoid false positives

Results

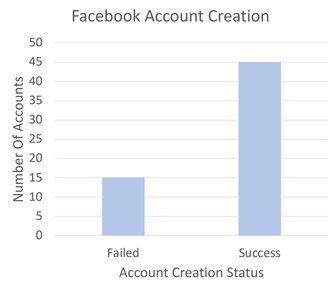

Figure 3: Distribution of Facebook accounts successfully and unsuccessfully created

Despite switching between IP addresses and browsers, many accounts were still locked by Facebook's anti-abuse system that categorized them as spam accounts

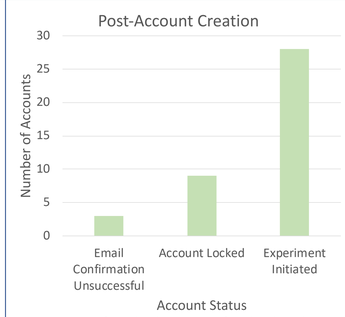

Figure 4: Status of Facebook accounts after they have been created, up to initiation of experiment

Facebook locks some accounts directly if they were created too quickly

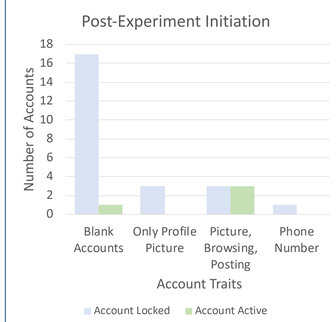

Figure 5: Attributes of accounts able to begin the experiment without being locked by Facebook, with their current status

More consistent activity on an account makes it less likely to be locked

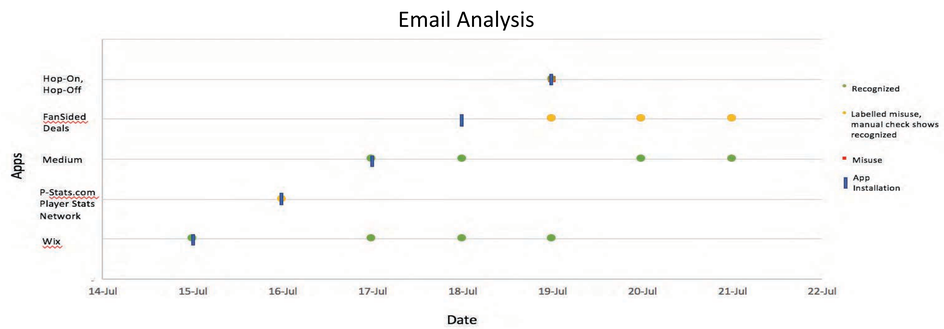

Figure 6: Timeline of emails received by five of Facebook's third-party apps. Each dot represents an email received, while the different colors represent the different categorizations of that email.

- Apps have already begun spreading information, although more time would give more instances of information abuse

Matrix Implementation

To maximize scalability of the experiment, we can implement a matrix implementation; essentially, a multi-dimensional version of the current array implementation.

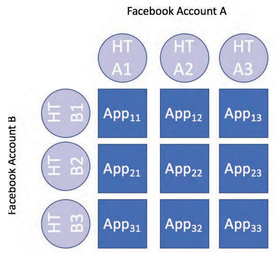

If honeytokens HT A1 and HT B1 receive the same email from the same sender, we can, under the assumption that an app will send promotional emails to all emails, trace that email back to App_{11}.

Figure 7: Visual representation of matrix implementation using two Facebook accounts

Limitation: as we decrease the number of honeytokens used, we increase probability of false positives due to the arrangement of the matrix and method of corresponding emails to apps

If app_{11} and app_{22} send emails from the same email, for example, there is a possibility that that will be recorded as app_{12} and app_{21}. This probability of getting a false positive increases as the number of Facebook accounts (and thus "dimensions") used increases, but decreases as the number of honeytokens increases.

For a matrix implementation with two Facebook accounts, with m and n honeytokens, respectively, we can model the probability of getting a false positive with

$$error = \in [-(m+n) + mn + 1]$$

where $\in$ is the probability that one pair of apps send the same email.

Future Directions

- Continue implementing CanaryTrap for all third-party apps on Facebook
  - Adjust to matrix implementation to maximize scalability and minimize error
- Expand CanaryTrap to monitor apps on other platforms
- Develop a website to inform the public of apps that are misusing their data
- Further research into Facebook's anti-automation policies and practices

Acknowledgements

Special thanks to Dr. Zubair Shafiq and Shehroze Farooqi for their guidance over these past weeks for this project, as well as to the Secondary Student Training Program and Belin Blank Center for this opportunity.

References

DeBlasio, J., Savage, S., Voelker, G. M., & Snoeren, A. C. (2017). Tripwire: Inferring internet site compromise. *Proceedings of the 2017 Internet Measurement Conference on - IMC 17*. doi:10.1145/3131365.3131391

Farooqi, S., Zaffar, F., Leontiadis, N., & Shafiq, Z. Measuring and mitigating OAuth access token abuse by collusion networks. (2017). *Proceedings of the Internet Measurement Conference on – IMC 2017*. doi:10.1145/3131365.3131404

Huber, M., Mulazzani, M., Schrittwieser, S., & Weippl, E. (2013). AppInspect: Large-scale evaluation of social networking apps. *Proceedings of the First AMC Conference on Online Social Networks – COSN 13*. doi:10.1145/2512938.2512942